2D

3D

Three-Dimensional Flow in the
Root Region of Wind Turbine Rotors

Galih Bangga

Three-Dimensional Flow in the Root Region of Wind Turbine Rotors

A thesis accepted by the Faculty of Aerospace Engineering and Geodesy of the University of Stuttgart in partial fulfilment of the requirements for the degree of
Doctor of Engineering Sciences (Dr.-Ing.)

by

Galih Senja Titah Aji Bangga

born in Kediri, Indonesia

Committee chair   : Prof. Dr.-Ing. Ewald Krämer
Committee member : Prof. Jens Nørkær Sørensen, PhD., Dr. Tech.
Date of defence : 18 December 2017

Institute of Aerodynamics and Gas Dynamics, University of Stuttgart

2018

Galih Bangga

Three-Dimensional Flow in the Root Region
of Wind Turbine Rotors

"I dedicate this thesis to the loving memory of my father, Madngisom, who has given me a proper guidance since I was born and inspired me a lot in numerous fruitful discussions."

"To my mother, Eko Supriati, who always encourages me in any situations and provides me a strong motivation to learn especially in the field of natural sciences."

"To my sister, Tiara Ayu Nugraha Putri, who always be a great rival in any occasions. The time we were competing and helping each other has led us to advance further."

"To my big family."

"To myself. Thank you for holding on this far. You are doing good."

"At last but not least, to my future wife and children."

Acknowledgements

This thesis was written when I was pursuing my doctoral degree, where I was given the opportunity to conduct systematic studies in wind energy field under a favourable scientific working environment. In this particular section, I would like to express my gratitude and appreciation towards the people helping me during the completion of the studies.

First and foremost, I would like to thank my supervisor Prof. Ewald Krämer. It has been an honour for me to be his doctoral student. He has taught me, both consciously and unconsciously, about what the importance of fundamental understanding of fluid mechanics is. I appreciate all his critics, ideas, funding and time spent for me to make my doctoral experience fascinating and challenging. He strongly inspired me and I would like to be a Professor as good as him in the future.

The person who has a significant role during the completion of this work is none other than Dr. Thorsten Lutz. This thesis would not be finished without his contributions. I gratefully thank him for spending a lot of time during our discussions. I am amazed by his hard-working habit from the early morning to the late afternoon everyday. I am relieved that he never scolded me for always coming late to the institute. He always gave me a lot of remarks when I showed him my paper drafts. I still remember about his very first comment on my very first draft: "please revise the English". This made me learn a lot and significantly improved my writing skills.

All the colleagues at the institute were very helpful especially the wind energy group. I personally think that this group conducts very good researches in several fields of wind energy areas. The script shared and the continuous development of the FLOWer code has significantly accelerated my research investigations. All the members of the institute also served as nice friends where I could talk to when I had any problem, not merely as a formal colleague dealing with professional work.

I would not be able to come to Germany if there was no funding provided by the Government of Indonesia through Directorate General of Higher Education (DGHE) scholarship. I will be forever indebted for the chance to further my studies. To many lecturers at the Institute Teknologi Sepuluh Nopember (ITS) especially from the Department of Mechanical Engineering, I would like to thank them for always supporting me to pursue a doctoral degree in Germany.

I would like to thank my dearest mother, father and sister, who are being all supportive and put the utmost trust in me and to the choice I made in my life so

far. I really thank to all kind-hearted person I met during the time I spent here, for the help and consolation, for the laugh and tears we have altogether, for accompanying me during the harsh time, for being with me in this precious moment of my life and for being the people I could address as my family.

At last but not least, my sincere gratitude towards the city of Stuttgart including all its people, animals, environment and atmosphere to let me fall in love and being comfortable with.

Contents

List of Figures

LIST OF FIGURES

List of Tables

LIST OF SYMBOLS

List of Symbols

Roman Symbols

$\breve{a}_{x,y,z}$	disturbance acceleration	[m^2/s]
$\breve{v}_{x,y,z}$	disturbance velocities	[m/s]
$\tilde{u}_{i,j,k}$	Favre-averaged filtered velocity component	[m/s]
$\tilde{u}_{i,j,k}$	Favre-averaged mean velocity component	[m/s]
a	axial induction	[-]
a'	tangential induction	[-]
c	chord length	[m]
C_L	coefficient of lift	[-]
C_M	coefficient of moment	[-]
C_p	pressure coefficient	[-]
C_{DES}	DES scaling factor	[-]
$C_{p,min}$	minimum pressure coefficient	[-]
D	drag force	[N]
d	distance to the wall	[m]
E	energy spectrum	[m^3/s^2]
$f^{RANS,LES}$	weighting parameters	[-]
F_n	wall normal centrifugal force	[N]
$F_{1,2}$	blending functions	[-]
F_θ	acting force in θ-direction	[N]
F_{crr}	radial Coriolis force	[N]
F_{crs}	chordwise Coriolis force	[N]
F_{cr}	radial centrifugal force	[N]
F_{cs}	chordwise centrifugal force	[N]
F_{cv}	vortex-induced centrifugal force	[N]
$F_{X,Y,Z}$	acting force in X-, Y- and Z-directions	[N]
$F_{x,y,z}$	acting force in x-, y- and z-directions	[N]
G	spatial filter	[-]
H	vertical displacements of the separation area for 2D case	[m]
H_2	vertical displacements of the separation area for 3D case	[m]
k	turbulent kinetic energy	[m^2/s^2]
k^*	wavenumber	[m^{-1}]

LIST OF SYMBOLS

L	lift force	[N]
L_n	nacelle length	[m]
n	rotational speed	[rpm]
p	pressure	[N/m^2]
p_0	stagnation pressure	[N/m^2]
p_{inlet}	static pressure at inlet	[N/m^2]
p_{static}	static pressure	[N/m^2]
Q	vortex identification criterion	[s^{-2}]
R	blade radius	[m]
r	radius	[m]
R_n	nacelle radius	[m]
Re	Mach number	[-]
Re	Reynolds number	[-]
Ro	Rossby number	[-]
St	Strouhal number	[-]
t	time	[s]
U	X-velocity component in inertial frame of reference	[m/s]
$u''_{i,j,k}$	fluctuating velocity component	[m/s]
$u''_{i,j,k}$	sub-filter velocity component	[m/s]
U_∞	wind speed	[m/s]
$u_{i,j,k}$	velocity component	[m/s]
U_{max}	maximum velocity	[m/s]
V	total fluid velocity in rotating frame of reference	[m/s]
V_θ	circumferential velocity in inertial frame of reference	[m/s]
V_r	radial velocity in inertial frame of reference	[m/s]
V_{kin}	kinematic velocity	[m/s]
V_{rel}	relative velocity	[m/s]
$v_{x,y,z}$	local fluid velocity in rotating frame of reference	[m/s]
X, Y, Z	Cartesian coordinates in inertial frame of reference	[m]
x, y, z	Cartesian coordinates in rotating frame of reference	[m]
$x_{i,j,k}$	Cartesian coordinate	[m]
y^+	non-dimensional wall distance	[-]
y_0	y-coordinate of the airfoil wall	[m]

Greek Symbols

α	effective angle of attack	[°]
α_0	pitch angle	[°]
$\bar{\phi}$	smoothed quantity	[-]
$\bar{\rho}$	Reynolds-averaged mean density	[kg/m^3]
$\bar{\rho}$	filtered density	[kg/m^3]
β	twist angle	[°]

$\Delta C_{p,min}$	minimum pressure coefficient difference	[-]
Δt	time step size	[s]
δ	boundary layer thickness	[m]
$\Delta, \Delta_{x,y,z}$	grid size	[m]
η	ratio of the Coriolis to centrifugal forces	[-]
Γ	circulation	[m²/s]
γ	flow angle	[°]
κ	von Kármán constant	[-]
λ	speed ratio	[-]
λ_2	vortex identification criterion	[s⁻²]
μ	dynamic viscosity	[kg/(m.s)]
μ_t	turbulent viscosity	[kg/(m.s)]
ν	kinematic viscosity	[m²/s]
ν_t	kinematic eddy viscosity	[m²/s]
Ω	rotational speed	[rad/s]
ω	specific dissipation rate	[s⁻¹]
ϕ	arbitrary variable	[-]
ρ	density	[kg/m³]
σ	standard deviation	[-]
$\tau_{i,j}$	Reynolds stress	[kg/s²]
θ	azimuth angle	[°]
ε	turbulent kinetic energy dissipation rate	[m²/s³]
ζ	chordwise distance of the center of rotation	[m]

Abbreviations

AVATAR	Advanced Aerodynamic Tools for Large Rotors
BEM	Blade Element Momentum
CFD	Computational Fluid Dynamics
CFL	Courant Friedrichs Lewy
DDES	Delayed Detached Eddy Simulation
DES	Detached Eddy Simulation
DLR	German Aerospace Center
DNW	German Dutch Wind Tunnels
DTU	Denmark Technical University
DU	Delft University
Ellpsys3D	CFD flow solver
ESWIRP	European Strategic Wind tunnels Improved Research Potential
EVTM	Eddy-Viscosity Turbulence Models
FLOWer	CFD flow solver
GCI	Grid Convergence Index
GIS	Grid Induced Separation

LIST OF SYMBOLS

Gridgen	Grid generator software
HLRM	Hybrid LES/RANS Methods
HLRS	High Performance Computing Center Stuttgart
IAG	Institute of Aerodynamics and Gas Dynamics
IDDES	Improved Delayed Detached Eddy Simulation
INNWIND	European project in wind energy
JST	Jameson-Schmidt-Turkel
LAKI	Computational cluster in HLRS
LE	Leading Edge
LES	Large Eddy Simulation
LIR	Low Induction Rotor
MaPFlow	CFD flow solver
MEXICO	Model Experiments in Controlled Conditions
MEXNEXT	Research project in wind energy
MSD	Modelled-Stress Depletion
NACA	National Advisory Committee for Aeronautics
NASA	National Aeronautics and Space Administration
NREL	National Renewable Energy Laboratory
NTUA	National Technical University of Athens
Pointwise	Grid generator software
RANS	Reynolds-Averaged Navier-Stokes
RAV	Reduced Axial Velocity
RSM	Reynolds Stress Model
SA	Spalart-Allmaras
SGS	Subgrid-Scale
SHS	Shen-Hansen-Sørensen
SST	Shear Stress Transport
TE	Trailing Edge
UAE	Unsteady Aerodynamic Experiment
URANS	Unsteady Reynolds-Averaged Navier-Stokes
WENO	Weighted Essentially Non-Oscillatory
XFOIL	Boundary layer code

Abstract

Three-dimensional flow in the root area of wind turbine blades is highly complex and has been thoroughly investigated for many years due to its importance in designing more efficient rotors in the future. Despite that, a complete understanding of the phenomenon is still not yet obtained, leaving unanswered questions and contradicting conclusions in several documented literature. The difficulty in the analyses arises because the inboard area of the rotor exhibits massive flow separation at high angles of attack (α) and operates under the effect of rotational motion causing the well known three-dimensional (3D) effects or rotational augmentation where the lift coefficient increases compared to the 2D conditions. Furthermore, as the aerodynamic design is far advanced and the rotor size increases significantly nowadays, abundantly thick airfoils are employed on the blade inner sections to obtain the necessary structural stability, and this leads to even stronger separation. On this basis, rigorous and continuous investigations are essential to unveil the complexity of the 3D effects and to provide a complete understanding of the mechanism.

Two major questions are intended to be answered in the present studies by means of Computational Fluid Dynamics (CFD). The first part discusses the main mechanism on how the rotation affects the blade characteristics including complex interaction between the 3D rotating viscous and inviscid flows. In these particular investigations, inviscid calculations employing the Euler solver and viscous computations using the Reynolds-Averaged Navier-Stokes (RANS) approach were carried out on generic blades with elliptical and NACA airfoil cross-sections. The results reveal the complex mechanism of the 3D effects, showing that the phenomena are generated by a strong interaction of the inviscid and the viscous flow in the blade root area and both are of importance. The strength of the 3D effects are primarily determined by the ratio of chord to radius (c/r) for both, inviscid and viscous flow. Furthermore, the chordwise distance of the center of rotation (ζ) has a prominent impact on the 3D effects characteristics, and some recommendations relevant for the blade/airfoil design can be derived from the present findings.

Detailed studies concerning the rotational augmentation for large wind turbine rotors need to be seriously considered as thick inboard airfoils characterized by massive separation are desired to stronger contribute to power production. These evaluations are presented in the second part of the studies. Two variants of wind turbine rotors with different sizes are employed, namely the MEXICO (Model

Experiments in Controlled Conditions) and the AVATAR (Advanced Aerodynamic Tools for Large Rotors) rotors. In these evaluations, Unsteady-RANS (URANS) and Delayed Detached Eddy Simulation (DDES) were performed.

The studies carried out for the MEXICO rotor demonstrate that the employed CFD methods are able to accurately predict the load distributions of the rotor at a high wind speed case involving massive separation for the whole blade radius. The results show that rotational augmentation is insignificant if no strong radial flow presents even though massive separation occurs. This strongly indicates that the 3D effects occur only in the blade root section with a large c/r value. It was shown that the effect is prominent for $c/r \geqslant 0.1$. Additionally, the root vortices seem to have weaker influence on the pressure distribution for the MEXICO rotor than for the generic blade consisting of a thin NACA airfoil examined in the first part of the studies, and this is likely to correlate with the airfoil thickness and separation characteristics.

In agreement with the observations made on the MEXICO rotor, rotational augmentation was observed in the root area of the generic 10 MW AVATAR blade although the relative thickness of the airfoil in the root section is more than 40%. Generally, the 3D effects cause drag reduction compared to the 2D situation due to separation delay and boundary layer thinning. Despite that, it was observed that drag increases locally at some parts of the blade and the reasons have been discussed. The occurrence of downwash in the blade root area was observed, characterized by a local increase of the bound circulation and by distinct counter-rotating root vortices. Furthermore, the ratio of the Coriolis to centrifugal forces was quantified, and it was shown that the Coriolis term is dominant in the beginning of separation where the flow is radially outward.

Kurzfassung

Die dreidimensionale Strömung im Wurzelbereich von Windenergieanlagen ist sehr komplex und wird seit vielen Jahren grundlegend untersucht, da dieser Bereich für die Entwicklung effizienterer Rotoren in der Zukunft wichtig ist. Trotzdem ist ein vollständiges Verständnis des Phänomens noch nicht vorhanden. Es gibt unbeantwortete Fragen und widersprüchliche Schlussfolgerungen in mehreren dokumentierten Quellen. Die Schwierigkeit der Analysen ergibt sich daraus, dass innere Blattsektionen eine massive Strömungsablösung bei hohen Anstellwinkeln (α) zeigen und unter dem Effekt der Rotationsbewegung arbeiten. Dies verursacht die bekannten dreidimensionalen (3D) Effekte, auch bekannt als Auftriebserhöhung. Wegen des optimierteren aerodynamischen Designs und der heutzutage erheblich erhöhten Rotorgröße werden an den inneren Blattsektionen dicke Profile eingesetzt, um die notwendige strukturelle Stabilität zu erhalten, was zu einer noch stärkeren Ablösung führt. Auf dieser Basis sind gründliche Untersuchungen erforderlich, um die Komplexität der 3D-Effekte zu erforschen und ein vollständiges Verständnis des Mechanismus zu erhalten.

Zwei Hauptstudien sollen in den vorliegenden Arbeiten mittels Computational Fluid Dynamics (CFD) durchgefürt werden. Der erste Teil diskutiert den Hauptmechanismus der 3D-Effekte, wie die Rotation der Strömung die Charakteristiken des Blatts beeinflusst. Hierbei wird besonders auf die komplexe Interaktion zwischen viskosen und reibungsfreien Effekten eingegangen. In diesen Untersuchungen wurden reibungsfreie Berechnungen mit dem Euler-Solver und viskose Berechnungen unter Verwendung des Reynolds-Averaged Navier-Stokes (RANS) Ansatz auf Blätter mit elliptischen und NACA-Querschnitten durchgeführt. Die Ergebnisse veranschaulichen den komplexen Mechanismus der 3D-Effekte. Es wird gezeigt, dass die Phänomene durch eine starke Interaktion der reibungsfreien und viskosen Strömungen im Wurzelbereich des Blatts erzeugt werden und beide von Bedeutung sind. Die Stärke der 3D-Effekte wird hauptsächlich durch das Verhältnis von Profiltiefe zu Radius (c/r) für sowohl reibungsfreie als auch viskose Strömungen bestimmt. Darüber hinaus hat der Sehnenabstand des Drehmoments (ζ) eine bedeutende Auswirkung auf die 3D-Charakteristiken. Einige Empfehlungen können aus den vorliegenden Erkenntnissen abgeleitet werden, die für die Blattkonstruktion relevant sind.

Detaillierte Untersuchungen zur Auftriebserhöhung der großen Windkraftanlagen müssen ernsthaft betrachtet werden, weil ein stärkerer Beitrag zur Energieerzeugung bei dicken Profilen im Blattwurzelbereich gewünscht wird. Diese Auswertungen werden

im zweiten Teil der Studien vorgestellt. Zwei Rotor-Varianten mit unterschiedlichen Größen werden erforscht: der MEXICO-Rotor (Model Experiments in Controlled Conditions) für die kleine Anlage und der AVATAR-Rotor (Advanced Aerodynamic Tools for Large Rotors) für die große Anlage. In diesen Untersuchungen wurden Unsteady-RANS (URANS) und Delayed Detached Eddy Simulation (DDES) angewendet.

Die numerischen Untersuchungen für den MEXICO-Rotor zeigen, dass die angewandten CFD-Verfahren die Lastverteilungen des Rotors bei einem Fall mit hoher Windgeschwindigkeit mit massiver Ablösung genau vorhersagen können. Die Auftriebserhöhung ist unwesentlich, wenn es keine starke radiale Strömung gibt, obwohl eine massive Ablösung vorliegt. Dies deutet stark daraufhin, dass die 3D-Effekte nur im Blattwurzelbereich mit einem großen c/r-Wert auftreten. Es wurde gezeigt, dass die Auswirkung nur für $c/r \geqslant 0.1$ bedeutend ist. Zusätzlich haben die Wirbel im inneren Bereich des MEXICO-Rotors einen schwächeren Einfluß auf die Druckverteilung als die Wurzelwirbel der dünnen Blätter mit NACA-Querschnitt, die im ersten Teil der Studien untersucht wurden. Dies korreliert wahrscheinlich mit der Profildicke und den Ablöseeigenschaften.

Ähnlich wie die Beobachtungen am MEXICO-Rotor findet Auftriebserhöhung im Wurzelbereich des generischen 10 MW AVATAR-Rotors statt, obwohl die Dicke des Profil-Abschnitts mehr als 40% beträgt. Allgemeinen verringert sich der Widerstand im Vergleich zu den 2D-Situationen auf Grund der 3D-Effekte. Dies wird verursacht von einer Verzögerung der Ablösung und einer Ausdünnung der Grenzschicht. Trotzdem sind einige Blattregionen durch lokal erhöhten Widerstand gekennzeichnet. Der Abwind im Blattwurzelbereich wurde untersucht. Dieser korreliert mit der lokalen Erhöhung der gebundenen Zirkulation und mit den gegenläufigen Wurzelwirbeln. Weiterhin wurde das Verhältnis der Coriolis- zu Zentrifugalkräften quantifiziert. Es wurde gezeigt, dass der Coriolis-Term am Anfang der Ablösung dominiert, da die Strömungsrichtung radial nach außen ist.

Chapter 1

Introduction

1.1 Motivation

Nowadays, as the aerodynamic design of wind turbines is far advanced and as the inboard region with thick airfoils is desired to stronger contribute to power production, better understanding of the three-dimensional flow over the turbine is needed for designing more efficient rotors. One key factor needed to be considered is three-dimensional (3D) effect widely known as rotational augmentation. It becomes a serious matter because the design of wind turbine blades typically relies on simple aerodynamic models based on the blade-element momentum (BEM) theory which uses only the two-dimensional (2D) airfoil data. The BEM methods are usually sufficient in predicting the wind turbine loads near the design point [1], but under-predict the forces in stalled conditions especially in the root region. For example, the measured power from the NREL Combined Experiment (Phase II) turbine exceeded the BEM predictions by approximately 15-20% [2]. The inaccuracy of the BEM models stems from the fact that the three-dimensionality of the flow is not taken into account in the formulation, especially near the blade root and tip regions. The inboard region is usually operating at high angles of attack (α) and often in post-stall conditions, which in turn enhance the three-dimensionality of the flow. It is clear that three-dimensional effects are important and have to be included in the aerodynamic calculations to correctly predict the loading and performance of wind turbines.

Despite the importance of the 3D effects, a complete understanding of the phenomena is still not yet realized. Numerous examinations have been done by various authors using experiment, mathematical modelling and numerical simulations. However, a clear mechanism of the phenomena is still not well understood. Complex interaction between the inviscid and viscous flows at the root area is not yet explored. Furthermore, the centrifugal and Coriolis forces generally claimed as the source of the effects are not yet evaluated thoroughly. On this basis, a careful examination of the phenomena which can explain the mechanism is required.

In this chapter, studies of the 3D effects on wind turbine aerodynamics are reviewed

and the objectives of the present research are clarified towards the end of this chapter which attempt to unveil the complexity of the 3D effects.

1.2 State of the Art

The studies of the 3D effects were started since Himmelskamp [3] observed deviations of the 3D lift for propeller blade sections compared to the 2D airfoil database. This phenomenon was attributed to stall delay due to radial flow [4]. Extensive experimental, theoretical and numerical investigations were then carried out [3, 5–11]. The majority was dealing with development of the radial velocity [6, 8–11], and how the radial velocity component influences the radial pressure gradient. Considerable mathematical difficulties in calculating rotating blades are encountered even for the inviscid flow, especially when the blades are working as lifting surfaces with complicated patterns of trailing vorticity [5]. Sears [6] solved the potential flow problem for rotating cylindrical blades. The formulations are based on the Euler equations in the rotating frame of reference [7]. It was explained that the spanwise flow depends only on the inviscid velocity distribution of the corresponding two-dimensional flow. It was shown later by Fogarty and Sears [8] that the advancing motion of the blade such as in propellers does not change the solution of the flow in radial direction.

Following these theoretical attempts for the inviscid case, some studies were carried out by considering the fluid viscosity in the mathematical formulations. However, due to limitations of the computer performance at that time, numerical studies on rotating blades were limited to the analysis of laminar boundary layers [4, 8, 9, 12–14]. Early studies on the 3D laminar boundary layer of rotating blades were performed in the middle of the 20th century and concluded that the rotation has a small influence on the flow, e.g., the one performed by Fogarty [9], Tan [10], and Rott and Smith [11]. These studies were intended to obtain velocity distributions at some chordwise and spanwise positions. Analytical approaches were used to solve the Navier-Stokes equations by introducing some simplifications. The most important simplifying assumption made (in addition to the usual boundary-layer assumptions) is that the length of chord, on which the boundary layer develops, is small in comparison with its distance from the center of rotation [9, 11]. Simplifications introduced by this concept made calculations of the 3D boundary layer over rotating blades possible [5]. The general treatment of the flow made use of the small perturbation procedure, implying that the boundary layer will be only slightly three-dimensional. As a result, a linear inhomogeneous differential equation for the crosswise velocity component was established (while those in chordwise and wall normal directions are exactly the same as in the two-dimensional boundary layer). The two-dimensional behaviour of the flow in streamwise and normal directions was similar to that found by Prandtl [15], Jones [16], and Sears [17] for the case of a yawed infinite wing. The conclusion made during these early studies [9–11] contradicted the engineers impression that the 3D effects are strong on rotating blades [3, 5, 15]. Fogarty [8] explained this discrepancy as the invalidity of the models downstream the

separation line or in the separated flow domain. Tanner and Yaggy [18] investigated the boundary layer characteristics of a hovering rotor aimed to examine the rotational effects on laminar - turbulent transition. The results showed that the rotation does not influence the position of transition and no secondary radial flow was observed. Despite that, the study was only performed for attached flow condition, which again indicates that Fogarty's conclusion and suggestion are correct.

The above studies led to the conclusion that the strong 3D effects in the Himmelskamp's experiment might come from the separated boundary layer. This explanation was supported by McCroskey and Yaggy [4] (using similar assumptions as Fogarty), stating that the rotational effects become increasingly important as the chordwise pressure gradient becomes more adverse. The rotation can have a strong influence in regions of incipient separation, but elsewhere the boundary layer generally resembles the viscous flow over a swept wing. The crossflow was observed to delay separation on the retreating side of the rotor disk for a helicopter in forward flight [4]. Furthermore, it was shown that the structure of the spanwise flow component depends upon whether the primary flow is accelerating or decelerating. This observation was supported by Banks and Gadd [12].

In the mid 1970's the modern development of wind turbines took its beginning [19]. Further experiments on the 3D effects following Himmelskamp's [3] have been carried out for wind turbine rotors. Milborrow and Ross [20] observed that the effective lift coefficient for a wind turbine blade section in the near hub area was higher than that obtained from 2D data in their wind tunnel study. Savino and Nyland [21] visualized the flow direction on the surface of a full-scale rotor using balanced wind vanes. Upstream of the separation line, the flow was attached in chordwise direction, but a strong radial flow was observed within the separated region. This was confirmed by Ronsten [22] and Bruining et al. [23].

At this stage, it was already concluded that the centrifugal and Coriolis forces are the main sources of the 3D effects. The centrifugal force transports the separated flow near the root, creating a strong radial flow component and reducing the boundary layer thickness [24, 25], the so-called centrifugal pumping. It shall be noted that the centrifugal force is felt by the fluid particle for all flow regimes but has the strongest effect within the separation area. This effect occurs if the flow is locally disturbed by the presence of the blade. For the inviscid part of the flow, the pressure gradient is responsible for this behaviour. The Coriolis force occurs as a consequence from the generated radial flow component and is believed to act in chordwise direction, delaying the occurrence of separation. Sørensen [19, 26] employed a viscous-inviscid interaction model to solve rotating blade problems. The results showed that the position of the separation line appeared to be the same as for the non-rotating 2D conditions. The difference became noticeable as stronger separation was encountered. However, the code was incapable to solve the problem for sectional angle of attack higher than 22°. Thus, predictions of the post stall conditions were not possible at that time. Snel [27] presented an order-of-magnitude analysis of the different terms in the 3D boundary layer equations for a rotating slender blade in terms of the local chord-to-radius ratio c/r [28].

1. INTRODUCTION

It was observed that the radial convective acceleration terms are of the order $(c/r)^{2/3}$ compared to the main terms which are of order unity. A semi empirical correction for the 2D lift polar was proposed [27], employing the ratio of the local chord to radius as the main parameter. The outcome was supported by Shen and Sørensen [1] and by Chaviaropoulos and Hansen [29] using quasi 3D Navier-Stokes computations. Du and Selig [30, 31] performed studies using simplified 3D boundary-layer equations in integral form and assumed a velocity profile, similar to the one used by Banks and Gadd [12]. It was demonstrated that the Coriolis force effect is stronger than the centrifugal force. Separation delay was observed with increasing chord to radius ratio and the rotational speed. This conclusion was confirmed by Dumitrescu *et al.* [32–34], Martínez *et al.* [35] and García *et al.* [25].

Wood [36] studied a rotating wind turbine blade using an inviscid panel code and compared the results with the experimental data from Ref. [37]. The investigation demonstrated that the rotational augmentation is actually an inviscid effect. The viscosity was neglected in the calculations and the 3D effects were still observed. The rotation reduces the minimum inviscid pressure peak at the blade root, changing considerably the inviscid pressure distribution in which a much smaller adverse pressure gradient was shown compared to the inviscid 2D conditions. This observation shows that separation shall be delayed because the chordwise pressure gradient in the 3D rotor is weaker than in the corresponding 2D conditions at the same angle of attack. It was concluded that the impacts of the centrifugal and the Coriolis forces on the boundary layer of the rotating blade are of minor importance. Prior to Wood [36], examples of calculations using inviscid panel codes on rotating blades were reported by Preuss *et al.* [38], Valarezo and Liebeck [39], and Hess and Valarezo [40]. The stall delay was inferred to result from changes to the inviscid flow and is controlled primarily by the local solidity of the blade [36].

The explanation regarding the inviscid effect however contradicted the studies on viscous boundary layer of rotating blades such as in [12, 25, 30–35, 41]. According to these studies, the rotational augmentation is a consequence of the Coriolis and centrifugal forces acting within the boundary layer. There was a lively debate at that time as Dumitrescu and Cardos [32, 41] stated that Wood [36] was mistaken by saying without doubt that the inertial forces within the 3D boundary layer are unimportant. They observed that the stall delay depends slightly on the reduced pressure effect and mainly on the accelerated boundary-layer flow effect by the Coriolis force. It was concluded that the inviscid nature or the explanation of stall delay assumed by Wood [36] is incorrect, the potential approach being unsuited to describe a phenomenon with complex dynamics. Furthermore, in their more recent paper [42] they demonstrated that as the blade adverse pressure gradient decreases, the separated area in the inner blade part decreases. Despite that, Wood [43] replied to their disagreement for the inviscid effect. The blade analysis of Ref. [36] was undertaken at the state where the knowledge of stall delay was poor. As it was more difficult to analyse boundary layer flows, Wood started from the fundamental assumption that it is not necessary to seek the explanation for the stall delay within the boundary layer if a significant

reduction occurs in the adverse pressure gradient on the suction surface of the blade when compared to an airfoil at the same angle of attack. This was motivated by two important considerations: (1) The boundary layers simply respond to the imposed pressure gradient. (2) The Coriolis force which becomes zero at the blade surface is unlikely to act as effectively as the adverse pressure gradient, which is felt equally across a boundary layer in the absence of significant streamline curvature.

Measurements conducted in the NASA Ames 24.4 m x 36.6 m (80 ft x 120 ft) wind tunnel known as the Unsteady Aerodynamic Experiment (UAE) have led to a better understanding of the 3D post stall aerodynamics of wind turbines [44–47]. Schreck and Robinson [48] evaluated surface pressure measurements from the NREL UAE wind turbine blade. It was shown that the rotational augmentation is independent of the Reynolds number influence but depends strongly upon the spanwise surface pressure gradients on the blade. Schreck [49] demonstrated a strong correlation of the local inflow condition to the characteristics of the normal force coefficient standard deviation (σ_{Cn}) which determines the blade flow field structures under rotational augmentation. In his subsequent study, Schreck *et al.* [50] compared the NREL UAE Phase VI blade to the MEXICO (Model Experiments in Controlled Conditions) rotor and observed discrepancies of the 3D post stall characteristics between these two rotors. The pressure coefficient (C_p) distribution for the UAE Phase VI blade implied a leading edge separation followed by shear layer impingement and it was highly responsive to increasing wind speed for the inboard blade sections [49, 51], but the C_p distribution for the MEXICO rotor consistently showed the characteristics of trailing edge separation. However, a strong correlation could be depicted from the variations of σ_{Cn} with respect to α [50].

The steady increase in computational performance over recent years has enabled Computational Fluid Dynamics (CFD) calculations on rotating wind turbine blades, and more detailed explanations of the 3D complex flow features involving the rotation can be done. Examples for rotor calculations with fully turbulent boundary layer were given by Sørensen *et al.* [52], Johansen *et al.* [53], Duque *et al.* [54], Herráez *et al.* [55], Bangga *et al.* [56, 57], Zahle *et al.* [58] and Kim *et al.* [59] while calculations with natural transition were given by Johansen and Sørensen [60], Laursen *et al.* [61], Gross *et al.* [62], and Troldborg *et al.* [63]. The studies confirmed that the 3D aerodynamic loads on a rotating blade are higher than in the non-rotating case (in both fully turbulent and transitional cases), mostly for the inboard sections and separated flow conditions [24]. Duque *et al.* [54] performed computations of the NREL Phase II blade using a lifting line code and a CFD code that made use of overset grids and an algebraic turbulence model known as Baldwin-Lomax [64]. The results demonstrated that the CFD code could predict the stalled rotor performance quite well while the lifting line method failed to capture the rotor performance at high wind speeds, even with the inclusion of a stall delay model. The CFD predictions of a wind turbine rotor using two-equation turbulence models, namely Wilcox $k - \omega$ and SST $k - \omega$, were carried out by Le Pape and Lecanu [65]. The SST $k - \omega$ model was superior in predicting the aerodynamic polar, but both models hardly showed a good prediction

of the post stall regime. Sørensen *et al.* [52] performed CFD calculations on the NREL Phase VI blade using SST $k - \omega$ with fully turbulent boundary layer and a good agreement against experimental data was achieved. Johansen *et al.* [53] simulated the same turbine in parked condition using Detached Eddy Simulations (DES) as well as the RANS (Reynolds-Averaged Navier-Stokes) SST $k - \omega$ turbulence model. The DES results gave more information on the 3D flow structures than the one predicted by the RANS, but the overall aerodynamic characteristics of the blade were not better predicted. Johansen and Sørensen [60] extracted the aerodynamic characteristics of the 3D CFD rotor computations on three stall-regulated wind turbine rotors as test cases. With a sufficiently accurate CFD computation, it was possible to reproduce the airfoil characteristics under rotational augmentation without using empirical stall corrections models. The other examples of CFD studies on rotational augmentation were given Guntur and Sørensen [66] and Herráez *et al.* [55] on the MEXICO rotor and by Bangga *et al.* [56, 57, 67] on the AVATAR blade.

As the need of wind power is remarkably increasing nowadays, the size of the rotor blade is also increasing as a consequence to generate more power. It leads the turbine to operate at significantly higher Reynolds number than smaller turbines. Contrasting Schreck and Robinson [48], Du and Selig [31] concluded that the rotational augmentation is less important for large wind turbines because the Reynolds number is remarkably larger. However, it should be kept in mind that the tip speed ratio of the larger turbines is comparable with the smaller one, resulting in the congruous value of the Rossby number which influences the 3D effects according to Dumitrescu and Cardos [32]. This argument was supported by Herráez *et al.* in their study [55]. Furthermore, larger rotors show even thicker inboard sections than the smaller rotors. This promotes stronger separation [68, 69] which leads to the presence of a radial flow component. Troldborg *et al.* [63] conducted experimental and numerical studies on a megawatt wind turbine blade, showing that the pressure distribution was affected by the rotation. Bangga *et al.* [56] performed a CFD evaluation and grid studies of the generic 10 MW AVATAR rotor operating near rated condition. The lift coefficient was observed to have a remarkably higher value than in 2D conditions at the inboard blade region and the size of the separated zone was significantly reduced due to 3D effects, similar to the observation made by Chaviaropoulos and Hansen [29]. On the same turbine, Bangga *et al.* [57] further investigated the rotational augmentation for mild turbulent inflow conditions and it was observed that a small turbulence level has only little influence on the 3D effects. Schreck *et al.* [51] investigated the field test measurements of a 2.3 MW wind turbine equipped with thick flatback airfoils in the inboard blade region. The use of thicker airfoils and enhanced trailing edge thicknesses was observed not to hinder the rotational augmentation. A significant increase of aerodynamic forces by factors as high as 2-3 relative to the results at stationary 2D conditions were observed. Zahle *et al.* [58] derived 3D airfoil characteristics by CFD calculations on the DTU (Denmark Technical University) 10 MW Reference Wind Turbine for aero-elastic simulations. The aerodynamic polars were extracted and used in BEM calculations. The results show a significant

improvement on the sectional loads compared to the 3D correction model from Bak *et al.* [70], but the mechanical power and thrust did not so much improve as the inboard region has small lever-arm. Recently, Troldborg and Zahle [71] applied vortex generators in the inboard region of the same blade as [58] to improve the aerodynamic performance of the blade by delaying the occurrence of separation. It was shown in their later studies [72] that the 3D effects at high angles of attack are alleviated by the vortex generators.

1.3   Scope and Aims

The flow characteristics in the root area of wind turbine blades are very complex as they involve three-dimensionality, separation and rotational motion of the blade. The phenomena have a strong influence on the aerodynamic characteristics that differ significantly from the routinely observed two-dimensional airfoil. Rigorous investigations are necessary to gain a fundamental basis in understanding the phenomena and to design more efficient blades in the future.

The aims of the present studies are to provide detailed examinations on the 3D effects for wind turbine rotors and a complete picture of the mechanism. High fidelity Computational Fluid Dynamics (CFD) approaches are to be employed in these studies. To sum up, two main research questions are listed below:

- As already discussed in Section 1.2, there are still open questions regarding the main source of the 3D effects. These issues shall be addressed particularly in the mechanism on how rotation affects the blade pressure distribution and in interaction of the 3D rotating viscous and inviscid flows which is still debatable up to now.

- As the blade size increases nowadays, three-dimensional effects for rotors with different sizes need to addressed. The aerodynamic characteristics of the blade sections shall be compared to the corresponding two-dimensional conditions to obtain an impression about the strength of the effects. A great challenge in examining the 3D effects for the large rotor stems from the fact that abundantly thick airfoils with the relative thickness of more than 40% are employed in the blade inboard area. The centrifugal and Coriolis forces were generally assumed as the source for the 3D effects, and quantification of these forces needs to be carried out. Furthermore, deeper studies are necessary in the relation between the aerodynamic loads and root trailing vortices shed downstream of the blade.

1.4   Thesis Outline

The thesis is composed of six chapters that are organized as follows:

- **Chapter 1** presents a short background along with reviews of the current state of the art studies on 3D rotor aerodynamics and explains the main focus of the

works.

- **Chapter 2** provides information about the CFD code used in the studies and reviews some turbulence models alongside with their limitations. The examined rotor blades, generation of the computational mesh and extraction of the angles of attack are described in this chapter.

- **Chapter 3** describes a complete picture of the root cause for the 3D effects in order to answer contradicting conclusions related to the inviscid and viscous effects. Recommendations relevant to the airfoil/blade design are given in this chapter.

- **Chapter 4** presents the evaluations of the 3D effects for a small isolated wind turbine rotor at a high wind speed case. The results are compared to available measurement data to demonstrate the accuracy of the CFD computations.

- **Chapter 5** examines the 3D effects occurring in the root area of a large wind turbine blade constructed by very thick airfoils. The evaluation of the root vortices effects on the local aerodynamic loads and quantification of the centrifugal to Coriolis forces are given.

- **Chapter 6** presents the main conclusions of the studies.

Chapter 2

Research Methodology

2.1   Numerical Simulations

2.1.1   The FLOWer Code

The FLOWer code solves the compressible, three-dimensional Euler or Navier-Stokes equations. It uses a finite volume formulation on block-structured meshes and is designed to simulate flows around complex aerodynamic configurations. FLOWer has been directly evolved from the DLR CEVCATS code [73] and is being further developed in close cooperation with the German aeronautical industry and universities in the framework of the MEGAFLOW project [74–76]. The main goal of FLOWer is the efficient and accurate simulation of complete transport aircraft at cruise and take-off/landing conditions. Although the flow modeling and the numerical algorithms are mainly designed to support this type of application, the FLOWer code can be used for many other flow problems, such as the flow around helicopters or the design of airfoils and wings. During the last years, the code was continuously further developed at the Institute of Aerodynamics and Gas Dynamics (IAG) - University of Stuttgart for wind turbine [59, 77, 78] and helicopter [79–81] applications. These involve actuator line and consideration of inflow turbulence. For scale resolving computations of wake and transporting the inflow turbulence, the Weighted Essentially Non-Oscillatory (WENO) scheme [82] as well as Delayed Detached Eddy Simulation (DDES) and Improved Delayed Detached Eddy Simulation (IDDES) [83] were implemented at the institute [59, 77–81, 84].

FLOWer is capable of calculating flows on moving grids (translation and rotation) under steady and unsteady flow conditions. In this case, the compressible Navier-Stokes equations are solved, transformed into body fixed rotating and translating reference frames, and the equations are formulated in terms of absolute velocities. The overset (Chimera) method can be used within overlapping meshes, which can significantly simplify the generation of the computational grid. By default, a central cell-centered Jameson-Schmidt-Turkel (JST) [85] method is used for flux computation with second order spatial accuracy on smooth meshes. The method

utilizes central space discretization with artificial dissipation computed with respect to the grid cell aspect ratio. However, it shall be noted that the aforementioned WENO scheme is available and can be chosen if high order (up to 7th order) numerical computations are required. The time integration is carried out by an explicit hybrid 5-stage Runge-Kutta scheme. For steady state calculations, the integration is accelerated by the techniques of local time stepping, enthalpy damping for inviscid flows and implicit residual smoothing. This is made possible by the implicit discretization which helps to bypass the time step limitation of the explicit schemes, *i.e.,* a very small time-step is required since the CFL constraints must be fulfilled for all cells. Jameson has developed a very efficient multigrid-driven implicit approach for the solution of the unsteady Euler equations [86], namely the dual-timestepping method. Using central differences in space and an implicit multistep discretization in time, a large set of simultaneous non-linear equations is formed and marched to steady-state in pseudo-time through a multigrid algorithm within each physical time step. This approach has been applied to the solution of the unsteady Navier-Stokes equations with great promise.

2.1.2   Turbulence Modelling

2.1.2.1   Basic Concept

RANS

In the prediction of engineering flows, turbulence presents considerable difficulties and becomes an obstacle to the accuracy and applicability of CFD methods. Although direct numerical simulation (DNS) allows the resolution of the complete range of turbulent scales, the computational cost renders this approach unfeasible for the time being. A reasonable simplification of this issue has led to the development of the Reynolds-Averaged Navier-Stokes (RANS) methods. In this approach, the solution variables in the instantaneous Navier-Stokes equations can be decomposed into the mean and fluctuating components. In cases where the density is not constant, it is advisable to apply the density (mass) weighted or Favre decomposition [87–89]. The most convenient way is to employ Reynolds averaging for density and pressure, and Favre averaging for other variables such as velocity, internal energy, enthalpy and temperature [89]. Application of this approach for the velocity vector u_i can be given as

$$u_i = \tilde{u}_i + u_i'' \tag{2.1}$$

where $\tilde{u}_i$ is the mean and u_i'' is the fluctuating velocity components. The average of the fluctuating part is zero, *i.e.,* $\widetilde{u_i''} = 0$. Substituting expressions of this form for the flow variables into the instantaneous continuity and momentum equations yields the averaged momentum equations. They can be written in Cartesian tensor form as

$$\frac{\partial \bar{\rho}}{\partial t} + \frac{\partial}{\partial x_i}(\bar{\rho}\tilde{u}_i) = 0 \tag{2.2}$$

$$\frac{\partial}{\partial t}(\bar{\rho}\tilde{u}_i) + \frac{\partial}{\partial x_j}(\bar{\rho}\tilde{u}_i\tilde{u}_j) = -\frac{\bar{p}}{\partial x_i} + \frac{\partial}{\partial x_j}\left[\mu\left(\frac{\partial \tilde{u}_i}{\partial x_j} + \frac{\partial \tilde{u}_j}{\partial x_i}\right)\right] - \frac{\partial}{\partial x_j}\tilde{\tau}_{ij}^{RANS} \quad (2.3)$$

which are called the Favre- and Reynolds-Averaged Navier-Stokes equations. The left hand side of Equation (2.3) represents the formulation of the fluid momentum, involving its variation in time by the mean flow, which is balanced by the mean pressure gradient, viscous stresses and apparent stress $\tilde{\tau}_{ij}^{RANS}$ commonly known as the Reynolds stress (Favre-averaged) on the right hand side of the equation. The latter, however, cannot be obtained directly and needs to be modelled in order to close the equation. The Boussinesq hypothesis [90] is commonly used to relate the Reynolds stress with the mean velocity gradients

$$-\tilde{\tau}_{ij}^{RANS} = \mu_t \left(\frac{\partial \tilde{u}_i}{\partial x_j} + \frac{\partial \tilde{u}_j}{\partial x_i}\right) - \frac{2}{3}\left(\bar{\rho}\tilde{k} + \mu_t \frac{\partial \tilde{u}_k}{\partial x_k}\right)\delta_{ij} \quad (2.4)$$

where μ_t is the "turbulent" viscosity introduced as a new parameter. Many turbulence models are developed based on this relation through the modelling of the turbulent viscosity. It is also common to recall these models as the eddy-viscosity turbulence models (EVTM). The Spalart-Allmaras (1-equation), $k - \varepsilon$ or the Wilcox [91] and Menter SST $k - \omega$ (2-equation) models are the examples of EVTM that are widely used for various industrial purposes. In many cases, models based on the Boussinesq hypothesis perform very well, and the additional computational expense of the Reynolds stress model (RSM) is not justified. However, the RSM (7-equation) is clearly superior for situations in which the anisotropy of turbulence has a dominant effect on the mean flow, such as cases with highly swirling flow component and with stress-driven secondary flows.

LES

The main idea behind Large Eddy Simulation (LES) is to reduce the computational cost compared to DNS by resolving only the large eddies and by ignoring the smallest length scales, which are the most computationally expensive to solve. LES is often introduced based on the filtering concept [92, 93]. A spatial filter (G) is applied to an arbitrary variable ϕ yielding the smoothed counterpart $\tilde{\phi}$ with scales smaller than the filter size being removed [92]. Usually, the filter size is set as close as possible to the step size of the grid Δ to benefit from the refined resolved scales for finer grid resolution. Thus, the ultimate limit of $\Delta \to 0$ implies that the modelled part of LES vanishes and the computations become DNS without turbulence model.

Applying the filtering procedure for the velocity and pressure fields together with the Favre-averaging procedure and substituting the results in the momentum equation yield

$$\frac{\partial}{\partial t}(\bar{\rho}\tilde{u}_i) + \frac{\partial}{\partial x_j}(\bar{\rho}\tilde{u}_i\tilde{u}_j) = -\frac{\bar{p}}{\partial x_i} + \frac{\partial}{\partial x_j}\left[\mu\left(\frac{\partial \tilde{u}_i}{\partial x_j} + \frac{\partial \tilde{u}_j}{\partial x_i}\right)\right] - \frac{\partial}{\partial x_j}\tilde{\tau}_{ij}^{LES} \quad (2.5)$$

The last term of Equation (2.5) describes the impact of subfilter scales on the resolved motion which needs to be modelled. This term is usually called subgrid-scale

(SGS) model. Similar to RANS, SGS turbulence models usually employ the Boussinesq hypothesis [90] in which the turbulent viscosity is used like in the Smagorinsky model [94].

Hybrid LES/RANS

Structural similarity of the RANS and LES equations show that the development of LES generally is based on the principal knowledge of the RANS model [92]. Several attempts to couple RANS and LES, mainly to reduce the computational expense coming from the LES simulations, were carried out. The combined models, according to Fröhlich and von Terzi [92], can be classified as the segregated and unified models. The first mentioned model works by decomposing the entire domain into LES and RANS zones. In this model, however, the resolved quantities are not continuous in the interface between LES and RANS. According to Speziale [95, 96], a good unified turbulence model should possess at least three properties: (1) in the coarse grid limit, the model should act as RANS, (2) for well resolved zones, a DNS should be recovered and (3) no explicit filtering or averaging should be applied. The unified model can be further classified as blended and interfaced models. The blended model is constructed by adding weighting parameters (f^{RANS} and f^{LES}) in the sum of RANS and LES models according to

$$\phi_{ij}^{model} = f^{RANS}\phi_{ij}^{RANS} + f^{LES}\phi_{ij}^{LES} \qquad (2.6)$$

where ϕ can be a model term in the momentum equation like the turbulent viscosity or a term in the secondary equation of the turbulence model [92]. The application of this model can be found in [97], where the Menter SST turbulence model is used as the RANS basis. The other form of the blended model is the damping of a RANS model (FSM) in which the damping depends on the grid resolution [96]. The RANS model is responsible in the modelling of all turbulence and depends only on the physical quantities.

On contrary, rather than adding a damping, the interfaced model applies pure LES in one domain and pure RANS in the rest of the domain which is possible by switching the model term at the interface [92]. The momentum transport equation, however, remains the same. Accordingly, the resulting velocity field is continuous at the interface. This idea is one main distinction with the segregated coupling. Detached Eddy Simulation (DES) approach is one example of the interfaced model that is widely employed and developed for engineering purposes. The model was firstly introduced by Spalart *et al.* [98] by combining LES and the Spalart-Allmaras (SA) RANS model [99]. The SA turbulence model is turned into LES mode by modifying the eddy-viscosity destruction term in which the wall distance is replaced by a length proportional to Δ. Thus, it becomes a SGS model. Despite the fact that a RANS model term is used, it does not hinder the resulting hybrid model to capture the unsteadiness of the flow field. In fact, even with the stationary statistics, the DES computations are unsteady close to the wall as a result from the fluctuations of the outer flow. The model has been used and examined for various types of separated flows and qualitatively showed

an improvement in capturing the eddy structures, but quantitative comparisons were rarely conducted [92].

In DES, the solution of the outer flow region should resolve at least 80% of the turbulent kinetic energy to become a true LES [100]. Thus, the solution in RANS region usually exhibit weak oscillations. The region between these areas where the wall distance, or an equivalent parameter used to define RANS-LES transition, is comparable with the grid spacing, is critical because the DES term can be turned on too early or even within the boundary layer area. This issue has forced the CFD community to use shielding so that the LES mode cannot penetrate too close to the wall inside the boundary layer. Menter and Kuntz [101] proposed an idea for this purpose by employing the SST $k - \omega$ [102] blending functions, F_1 and F_2, in switching between the RANS and LES modes. One year following this idea, Spalart *et al.* [103] developed Delayed Detached Eddy Simulation (DDES) by revising the DES formulation. However, the modification is universal and not limited only to the Menter SST model [102] as long as the model employs a turbulent viscosity. In fact, they developed the model based on the SA turbulence model [99]. The parameter r, which defines the ratio (squared) of a model length scale to the wall distance, is redefined in the model as

$$r_d = \frac{\nu_t + \nu}{\sqrt{(\partial \tilde{u}_i/\partial x_j)(\partial \tilde{u}_i/\partial x_j)}\kappa^2 d^2} = \frac{\nu_t + \nu}{S\kappa^2 d^2} \tag{2.7}$$

where ν_t is the kinematic eddy viscosity, ν the kinematic viscosity, κ the von Kármán constant, and d the distance to the wall. This parameter is equal to unity in the log-layer zone and gradually reduces to zero toward the boundary layer edge [99]. This term is used in the f_d function employed in the dissipation length scale term

$$\tilde{d} = d - f_d \max\{0, d - C_{DES}\Delta\} \tag{2.8}$$

where

$$f_d = 1 - \tanh[(8r_d)^3]. \tag{2.9}$$

By doing so, DES is prevented from too an early switch to LES mode. This model has recently been implemented in the FLOWer code and was presented in [77, 78].

2.1.2.2   Limitation of the Turbulence Models

It has been agreed that it was too naive and dangerous to assume the validity of a turbulence model in the wide range of flows [104]. In this section, the limitation of the turbulence models discussed above will be pointed out particularly for RANS, LES, DES and DDES.

The main issue for the RANS models is that all turbulence are modelled regardless the grid size. By refining the grid resolution, the computed RANS results are converged to a certain value implying that the ultimate accuracy of a RANS model is determined by the accuracy of the turbulence model itself. Thus, a RANS method is sufficient

if the objective of the study is to capture the mean flow with acceptable precision. The validity of RANS for a case can be seen from the "scale separation" or "spectral gap" point of view [92]. A clear scale separation occurs when the unsteadiness of the statistical mean properties is triggered by the external sources, not by the internal instabilities of the flows. In wind turbine rotor simulations, the external unsteadiness is caused by the rotor rotation or wind shear while the internal instabilities can come from the high frequency fluctuations of flow separation due to pressure gradient on the blade surface. If the global flow characteristics are of interest, thus, a direct interaction between the first and the latter cases can be neglected and modelling assumptions of RANS are valid.

However, in other situations, dominated by large-scale anisotropic vortical structures like wakes of bluff bodies, the average quantities are often less satisfactory when a RANS model is employed [92]. For example, in modelling 3D flow separation around a square cylinder investigated in [105], the URANS solution which developed in the simulation was seen to be mostly two-dimensional and did not produce the correct Strouhal number (St) [92]. The fact that St is insensitive for most bluff body flows leads to a doubt whether the phenomena are correctly modelled. Furthermore, Weihing *et al.* [78] also documented that even though the mean forces of a generic wind turbine rotor predicted by URANS and DES approaches are similar, the load fluctuation and its resulting spectra are completely different. According to Fröhlich and von Terzi [92], the use of URANS can hence only be advocated in cases of clear scale separation as described in the preceding discussion.

The basic strategy of the eddy resolving methods is to resolve most of the turbulent kinetic energy of the flow and modelling most of the dissipation [92]. This idea comes from the fact that the turbulent kinetic energy is determined by the large turbulent scales while most of the dissipation occurs at smaller scales. Leonard [93] showed that simulating all the eddy structures are generally not practical but most information of interest can be obtained by resolving the motion of the large-scale, energy containing eddies. For this purpose, the LES and DES simulations are carried out instead of DNS. Despite that, LES is still within the factor of 10-100 times more expensive than RANS simulations [106]. This is particularly true because LES needs to resolve at least 80% of the turbulent kinetic energy to warrant reliable results [100]. Ducros *et al.* [107] and Akselvoll and Moin [108] reported that their LES simulations were only 1/10 and 1/50, respectively, that of a DNS. Spalart *et al.* [98] estimated the cost for these computations and showed that the gains were only a factor of $10^{1/4}$ and $50^{1/4}$, respectively, in each direction including time. Furthermore, LES often has an issue concerning near wall flows where the grid is strongly anisotropic so that the choice of the grid scale definition becomes crucial [92].

In Figure 2.1, the resolved and modelled parts of different turbulence model strategies are shown. It can be seen that RANS models all structures regardless of the size while no model is employed for DNS computations. While LES needs to resolve most of the turbulent kinetic energy resulting in a high computational effort, hybrid LES/RANS methods like DES are in between RANS and LES. The main issue for the
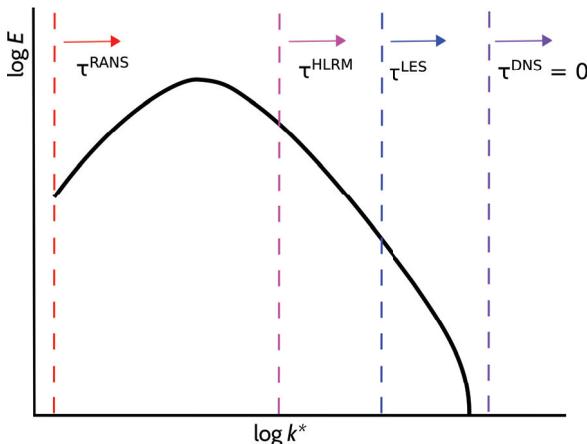
Figure 2.1: Typical turbulent kinetic energy spectrum of the idealized isotropic turbulence as a function of wavenumber k^*. The arrows mark the region where the turbulent scales are "modelled" by each simulation strategy. In case of DNS, no model is applied and all scales are resolved.

original DES is the grey area where the grid is small enough so that the hybrid model switches to LES but not fine enough to resolve the turbulent structures. This leads to Modelled-Stress Depletion (MSD) which has been the most significant practical issue and worse to deal with than initially anticipated [109]. Under this particular circumstance, the DES limiter reduces the eddy viscosity and, therefore, the modelled Reynold stress (τ_{ij}^{model}) without any sizeable resolved stress to restore the balance [103]. Caruelle [110], Deck [111] and Menter and Kuntz [101] have emphasized that severe cases of MSD could lead to Grid Induced Separation (GIS). The DDES method proposed by Spalart *et al.* [103] is intended to prevent this issue by delaying the switch of the LES region further away from the wall. On the other hand, this method exploits a history effect of the numerical computations which has consequences in term of the uniqueness of solutions [109]. This phenomenon perplexed some authors like Fröhlich and von Terzi [92] who observed that mean flow characteristics of the DDES solutions are sensitive towards the initial condition. For instance, if the flow starts from the RANS state, where the eddy viscosity is high and the internal flow instabilities are weak, the results will remain in that state until a steady state condition is reached. In contrary, if the flow starts in LES mode, the solutions settle into a statistically steady condition. Spalart [109] emphasized that both solutions are valid and such non-uniqueness are not uncommon in RANS practice, for example the hysteresis properties of the the flow over airfoils near maximum lift which exist in the

real-word situations and in CFD.

2.1.3 Blade Element Momentum Theory

The Blade Element Momentum (BEM) theory is commonly used in the early design phase of wind turbine rotors and for load analyses. It owes to Glauert [112], who collected all available work on aerodynamics at that time in a single textbook, that the method exists and is helpful for the wind turbine community [113]. The method combines the momentum theory and the Blade Element Theory (BET), which was intended to be used in propeller aerodynamics. The axial and tangential inductions are the unknowns from the momentum theory and the resulting equations are of little use in isolation [114]. The BET models the rotor blade as a single line consisting of discrete span-wise (along the blade radius) elements. The induction effects take into account the radial variations of the airfoil database. Despite that, no 3D Coriolis and centrifugal effects are modelled and, consequently, the loads on the blades can then be assumed to rely purely on the lift and drag characteristics of these airfoil shapes [114, 115].

Because of the two-dimensional assumption for the blade element properties, as expected, the model fails if a strong three-dimensionality of the flow takes place. This is particularly true near the blade root and tip regions where a radial flow interaction is likely to occur. Approaching the tip, the fluid flow is rolled up due to a significant change of the radial circulation distribution, which in turn produces an intense tip vortex similar to those on airplane wings. This vortex is transported downstream and the whole wake swirls in opposite direction than the rotor rotation. A significant loss of the local force occurs and the pure BEM method will not capture it at all. Corrections of this issue have been given by Prandtl [116], Glauert [112] and recently by Shen *et al.* [117]. It shall be noted that trailing vortices are produced along the whole span of the blade, but the most remarkable vortices are usually located near the tip and in the blade root area due to a strong gradient of the radial circulation distribution.

Similar to the outer blade region, in the inboard region a strong radial flow interaction also takes place. In fact, this topic is the main focus of the present studies. As mentioned in the introduction, the inboard blade area generally consists of thick airfoils and operates at high angle of incidence, and is associated with massive flow separation. It is worthwhile to mention again that the centrifugal force radially transports the detached fluid flow to the outer blade region and the Coriolis force acts in chordwise direction, increasing the chordwise flow acceleration. As a result, the lift coefficient remarkably increases compared to the corresponding 2D conditions within this area that is commonly referred as the Himmelskamp effects [3]. The 2D assumption of the BEM method obviously cannot account for these effects and several correction methods have been developed for this purpose, for example, by Snel [27], Du and Selig [31], Chaviaropoulos and Hansen [29] and Bak *et al.* [70] . The correction models rely on the ratio of the local chord length to the local radius (c/r). The basic idea of these models is to correct the 2D aerodynamic polars so that they can be more or less mimic the 3D rotating blade characteristics and then provide

them as the input data for the BEM simulations.

2.2 Studied Turbines

2.2.1 Blades with Elliptical and with NACA Airfoil Cross-Sections

In these studies, generic blades constructed by a constant shape for the whole radii without twist are considered in the investigation of the root cause for the Himmelskamp effects [3]. The blade chord is constant along the radius, except near the tip (where taper is introduced starting from 90% of the blade radius). The blade radius (R) is equal to 30 chord lengths (c), with $c = 1$ m. Two different airfoil families, namely elliptical cross sections and NACA 4 digit profiles, with two different maximum thicknesses each are examined to assess the effects of the airfoil contour shape. The profiles and their thicknesses are shown in Table 2.1. For clarity, the elliptical and NACA 4 digit profiles are mentioned as Ellips 00xx and NACA 00xx, respectively, with the last two digits xx specify the percentage of the relative thickness. No camber is introduced in this study. These very simple geometries are chosen to simplify the studies and to isolate the 3D effects from complicated effects arising from the radial interaction of the flow induction, all the more, as a complete picture of the mechanism for the viscous and inviscid rotational effects are of interest.

2.2.2 The MEXICO Rotor

The MEXICO (Model Experiments in Controlled Conditions) rotor is a 2.25 m radius three-bladed rotor studied in the MEXNEXT project. Three different aerodynamic profiles (DU91-W2-250, RISØ-A1-21 and NACA 64-418) are used in the blade design. The DU91-W2-250 airfoil is applied from 20% to 45.6% span, the RISØ-A1-21 airfoil from 54.4% to 65.6% span and the NACA 64-418 airfoil outboard of 74.4% span. Hence a constant airfoil is applied over a considerable radial extension around the instrumented sections in order to assure known conditions at each of these sections, where as the remaining length is used for the transition from one airfoil to another [118]. The distributions of the chord length and twist angle along the blade radius is given in Figure 2.2. The main objective of the project was to advance aerodynamic (and acoustic) modelling of wind turbines and wind turbine farms [119]. The *new MEXICO* experiments used in the validation were carried out within the ESWIRP

Table 2.1: Shapes used for the blade with the elliptical and NACA airfoil cross-sections.

Shape	Relative thickness [%]
Ellips 00xx	10
	20
NACA 00xx	10
	20

and INNWIND projects in the large low-speed facility of the German Dutch Wind Tunnels (DNW). [77, 78].

2.2.3 The AVATAR Rotor

The generic 10 MW AVATAR blade [120, 121] was chosen in the examination. The blade is twisted and tapered. The list of airfoils used in the blade can be seen in Table 2.2. It is designed based on the DTU 10 MW wind turbine [122] with the aim to model the aerodynamics of turbines larger than 10 MW. It shall be kept in mind that the rated wind speed of the AVATAR rotor is smaller than the DTU 10 MW rotor. As the rated power is kept constant, the approach results in a larger blade radius [120]. The original DTU 10 MW blade is scaled by the factor 1.15 in radial direction to a radius of $R = 102.9$ m. The axial induction a is reduced to below $1/3$, resulting in $0.23 < a < 0.28$, which is better from a cost of energy point of view [123]. This design concept is denoted as low induction rotor or LIR concept. A comparison of the chord

(a) c/r **(b)** β
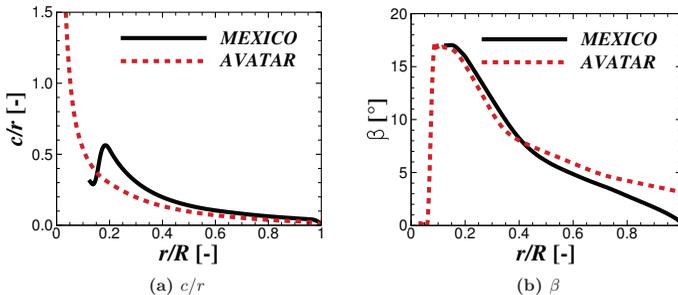
Figure 2.2: The distributions of the local chord to radius (c/r) and twist angle (β) along the radius for the MEXICO and the AVATAR rotor. It shall be noted that the most inboard region of the AVATAR rotor consists of cylindrical shape with the chord length of about 5 m, and c/r is larger than unity for $r/R < 0.05$.

Table 2.2: Airfoil sections used for the AVATAR reference blade [67, 120].

Airfoil Thickness [t/c]	Airfoil Type
60.0%	Artificial, based on thickest available DU
40.1%	DU 00-W2-401
35.0%	DU 00-W2-350
30.0%	DU 97-W300
24.0%	DU 91-W2-250 (modified for $t/c = 24\%$)
21.0%	Based on DU 00-W212, added trailing edge thickness
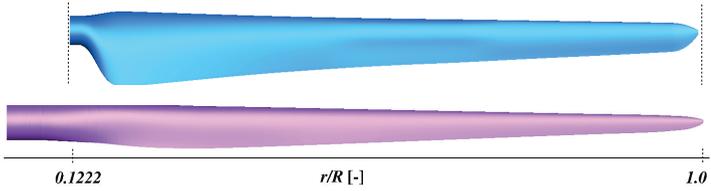
Figure 2.3: The MEXICO (top) and the AVATAR rotor blades.
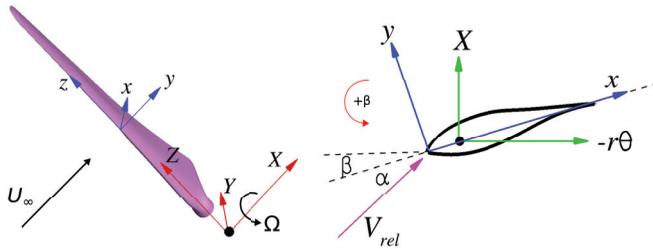
Figure 2.4: Global and local coordinate systems of reference used in the present studies. Note that nose down generates a positive β value.
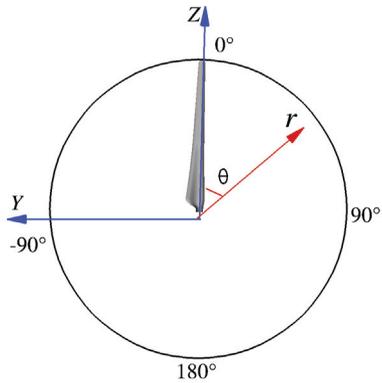
Figure 2.5: Definition of the azimuth angle for the rotor simulation.

19

and twist distributions with the MEXICO rotor is illustrated in Figure 2.2. It can be seen that the c/r parameter of the MEXICO rotor is larger than of the AVATAR rotor starting from r/R of 0.15, while no much difference of the twist angle distribution is present in the blade inboard region. The shape of the blades are presented in Figure 2.3.

The Cartesian axes in inertial (X,Y,Z) and rotating (x,y,z) frames of reference are adopted in these studies. Details of the coordinate system are illustrated in Figure 2.4. In the rotating (local) coordinate system, x,y and z represent chordwise, normal and spanwise directions of the blade, respectively. They are attached on the blade and rotate alongside with the rotor. Similar approaches have been employed also in [9–11, 67]. In addition to these Cartesian coordinates, the rotation of the blade is represented by the radius (r) and azimuthal angle (θ) depicted in Figure 2.5. The blade rotates in clockwise direction, and zero azimuth angle is defined as the blade tip points upward.

2.3 Mesh Generation

The computational grids used in the present studies were generated using the commercial software Gridgen from Pointwise Incorporated. The mesh, especially for the blade, is constructed by an automatic script developed at the institute [84]. By doing so, the user can specify the required resolution of the generated meshes easily, which greatly accelerates the process chain of the studies. There are options to chose two different grid topologies (O and C-H meshes) and to use advanced-block tip and wake meshes. The distribution of the radial grid points can be specified by the user either using hyperbolic tangent function or by a customized distribution as an input file. Recently, the script was extended to allow chordwise grid points redistribution near the blade root region where the shape is usually cylindrical. The resulting volume grid is then converted to a structured *cgns*-format which will be converted to the FLOWer grid input using the in-house code cgns2FLOWer. Detailed descriptions of the grid resolutions, number of cells within the boundary layer, the first cell layer distance, background mesh and other important parameters will be given in Chapter 3 for the blades with elliptical and with NACA airfoil cross-sections, Chapter 4 for the MEXICO rotor and Chapter 5 for the AVATAR rotor.

2.4 Extraction of the Angle of Attack

To compare the 3D and 2D aerodynamic characteristics, the flow condition in both cases must be consistent. Thereby, the effective angle of attack is a key parameter that needs to be considered, which is influenced by the effects of bound circulation and wake, including the shed- and trailing-vortices and inductions. Thus, it cannot be obtained directly from the blade surface pressure data [67].

Several methods have been proposed in the extraction of the effective angles of attack for rotating blades. The calculations of α performed by Snel *et al.* [27], Bruining

| (a) | (b) |
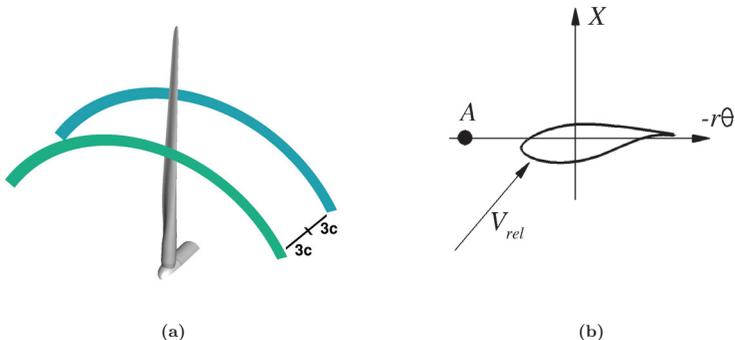
Figure 2.6: Illustration of the blade angle of attack extraction methods according to (a) Hansen [126] and (b) Shen [125]. Left figure shows thin annular planes upstream and downstream of the rotor where the flow is monitored, a lot of grid points are necessary for this method. Right figure illustrates a monitor point (point A) where the flow data is stored during simulations.

et al. [23], Laino *et al.* [124] and Bak *et al.* [70] correspond to the inverse blade-element momentum (BEM) method in which a measured or computed load distribution is used as the input data [125]. Reasonable results were obtained for the case where the three-dimensionality of the flow is small. Furthermore, the method depends strongly on the tip-loss correction model used for the BEM code; different tip loss correction models result in different airfoil polars [125].

The reduced axial velocity technique (RAV), also known as the azimuthal averaging technique, was employed by Hansen *et al.* [126], Johansen and Sørensen [60] and Hansen and Johansen [127]. In this approach, the velocity is monitored during simulations at two axial positions, one upstream and one downstream of the rotor (see Figure 2.6a) at a specified distance to the rotor plane. The actual inflow velocity is determined by considering the decrease of the axial velocity due to the presence of the rotor. It is calculated by averaging the velocity for a specific azimuth range at a given radial position in each extraction plane. In the present studies, the averaging was applied from $-60° < \theta < 60°$. Then, linear interpolation is used to calculate the velocity in the rotor plane. The method has been coded [128, 129] at the institute and was tested in [56, 67, 128, 129]. The approach was used by other preceding authors [60, 126, 127] to derive the 3D characteristics of rotating wind turbine rotors with reasonable results. Furthermore, Shen *et al.* [125, 130] confirmed this by comparing the method with the iterative bound circulation analysis using the Biot-Savart law they proposed. The method developed by Shen *et al.* [125, 130] will be described in the following paragraph.

2. RESEARCH METHODOLOGY

However, the RAV method requires many input points to evaluate the local flow features since the method utilizes azimuthally averaged data. As the velocity is averaged over a large azimuth range, the reliability of the approach is expected to deteriorate for the rotor operating under a strong unsteady inflow condition.

Shen *et al.* [125, 130] proposed two methods for determining α by employing the Biot-Savart integral to calculate the influence of the bound vorticity on the velocity field. Both methods require monitor points in the vicinity of the blade containing the velocity data, which can be obtained from measurements or CFD results. The difference of the second technique to the first method is on the determination of the bound circulation. In the first approach, the monitor points are distributed along the blade sections where the local force on the blade is known. The bound circulation of the blade section is represented by a distinct vortex in the quarter chord location of the blade section. The initial circulation is obtained based on the velocity components recorded on the monitor points. Then, the circulation is used to calculate the induced velocities which can be employed to correct the initial velocities on the monitor point. The step is carried out iteratively until convergence is achieved. In the present studies, this method is called the "SHS" approach.

In the second technique, the bound circulation is calculated using the chordwise pressure distribution of the airfoil, enabling the velocity monitor points to be located closer to the blade, which results in a higher accuracy. A similar method was proposed by Schmitz and Chattot [131] using the Biot-Savart law as a base. However, in this method, the bound circulation is calculated on a closed contour line covering the blade section. In determining the angle of attack for measured data, Sant *et al.* [132] employed the Kutta-Joukowski law to estimate the bound circulation on the blade. Then, it was used to re-construct the wind turbine wake using a free wake vortex model. The angle of attack is then calculated using the lifting line theorem if the calculations are converged.

In the present studies, most of the works were based on the RAV approach to determine the local effective angle of attack on rotating blades. It shall be noted that the method can only be used for steady inflow situations because any strong unsteadiness (like inflow turbulence) will be disregarded in the azimuthally-averaging procedure. Furthermore, as massive flow separation occurs in the inboard area, it is expected that there will be uncertainty about the accuracy of the approach. To consider this issue, the consistency of the method will be evaluated and discussed further in Section 5.3.

Chapter 3

3D Effects on the Inviscid and the Viscous Flow

Currently, there are open questions related to a complete mechanism of the 3D effects. The issue mainly stems from the lively debate whether the phenomena are caused by inviscid or viscous effects. In the present chapter, this aspect is investigated for generic rotors. The main aim is to quantify the inviscid and viscous contributions on the 3D effects. To do so, the chapter is divided into three main parts. (1) Section 3.1 will discuss the main contribution of the inviscid effect of the blade without circulation by avoiding complex interaction of the trailing vortices. (2) Then, the effect of circulation will be addressed in Section 3.2. In Section 3.3, the viscous effect will be quantified and recommendation for the blade design will be given afterwards.

3.1 Inviscid Non-circulatory Flows

3.1.1 Test Case and Computational Setup

The effect of rotation in the frame of inviscid flow is investigated in this study. For this purpose, steady Euler calculations are conducted for rotating blades. As described shortly in Section 2.2.1, the blade was constructed by extruding an aerodynamic profile in radial direction. The rotor consists of two blades depicted in Figure 3.1. A similar technique was also used by Kroll [133]. The blade chord length is constant of 1 m, except near the tip (where taper is introduced starting from 90% of the blade radius) to prevent the occurrence of a non-physical discontinuity in the CFD results due to a strong numerical dissipation at the blunt tip region with the use of the Euler solver [134]. The radius of the blade (R) is equal to 30 chord lengths (c), equivalent to 30 m. The elliptical and NACA airfoil cross sections are selected for the blade shape.

Using the Chimera technique in the overlapping region, the domain consist of two different meshes, namely Blade and Background meshes. The Blade mesh has 256x128x88 cells in chordwise, wall normal and radial directions, respectively. It was observed that the employed grid resolutions are spatially converged to model the
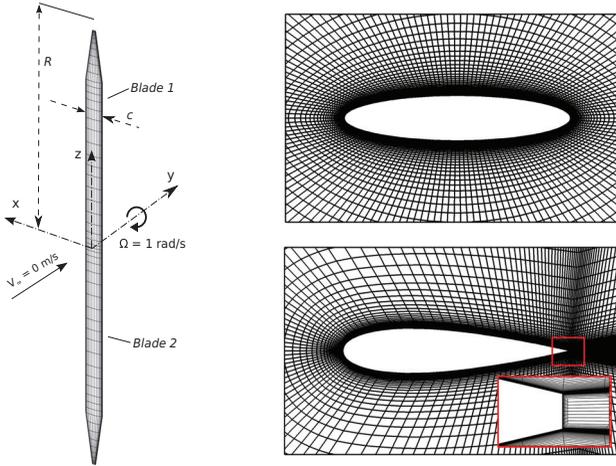
Figure 3.1: Meshes used in the calculations (scale and cells number are adjusted in the pictures to avoid graphical interferences).
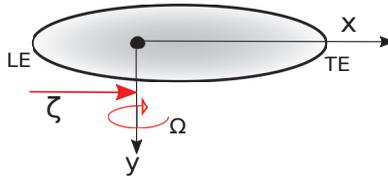
Figure 3.2: Center of rotation variation.

mean flow characteristics, especially if no unsteady simulations are performed. Furthermore, the cells number was adopted from the grid study carried out by Meister in his thesis [135]. In radial direction, the inner blade region has higher mesh density than the outer blade area. The mesh was refined near the leading and trailing edges. As the viscous effects will be introduced in Section 3.3, the mesh was refined near the wall employing 32 cells to properly resolve the boundary layer. The non-dimensional wall distance (y^+) of the first cell layer is less than unity. The O-type mesh topology was applied for the elliptical blades, while a C-type mesh was generated for the NACA type blades. Figure 3.1 presents the mesh of the blade section for the elliptical and the NACA type blades. The Euler wall boundary condition was used on the blade surfaces, while the farfield boundary condition was employed at the outer boundaries of the background mesh. The background mesh has

a cylindrical shape and is refined in the rotor area. The dimension is set to minimum 6 times blade radius from the blade center of rotation.

The coordinate system used in the present study is defined in Section 2.4. For clarity, the coordinate definition is presented again in this section including necessary information in Figure 3.1. The blade is rotating at a constant rotational speed Ω = 1 rad/s and the freestream velocity (U_∞) was set to zero. No twist and pitch angles are introduced, allowing the blade to operate at zero angle of attack (α) for the whole spanwise positions. The relative distance between the leading edge (LE) and the center of rotation (in chordwise direction, non-dimensionalized by the chord length) is defined as ζ, see Figure 3.2. In this study, different chordwise positions of the center of rotation were examined, namely ζ equal to 0.00, 0.25, 0.50, 0.75, and 1.00, to examine its importance on the inviscid rotational effect. By varying ζ, blade 1 ($r > 0$) sees opposite inflow direction to blade 2 ($z < 0$), *i.e.*, $\zeta = 0.00$ in blade 1 is equal to $\zeta = 1.00$ in blade 2. Due to this anti-symmetrical behavior, only blade 1 was evaluated.

The inviscid solutions were obtained by employing the finite volume formulations on block structured meshes using the CFD code FLOWer [75]. Implementations of the Euler equations in FLOWer and some examples of its applications were given in [74, 75, 133, 136–138]. For the spatial discretization, a cell-centered scheme was used as it provides high robustness and is well-suited for parallel applications. The scheme is second order accurate in space on smooth meshes. For the steady state case, the integration is accelerated by means of the local time stepping technique, employing the explicit hybrid 5-stage Runge-Kutta with central discretization scheme [74]. The CFL number for the main equations is equal to 3 in the present calculations. To accelerate convergence, multigrid level 3 was utilized. In each stage of the Runge-Kutta time-stepping scheme, data are exchanged between the computational blocks as this strategy provides good convergence acceleration and is able to damp the oscillation in the residual history (further details were explained by Rossow [138]). The implicit residual smoothing with variable coefficients according to Radespiel *et al.* [139] was applied. For inviscid flow calculations, it is often beneficial to damp the numerical
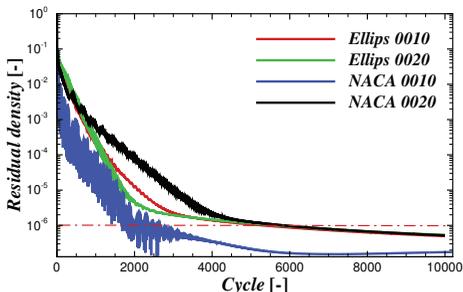
Figure 3.3: Convergence history of residual density.

enthalpy to obtain faster convergence as shown in [133]. However, the effect of this damping is negligible in the present calculations and it is dominant only for high speed flow cases. Therefore, the enthalpy damping was switched off. In Figure 3.3, the convergence history of the density residual is shown. The residuals for all cases drop to below 10e-6. The iteration was stopped after 10k cycles, providing a good converged result with a very small fluctuation of the density residual. This shows that the steady assumption is plausible.

The discussion presented in the present studies mainly involves the streamline curvature of the flow past a rotating blade which can be divided into two aspects. The first aspect discusses the influence of the flow curvature in the x-z (rotor) plane that is generated by the blade rotation. The second aspect is dealing with the usual airfoil aerodynamics concerning the flow curvature in the x-y (airfoil) plane due to the shape of the airfoil. To see the coordinate system, please refer to Figure 3.1.

3.1.2   Blades with Elliptical Cross-Section

To demonstrate the influence of 3D rotational effects, steady Euler simulations were carried out on the blades with elliptical cross-section as introduced in Section 2.2.1. The results of the simulations at different radial positions (c/r) and various ζ (0.0, 0.25, 0.50, 0.75, and 1.00) are given in Figures 3.4 and 3.5 for Ellips 0010 and Ellips 0020, respectively. 2D inviscid calculations using the panel code XFOIL and 2D Euler CFD simulations are presented for comparison. The pressure coefficient (C_p) was calculated based on the kinematic inflow velocity of the blade sections $V_{kin} = (U_\infty^2 + (\Omega r)^2)^{0.5}$. With U_∞ equal to zero, V_{kin} depends only on the rotational speed and blade radius.

Figures 3.4a and 3.5a show the C_p distributions of the blades with elliptical cross-section at chord to radius ratio of 0.1, corresponding to a radial position of 10 m. For this position, the 3D results resemble the C_p characteristics of the 2D conditions independent of ζ. The rotation has very little influence at this radial position. This confirms the results of Wood [36, 43, 140] and Dumitrescu [32–34, 41, 42] though their conclusions regarding the viscous effects contradicted each other. At the outer blade part, the effect of rotation on the inviscid flow is small so that the flow behaviour will be similar to the 2D case as shown by the present results. The curvature of the inflow in the x-z plane is small relative to the blade chord length, and it is almost translatory (Figures 3.6a and 3.6c). With decreasing radius (increasing c/r), the flow becomes more curved (Figures 3.6b and 3.6c) and the effect of rotation starts to appear. This is demonstrated by the C_p distributions in Figures 3.4b and 3.5b at $c/r = 0.5$ which differ slightly from the corresponding 2D results. The rotational effect has stronger influence near the leading and trailing edge areas (near the stagnation regions), mostly on the strong accelerating and decelerating flow zones. This characteristic continuously becomes more pronounced with increasing c/r, Figures 3.4c, 3.4d, 3.5c and 3.5d.

The centrifugal and the Coriolis forces are identified as the origins of this phenomenon. These forces act when the flow is locally disturbed by the presence of the blade where the local flow acceleration is present. The forces become zero far away from the blade. They are driven by the pressure gradient effect. Depending on

(a) c/r=0.1.

(b) c/r=0.5.

(c) c/r=1.0.

(d) c/r=2.0.
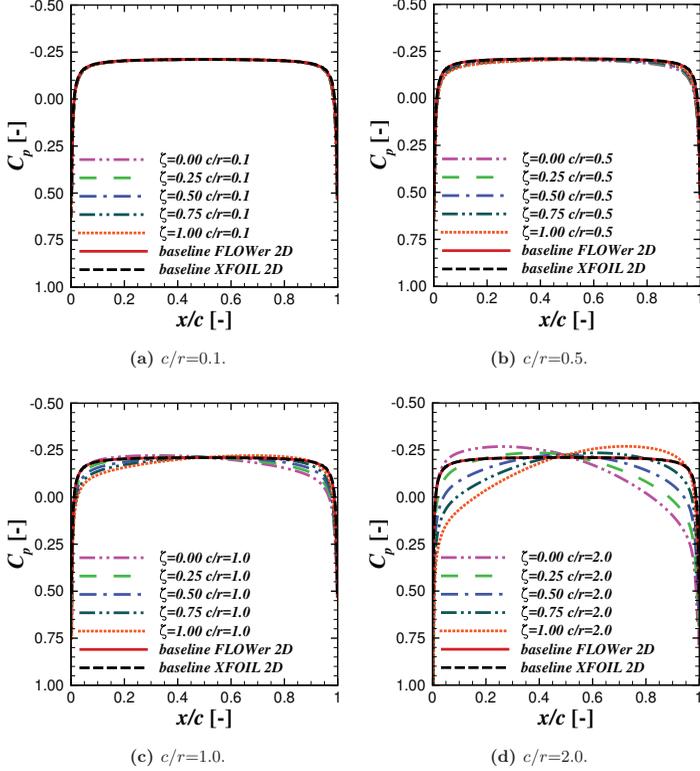
Figure 3.4: C_p distributions of a blade with elliptical cross-section (10% relative thickness) at different radial positions (c/r) and various ζ.

the source, the centrifugal force can be divided into two categories: (1) due to the blade rotation (x-z plane) and (2) due to the airfoil shape (x-y plane). The first category of the centrifugal force is illustrated in Figure 3.7a. It can be seen that the force has two components, chordwise and radial. The magnitude of chordwise component depends on x/c and ζ. This is caused by the variation of the velocity magnitude along the chord line which creates variations in the chordwise centrifugal force (F_{cs}). At the position where $x/c = \zeta$, F_{cs} is equal to zero. Its magnitude increases with x ($F_{cs} \propto \Omega x$) as illustrated in the F_{cs} magnitude distribution in Figure 3.7b. On the other hand, the radial component of the centrifugal force has no

(a) c/r=0.1.

(b) c/r=0.5.

(c) c/r=1.0.

(d) c/r=2.0.
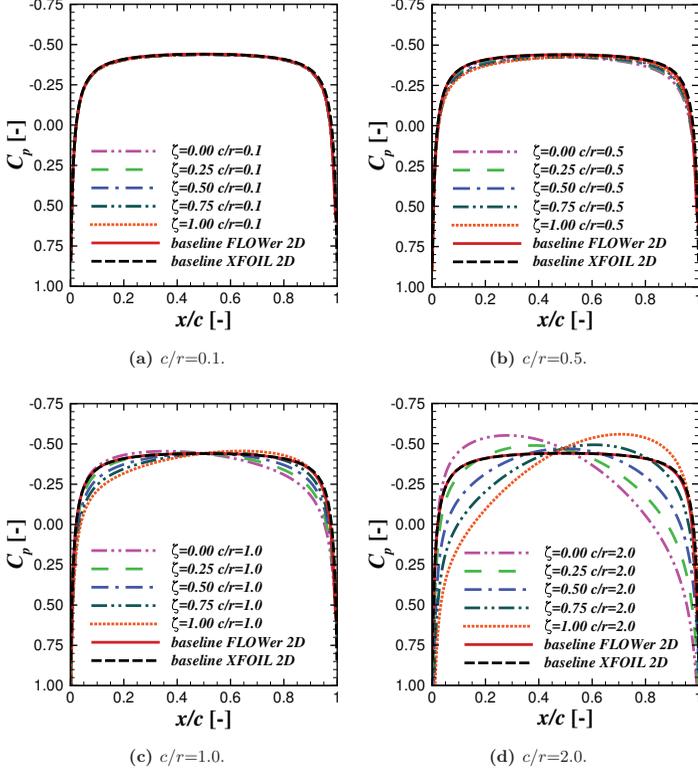
Figure 3.5: C_p distributions of a blade with elliptical cross-section (20% relative thickness) at different radial positions (c/r) and various ζ.

dependency towards x/c and ζ, instead it is strongly dependent on the radial position of the blade section. A comprehensible visualization of the blade section, where F_{cs} is strong, is given in the streamline near the center of rotation in Figure 3.6c. The second category of the centrifugal force is dealing with the force acting in wall normal direction of the airfoil F_n which is manifested in the pressure gradient term. This force is strongly depending on the airfoil shape and usually neglected in first order boundary layer theory [9, 31, 32]. The Coriolis force also has two components; one in chordwise (F_{crs}) and one in radial (F_{crr}) directions. F_{crs} occurs as the response of the flow due to the local spanwise flow component. The combined effects of F_{cs}, F_n and
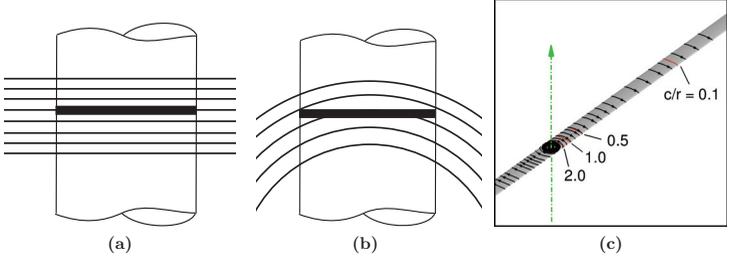
Figure 3.6: Illustration of the flow curvature. (3.6a) Translatory flow, (3.6b) curvilinear flow, and (3.6c) streamlines on the blade surface.
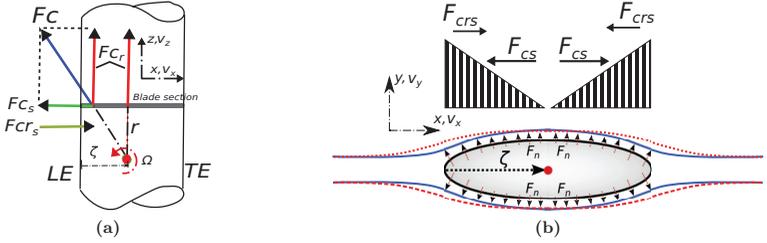
Figure 3.7: Vector force representation on the blade section. (a) The centrifugal and Coriolis forces, (b) illustration of the flow past an elliptical body (solid blue line represents the streamline of translatory flow and dashed red line represents the curvilinear flow streamline.

F_{crs} are pushing the main flow and lead to an increase of the v_y/v_x ratio, see Figure 3.7b. The streamtube is widened, and this creates larger C_p values compared to the two-dimensional (translatory flow) case as displayed in Figures Figures 3.4 and 3.5.

The rotation has a stronger influence for the Ellips 0020 than for the Ellips 0010 cross-section. It is clearly shown in Figures 3.4 and 3.5 that the blade with elliptical shape of 20% thickness has a more pronounced pressure coefficient change, *i.e.*, C_p deviations from the baseline C_p are much larger than for the 10% profile. As explained above, F_{cs} and F_n acting in chordwise and in stream normal directions, respectively, influence the streamtube characteristics. For thicker cross-section, the curvature of the flow becomes stronger (as the profile is highly curved). This imposes stronger F_n outwards the body. As a result, a larger wall normal pressure gradient arises, creating a larger C_p change in Figure 3.5. In addition to that, it was observed that the relative x-velocity component for the Ellips 0020 cross section is smaller than for the Ellips 0010 except in the vicinity of the maximum thickness. This also indicates that the

inertial force has the smallest influence near the maximum thickness, independent of the relative thickness value.

The characteristic of the 3D flow acceleration differs from the 2D acceleration. The difference is identified as the contribution of the inertial forces which are generated by the centrifugal and the Coriolis effects. Consider the chordwise convective acceleration equations for the disturbed flow components as follows:

$$\breve{a}_x = \breve{v}_x \frac{\partial \breve{v}_x}{\partial x} + \breve{v}_y \frac{\partial \breve{v}_x}{\partial y} + \breve{v}_z \frac{\partial \breve{v}_x}{\partial z}, \tag{3.1}$$

where

$$\breve{a}_x 1 = \breve{v}_x \frac{\partial \breve{v}_x}{\partial x}, \quad \breve{a}_x 2 = \breve{v}_y \frac{\partial \breve{v}_x}{\partial y}, \quad \breve{a}_x 3 = \breve{v}_z \frac{\partial \breve{v}_x}{\partial z}, \tag{3.2}$$

$$v_x = \breve{v}_x + \Omega z, \quad v_y = \breve{v}_y, \quad v_z = \breve{v}_x z - \Omega x. \tag{3.3}$$

In Equation 3.1, the rotation term from the rotor rotation is omitted to isolate the acceleration effects caused by the presence of the blade. It is shown that $\breve{a}_x$ is composed by three main contributors; chordwise ($\breve{a}_x 1$), normal ($\breve{a}_x 2$) and crosswise ($\breve{a}_x 3$) directions. The third contributor indicates how the chordwise acceleration is influenced by the spanwise flow component which becomes the main difference compared to the acceleration equation in 2D.

In Figure 3.8, the chordwise convective flow acceleration for the disturbed flow components is presented. The magnitude is non-dimensionalized by V^2/c, where V is the total velocity of a fluid particle at the corresponding position ($V = (v_x^2 + v_y^2 + v_z^2)^{0.5}$). Theoretically the flow disturbance is zero far away from the solid body. This is confirmed as $\breve{a}_x 1$ and $\breve{a}_x 2$ become zero further away from the blade. A similar behaviour is observed for $\breve{a}_x 3$ but is not presented in Figure 3.8. Note that if the rotation term is included in computing a_x, the convective acceleration far away from the rotor is not zero but is equal to $-\Omega^2 x$ (even if $\breve{v}_x = \breve{v}_y = \breve{v}_z = 0$). This term represents the centripetal acceleration that occurs only when the equation is transformed into the rotating frame of reference. The flow starts to decelerate at about one chord length upstream of the leading edge. Then it is strongly accelerated near the leading edge location, reaching its maximum around 5% chord length. Downstream this location, the acceleration of the fluid particle is decreasing and reaches zero around the maximum thickness (x/c = 0.5). Then, it is entering the adverse pressure zone at a larger x/c value. For ζ = 0.5, the general behavior of the fluid particle acceleration for all c/r values is similar, but the magnitude of acceleration differs. It can be seen that the acceleration and deceleration values for the higher c/r case are remarkably smaller than for the lower c/r and 2D cases.

In the 3D case the magnitude of convective flow acceleration ($\breve{a}_x 1 + \breve{a}_x 2$) varies depending on ζ. In Figures 3.8a and 3.8b, a strong variation is observed at $0.5 < x/c < 1.0$ while the variations are much smaller upstream of this location. For the case where the center of rotation is located at mid-chord position ($\zeta = 0.5$) in Figures 3.8c and 3.8d,

(a) Ellips 0010 $\zeta = 0.0$.

(b) Ellips 0020 $\zeta = 0.0$.

(c) Ellips 0010 $\zeta = 0.5$.

(d) Ellips 0020 $\zeta = 0.5$.

(e) Ellips 0010 $\zeta = 1.0$.
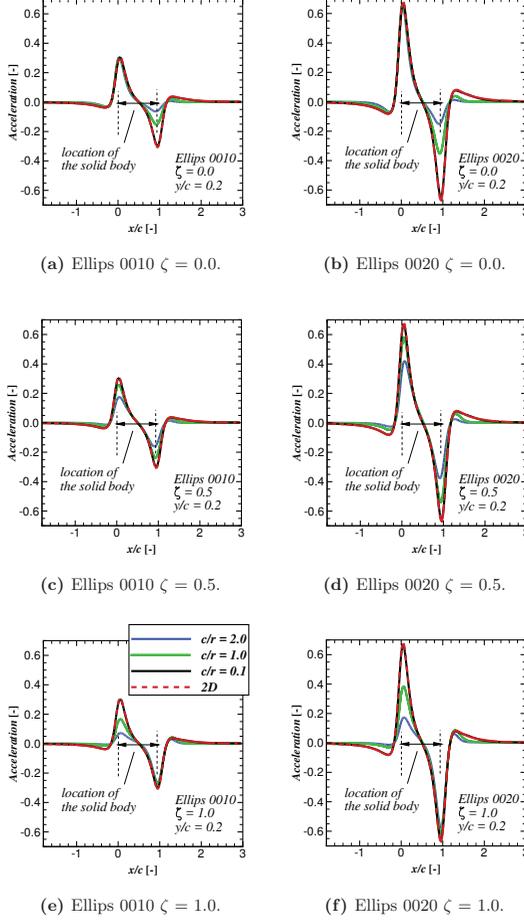
(f) Ellips 0020 $\zeta = 1.0$.

Figure 3.8: Convective flow acceleration in x-direction ($\breve{a}_x1 + \breve{a}_x2$) normalized by V^2/c at $y/c = 0.2$ for the blades with Ellips 0010 and 0020 shapes. Three radial stations and three ζ values are examined.

the impact of c/r is the same upstream and downstream of ζ, but the discrepancies between different c/r values are smaller than in the case for $\zeta = 0.0$. In Figures 3.8e

and 3.8f, the magnitude of acceleration varies strongly near the leading edge. In this case, the center of rotation is located at $x/c = 1.0$ and the variation of acceleration is very small at this position, contrasting the case for $\zeta = 0.0$. Additionally, for all ζ values, the acceleration shows almost no variation at the middle chord position, where the maximum thickness is located, for both studied elliptical shapes. Therefore, it can be seen that the chordwise flow acceleration due to the influence of the streamwise and normal flow components has the smallest variation near the center of rotation and the maximum thickness.

In Figure 3.9, the effects of the spanwise flow component on the chordwise acceleration is presented. It can be seen that $\breve{a}_x 3$ reduces the $\breve{a}_x$ magnitude (becoming more negative) for $\zeta = 0.0$, increasing the deviation to the 2D flow acceleration. This causes a strong influence on the chordwise pressure gradient as shown in Figure 3.5d. The distributions of $\breve{a}_x 3$ are influenced strongly by the chordwise position of the center of rotation as illustrated in Figure 3.9b. It becomes evident that $\breve{a}_x 3$ is not zero near the leading edge for $\zeta = 0.5$ and 1.0 due to the influence of the local spanwise flow. As can be depicted from Figure 3.10, the spanwise flow component is actually still present at the outer blade area around the leading edge although the effects are significantly weaker compared to the inboard region.

To better understand the effects of the inertial forces on the 3D flow, the contributing terms in the Navier-Stokes equations can be evaluated. Consider the momentum equation in x-direction as

$$v_x \frac{\partial v_x}{\partial x} + v_y \frac{\partial v_x}{\partial y} + v_z \frac{\partial v_x}{\partial z} = -\frac{1}{\rho} \frac{\partial p}{\partial x} + \Omega^2 x + 2\Omega v_z. \tag{3.4}$$

(a) $\zeta = 0.0$, $c/r = 2.0$ **(b)** $\breve{a}_x 3$, $c/r = 2.0$
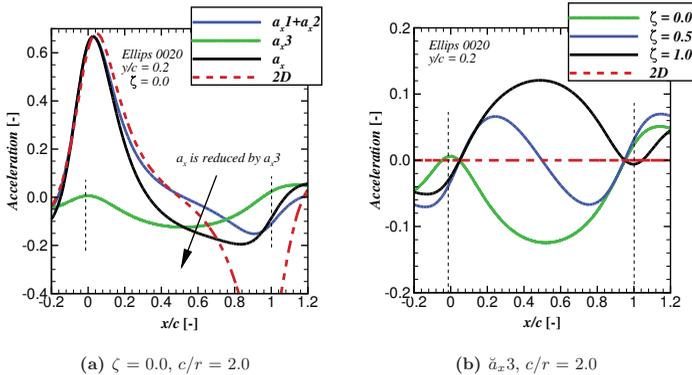
Figure 3.9: Crosswise flow component ($\breve{a}_x 3$) influence on the convective flow acceleration in x-direction normalized by V^2/c at $y/c = 0.2$ for the blade with the Ellips 0020 shape; (a) for $\zeta = 0.0$ and (b) for various ζ values.
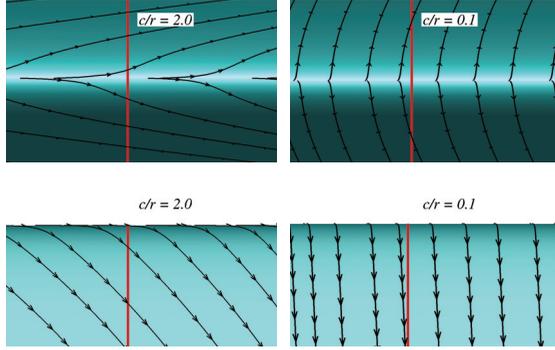
Figure 3.10: Streamlines on the blade surface near the leading edge area for $\zeta = 0.5$ at the inboard (left) and outboard (right) blade sections with the Ellips 0010 shape. The top figures show the front view upstream of the leading edge and the lower figures are the view from positive y-axis. The spanwise flow component is still observed in the near leading edge area at $c/r = 0.1$ although the influence is much weaker compared to radial station of $c/r = 2.0$.
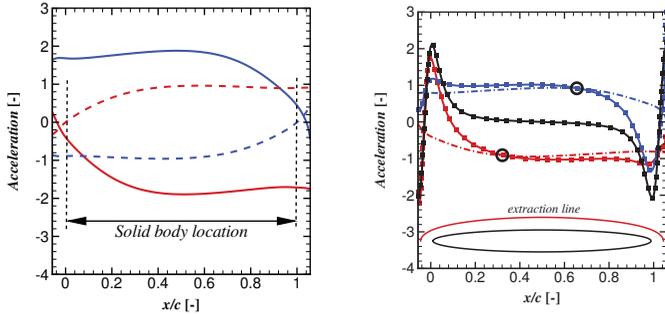
Figure 3.11: Acceleration terms quantification for the momentum equation in x-direction; a_{crs} (solid lines), a_{cs} (dashed lines), a_{is} (dash dotted lines) and a_x (symbolized lines). The blade with Ellips 0010 shape is examined. The data are normalized by V^2/c. Red lines represent $\zeta = 0.0$, blue lines are $\zeta = 1.0$ and black line is 2D data. The regions marked by circles indicate the zero pressure gradient areas.

The left hand side terms represent the convective flow acceleration in x-direction (a_x) as in Equation 3.1 but with the rotation term included. The right hand side terms represent the pressure gradient and inertial forces. The latter can be divided into the

33
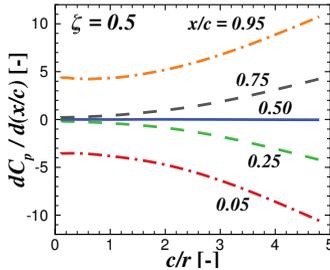
Figure 3.12: Chordwise pressure gradient along the blade with Ellips 0020 cross-section.

centrifugal term ($a_{cs} = \Omega^2 x$) and the Coriolis term ($a_{crs} = 2\Omega v_z$). The contribution of these two terms is represented as the inertial term ($a_{is} = a_{cs} + a_{crs}$). Figure 3.11 presents the distribution of a_{cs}, a_{crs}, a_{is} and a_x normalized by V^2/c for two different ζ values. The effect of the inertial force is actually not exactly zero at $x/c = \zeta$ due to the influence of the chordwise Coriolis force, but is very weak. For $\zeta = 0.0$, the strength of the positive flow acceleration is increased by the centrifugal effect where a_{cs} is always positive but is reduced by the Coriolis effect where a_{crs} acts in negative x. At the position where a_{is} is equal to a_x (marked by circles), the pressure gradient shall be zero to balance the momentum equation. This is confirmed as the minimum pressure level (with zero gradient) in Figure 3.4d occurs around this position.

In the extreme root region, Figures 3.4d and 3.5d, $c/r = 2.0$, the rotation has a very strong impact. While XFOIL and 2D FLOWer predicted very similar C_p distributions, the 3D results differ significantly at this radius. Depending on ζ, the pressure coefficient within the accelerating and decelerating flow regime changes. An increase in ζ tends to increase C_p near the leading edge region. As an example, while the 2D case shows a sharp C_p reduction from the leading edge up to about 10% chord length, the decrement for the $\zeta = 1.00$ case is more gradual until it reaches the minimum pressure coefficient at about $x/c = 0.75$. This clearly indicates the influence of the center of rotation on the chordwise pressure gradient. In addition, it is interesting to note that the magnitude of the chordwise pressure gradient gradually decreases from the root towards the outer blade sections for the case of $\zeta = 0.5$. Figure 3.12 shows this property and its dependency on c/r ratio (increasing with c/r). The behaviour occurs as the response of the flow due to the influence of the inertial force and the convective flow acceleration discussed above.

3.1.3 Blades with the NACA Airfoil Cross-Section

In this section, the results of the simulations on the blades with the symmetrical NACA airfoil shape are presented. The NACA 4 digit airfoils used in the present simulations have no camber and the maximum thickness is located at $x/c = 0.3$. Figures 3.13 and 3.14 show the C_p distributions for NACA 0010 and 0020, respectively, for various c/r

(a) c/r=0.1.

(b) c/r=0.5.

(c) c/r=1.0.

(d) c/r=2.0.
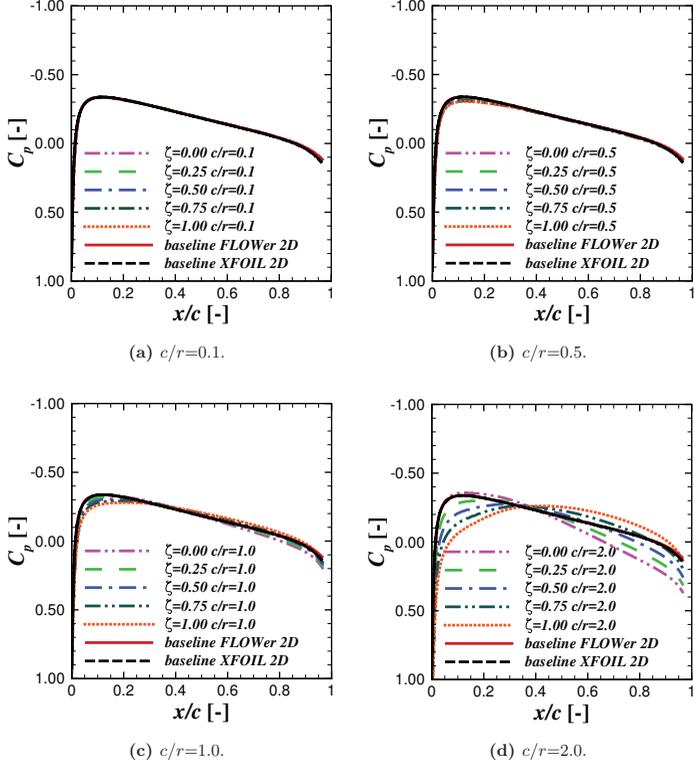
Figure 3.13: C_p distributions of a blade with the NACA 0010 cross-section at different radial positions (c/r) and various ζ.

and ζ values. For clarity of the visualization, the data at $x/c > 0.97$ are excluded because quite large spikes were observed. As mentioned in Section 3.1.1, Liu and Jameson [134] demonstrated that the Euler solver is struggling in predicting the flow around a blunt trailing edge. The scheme is inaccurate to resolve a high gradient inviscid flow over such corners, and the use of an appropriate cusp can reduce this issue. Because the present NACA airfoils have blunt trailing edges with thicknesses around 0.2% (NACA 0010) and 0.4% (NACA 0020) relative to the chord length, the resulting spikes are observed.

As already presented in Section 3.1.2, the rotation influences the characteristics of

(a) c/r=0.1.

(b) c/r=0.5.

(c) c/r=1.0.

(d) c/r=2.0.
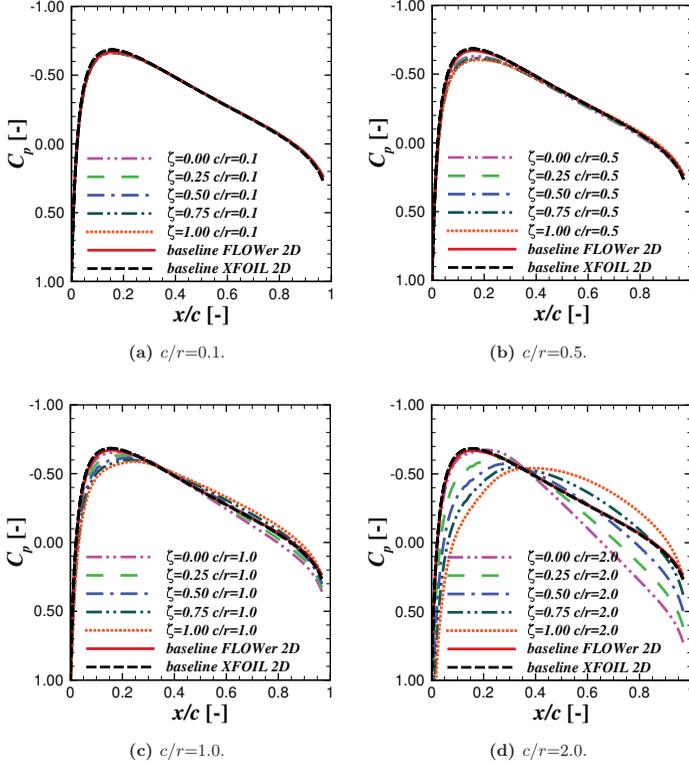
Figure 3.14: C_p distributions of a blade with the NACA 0020 cross-section at different radial positions (c/r) and various ζ.

the C_p distribution of the blade sections. At the outer blade section, the impact is very small as shown in Figures 3.13a and 3.14a. The 3D results resemble the 2D C_p distributions for both airfoils studied. The influence starts to occur from the region near the minimum C_p, and becomes more noticeable with increasing c/r ratio. Depending on ζ, the shape of C_p and the position of its minimum value vary, and, similar to the elliptical shapes, the effect is more pronounced for the thicker cross-section.

In all c/r values, even in the extreme root region (Figures 3.13d and 3.14d), the rotation seems to have a small influence on the C_p distribution along the front side of the airfoil $(0 < x/c < 0.3)$ if the center of rotation is located at the leading edge $(\zeta = 0.0)$.
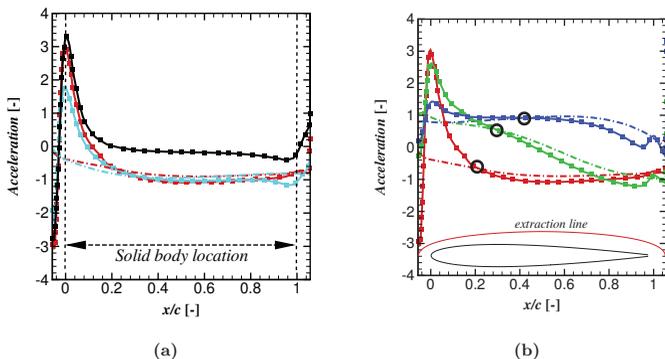
Figure 3.15: Acceleration terms quantification for the momentum equation in x-direction at $c/r = 2.0$; a_{is} (dash dotted lines) and a_x (symbolized lines). The data are normalized by V^2/c. (a) Blade with Ellips 0010 shape (light blue lines), blade with the NACA 0010 airfoil shape (red lines) and 2D NACA 0010 data (black line). (b) Distributions of a_{is} and a_x for various ζ values for the blade with the NACA 0010 airfoil shape; $\zeta = 0.0$ (red lines), $\zeta = 0.5$ (green lines) and $\zeta = 1.0$ (blue lines). The regions marked by circles indicate the zero pressure gradient areas.

This characteristic is different to the elliptical blade which shows a substantial reduction in the pressure coefficient for $\zeta = 0.0$ at $c/r = 2.0$. Here, the non-symmetrical behavior of the aerodynamic shape (between the front and rear sides) can play an important role as the maximum thickness location is shifted to $x/c = 0.3$ for the NACA profiles, rather than at the mid-chord position for the elliptical shapes. In Figure 3.15, the convective and inertial accelerations in x-direction as in Equation (3.4) are quantified. It is shown in Figure 3.15a that the inertial term (a_{is}) for the blade with the NACA 0010 airfoil shape is still comparable to the blade with Ellips 0010 shape, but a_x for the NACA profile is higher near the leading edge than the elliptical blade for $\zeta = 0.0$. Thus, the inertial term (a_{is}) has a minimum role in the front side of the airfoil for $\zeta = 0.0$. From Equation (3.4), the increased convective acceleration for the NACA 0010 shape near the leading edge is balanced by chordwise pressure gradient ($-\partial p/(\rho \partial x)$) as the inertial term remains similar to Ellips 0010. Note that the pressure gradient is partly contributed by F_n that becomes stronger with increasing surface curvature.

Figure 3.15b presents the effect of ζ on the acceleration terms. Similar to the analysis given for the elliptical blade, zero chordwise pressure gradient occurs at the location where a_{is} is equal to a_x. An interesting point is observed where all C_p curves meet (crossing each other) and have a single value, independent of ζ and c/r. This is observed around $x/c = 0.35$ for the NACA airfoils and $x/c = 0.5$ for the elliptical shapes (see Section 3.1.2). The physical meaning which can be drawn is, that this

point is the location along the chord line where the rotation has the minimum influence on the inviscid flow characteristics, confirmed by the smallest C_p deviation from the 2D case. The observed location is close to the maximum thickness position of the corresponding profile. However, it is worthwhile to note that the location is not exactly at the maximum thickness of the NACA airfoils, but is slightly shifted downstream. It is shown in Figure 3.16 that the dynamic pressure of the spanwise disturbed flow $(\breve{v}_z^2/V^2)$ is minimum at this position.

Figure 3.17 shows the C_p gradient for several ζ values in the decelerating flow regime, at $x/c = 0.5$ and 0.75. In this figure, the pressure gradient, *i.e.* a positive (dCp/dx), is presented as a function of radial position divided by the maximum blade radius (r/R) to get a better view on how much the impact of rotation along the blade span is. From this figure, it can be seen that the pressure gradient increases with decreasing ζ. For many practical purposes of rotating machineries, like wind turbines, the center of rotation is located around the quarter chord position, $\zeta = 0.25$. At this position, the adverse pressure gradient is stronger compared to the corresponding 2D case. Therefore, it is expected to be more prone to separation, and a strong radial flow may develop if the effect of viscosity is considered as already mentioned for the case of the elliptical cross-section. Additionally, the rotation has an influence only in the extreme root sections of the both examined chordwise positions. In this case, the C_p gradient varies only up to $r/R = 0.1$. The Coriolis and centrifugal forces which act within the viscous boundary layer are expected to have a stronger influence than the present effect because it can affect the flow up to 35% blade radius on a wind turbine blade operating near the design point, and even above that for a higher wind speed case [56, 57, 67, 141]. However, the importance of the inviscid effect is expected to be more pronounced if the issue concerning the corner flow near the hub region is considered because the pressure gradient is demonstrated to remarkably increase in the decelerating flow region.
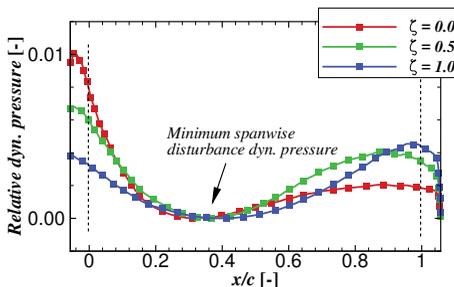
Figure 3.16: Relative dynamic pressure $(\breve{v}_z^2/V^2)$ for the radial flow disturbance. The blade with the NACA 0010 at $c/r = 2.0$ is examined. The same extraction line as in Figure 3.15 is used.

(a) x/c=0.50.

(b) x/c=0.75.
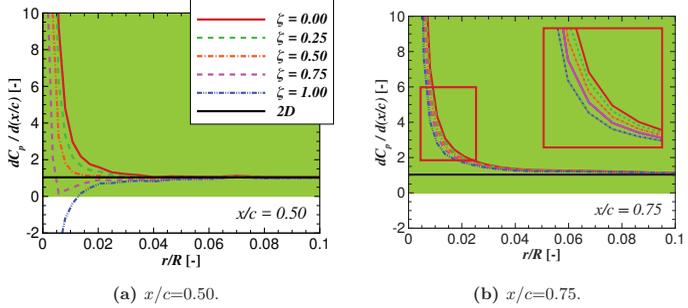
Figure 3.17: Chordwise pressure gradient along the span of the blade with the NACA 0020 cross-section. Green shaded area indicates the positive chordwise pressure gradient.

(a) c/r=0.1.

(b) c/r=2.0.
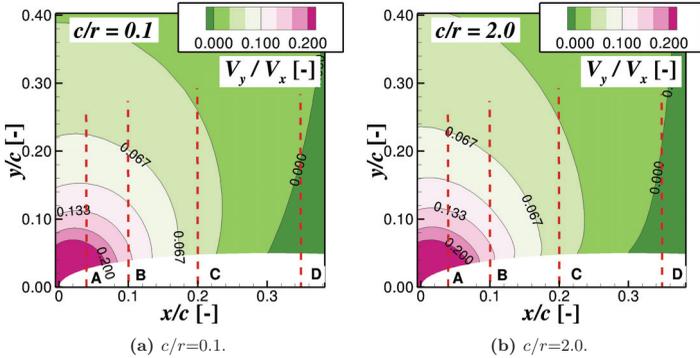
Figure 3.18: Iso contours of flow inclination near the leading edge of the NACA 0010 for ζ=0.0.

Figure 3.18 shows iso-contours of the flow inclination (v_y/v_x) for the NACA 0010 at $c/r = 0.1$ and $c/r = 2.0$. Data are extracted from the slices at the positions marked as A, B, C, and D respectively at $x/c = 0.05$, 0.1, 0.2, and 0.35. The extreme values of ζ equal to 0.0 and 1.0 are chosen and two radial positions are examined ($c/r = 0.1$ and 2.0). The results of the extraction are shown in Figure 3.19. The solid lines in Figures 3.19a and 3.19b correspond to the flow inclination profiles for $\zeta = 0.0$ and the dashed lines represent the case for $\zeta = 1.0$.

In the outer region of the blade, $c/r = 0.1$ (Figure 3.19a), the velocity profiles almost coincide for both ζ values, stating that flow curvature effects in the x-z plane are negligible. Similar results were also observed for the NACA 0020 cross-section
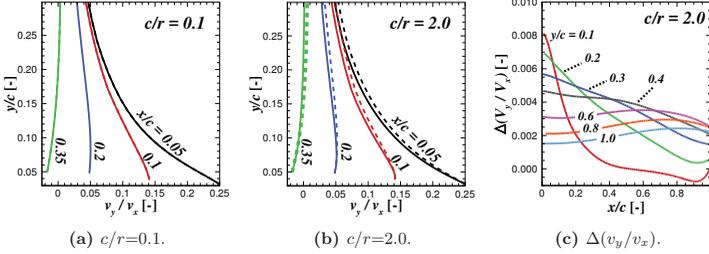
Figure 3.19: Flow inclination profiles. Solid lines in (3.19a) and (3.19b) represent the case for $\zeta = 0.0$, and dashed lines for $\zeta = 1.0$.
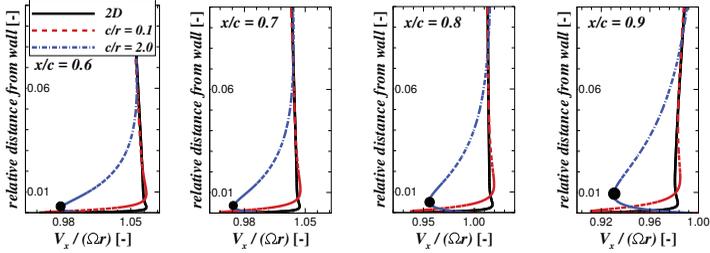
Figure 3.20: Relative velocity profiles and their corresponding iso-contours on the rear side of the NACA 0010 airfoil for $\zeta = 0.25$.

case. Therefore, the C_p distributions are very close to each other (also with the two-dimensional data) as shown in Figures 3.13a and 3.14a. These characteristics also appear in the presence of the viscous boundary layer [24]. It explains that the three-dimensionality of the flow is small. At a larger c/r value, the difference is more pronounced, see Figure 3.19b. It can be seen that the flow inclination between the two ζ values differs. The curvature effect in the x-z plane has a small influence in the

vicinity of the solid surface where a very small difference is observed between the two examined ζ values. The discrepancy between the two cases is increasing farther away from the wall, reaching its maximum, and then they are decreasing in the undisturbed stream. Figure 3.19c shows the plot of their deviation $((v_y/v_x)_{\zeta=1.0} - (v_y/v_x)_{\zeta=0.0})$ in chordwise direction at several positions normal to the chord line. The variations, in general, decrease with x/c except for the slice position far-away from the airfoil wall. Starting from $y/c = 0.6$, the discrepancies are slightly enhanced from the leading edge to 75% of the chord length.

Within the decelerating flow regime, the inviscid curvature effect has a strong impact on the velocity field near the wall. Figure 3.20 illustrates this behavior for the NACA 0010 cross-section with the center of rotation located at $x/c = 0.25$. The relative velocity is extracted at several chordwise positions, and the results are compared to the 2D Euler simulation (Figure 3.20). The single black dot mark in the velocity profiles represents the minimum relative chordwise velocity for the 3D rotating case at $c/r = 2.0$. The relative distance is defined as $(y - y_0)/c$, where y_0 represents the y-coordinate of the airfoil wall.

In the two-dimensional case, the decelerating flow occurs only in the vicinity of the airfoil wall. It shall be noted that the presented velocity is only for the x-component. Thus, the reduction of the velocity near the wall for the 2D case is caused by the missing part of the y-component. At $x/c = 0.6$, the underlying region is located at a wall distance (relative to the chord length) less than 0.0025. Further away from the wall, the velocity remains higher than the free stream (Ωr), see Figure 3.20. The flow becomes slower with increasing chordwise position. It is observed that the value of the relative chordwise velocity reaches less than one at $x/c = 0.9$. While the 3D velocity profiles at a small value of c/r look similar to the 2D case, it can be seen that the flow strongly decelerates in the case with higher a c/r value ($c/r = 2.0$). The reduction is observed for the relative wall distance less than 0.060 and is increasing towards the trailing edge region. The minimum velocity is observed in the vicinity of the wall and its position is shifted farther away from the airfoil body at a higher x/c. For example, the minimum value at $x/c = 0.6$ and $c/r = 2.0$ is located at a wall distance of 0.002 and it is increasing to 0.009 at $x/c = 0.9$. By observing this, it is possible to say that there is a fictitious line of action along the chord where the inviscid effect has its strongest influence (by connecting the dot marks in Figure 3.20). The thickness of the underlying line (distance from the dot point to the airfoil wall) is increasing towards the trailing edge, similar to the boundary layer thickness concept for the viscous flow [5]. Furthermore, the thickness of the underlying line is also decreasing in radial direction, similar to the reduction of the boundary layer thickness in radial direction for a viscous flow over a rotating blade as observed by Rott and Smith [11].

3.2 Inviscid Circulatory Flows

In the discussions presented in Section 3.1, 3D characteristics of the inviscid flow under rotational motion were examined by assuming that the blade does not produce lift, *i.e.,*

non-circulatory flows. However, this specific case alone cannot be directly translated into wind turbine applications because, by nature, the rotor shall produce a positive driving moment. This means that the blade is operating under circulatory flows. In order to extend the current knowledge of the 3D inviscid rotational effects to this particular case, additional simulations for non-zero angle of attack operations were carried out for the blade with the NACA 0010 airfoil shape. Four speed ratios of $\lambda_{c/r=1.0}$ = 2.5, 3.33, 5.00 and 10.00 were examined in these studies, where $\lambda_{c/r=1.0}$ defines the ratio of sectional rotor rotation to incoming wind speed, $(\Omega r)/U_\infty$, at $c/r = 1.0$. It shall be noted that the blade is untwisted and no pitch angle was introduced. Therefore, to obtain reasonable sectional angle of attack, $\lambda_{c/r=1.0}$ was set to the mentioned values. For instance, the geometric angles of attack for $c/r = 1$ and $\lambda_{c/r=1.0} = 2.5$ is equal to 21.8°.

Similar to the examinations for non-circulatory flows, the ratio of c/r and the chordwise distance of the center of rotation (ζ) are the main parameters examined in these investigations. The only difference is that only one blade is modelled in the present studies because the flow is no more periodic from blade 1 to blade 2. It is worthwhile to note that the blade 1 leading edge is at the same location as blade 2. For non-circulatory flows, which do not produce complex 3D trailing vortices, the previous approach is plausible. Despite that, as trailing vortices are generated for the present approach, blade 2 is removed to simplify the studies, avoiding the induction effects from blade 2 to blade 1. This approach is similar to the one carried out by Wood [36] where no hub was modelled. He argued that the actual formation of the hub trailing vortex is likely to be very complicated, and may even involve considerable skewing of the circumferential vorticity in the hub boundary layer as it encounters the blade-hub junction [37]. Thus, it was preferable to keep the model as simple as possible.

The angle of attack was determined by the reduced axial velocity method proposed by Hansen *et al.* [126]. It shall be noted that the complex behaviour of the root vortices may induce some uncertainties in the effective angle of attack calculations which can have an influence to the 3D effects assessment. In comparison with the 2D inviscid results, the pressure coefficient needs to be normalized. In these studies, this was done using the magnitude of stagnation pressure (p_0), defined as the maximum pressure at the corresponding radial station obtained from the computations. The results for ζ = 0.0 are plotted in Figure 3.21. Solid and dashed lines correspond to 3D and 2D pressure coefficient distributions, respectively. Left figures (Figures 3.21a, 3.21d, 3.21g and 3.21j) show the C_p distribution for $c/r = 1.0$, middle figures (Figures 3.21b, 3.21e, 3.21h and 3.21k) for for $c/r = 0.5$ and right figures (Figures 3.21c, 3.21f, 3.21i and 3.21l) for $c/r = 0.2$. The sectional angle of attack increases, and inversely the speed ratio, from top to bottom figures.

It can be observed clearly that the main difference between the pressure distributions of the 3D blade to the 2D airfoil is that the minimum pressure becomes more positive for the blade under rotational motion, *i.e.,* the suction peak at the leading edge is reduced. The effects are stronger with increasing c/r. This causes a
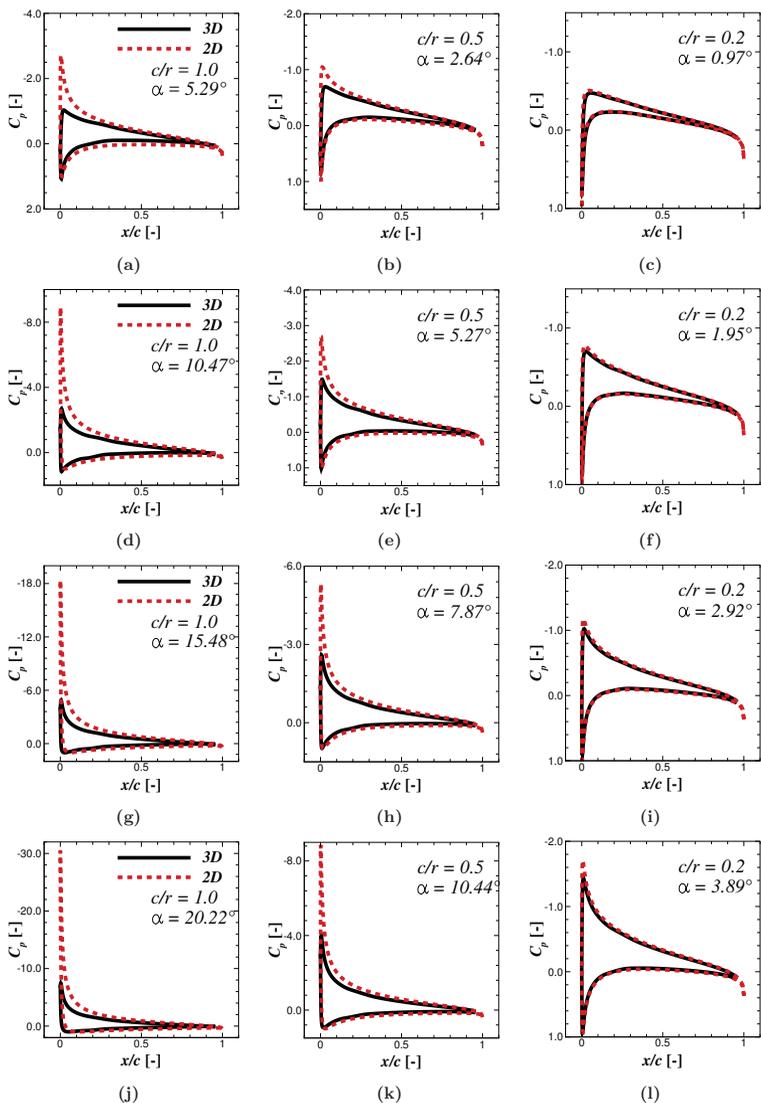
Figure 3.21: 3D (solid line) and 2D (dashed line) inviscid C_p distributions for circulatory flows. From top to bottom: $\lambda_{c/r=1.0} = 10.00$, 5.00, 3.33 and 2.5. From left to right: c/r = 1.0, 0.5 and 0.2. The results presented are for $\zeta = 0.0$. The blade with the NACA 0010 airfoil shape is examined.

43
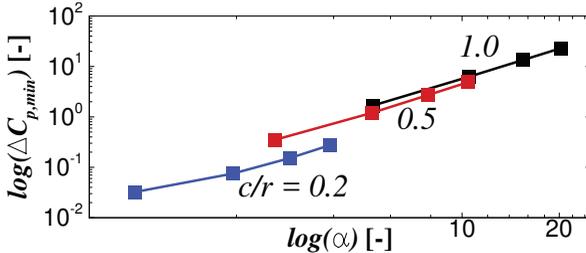
Figure 3.22: $\Delta C_{p,min}$ as functions of α and c/r for $\zeta = 0.0$.

significant reduction of the adverse pressure gradient occurring on the blade suction side. Wood [36] argued that this is the main cause of the 3D effects. The deviation between 2D and 3D conditions becomes more noticeable with increasing angle of attack, as shown from Figures 3.21a, 3.21d, 3.21g and 3.21j. For example, the difference between the minimum 3D C_p to 2D C_p ($\Delta C_{p,min}$) for the case of $c/r = 1.0$ and $\alpha = 5.29$ (Figure 3.21a) is 5.29, and this increases quite significant for the case of $c/r = 1.0$ and $\alpha = 20.22$ (Figure 3.21j) where $\Delta C_{p,min} = 23.00$. This characteristic is also observed for the lower c/r magnitude, but with noticeably reduced influence. Figure 3.22 presents this minimum C_p deviation for the examined cases. It shall be noted that the figure axes are in logarithmic scale for clarity purpose. The deviation reduces for a lower c/r magnitude. Interestingly, $log(\Delta C_{p,min})$ nearly "linearly" increases with increasing $log(\alpha)$. This indicates that a simple correlation model might be able to be derived to relate the inviscid flows on the boundary layer edge to the 2D inviscid flow fields.

These observations for the inviscid effects are in a good agreement with the studies carried out by Wood [36]. He suggested that the 3D behaviour of rotating blades stems from the complex effects of the trailing vorticity, especially in the near hub area. The root vortex can be treated as a potential vortex that generates downwash on the rotor blade. The downwash becomes stronger with reducing r/R (or increasing c/r). Therefore, the local angle of attack reduces and the suction peak becomes more positive. It will be shown in Figure 3.25 that a sharp radial gradient of the bound circulation occurs in the root area of the blade, indicating the occurrence of strong root vortices. A similar result was reported by Wood [36] in his examinations. The effect is actually also present in the tip area as a strong radial gradient of the bound circulation occurs. Therefore, the reduction of the pressure peak for the 3D inviscid case can be categorized as the root effect instead of the rotational effect.

Figure 3.23 presents the pressure coefficient distributions for various ζ values with $\lambda_{c/r=1.0} = 10.0$. It is mentioned again that ζ defines the relative chordwise distance of the center of rotation to the leading edge. Two radial positions are shown, for $c/r = 1.0$ and 0.5. It can be seen that the minimum pressure becomes more positive with increasing ζ. This implies that the deviation between 2D and 3D pressure coefficients

Figure 3.23: Effects of ζ on blade pressure distributions for the blade with the NACA 0010 airfoil cross-section at two different radial positions.

becomes larger and the pressure gradient is smaller. This effect is alleviated significantly at a smaller c/r value. It is caused by the inertial force influence due to rotation as already presented for the blades with elliptical cross-section, and can be categorized as the inviscid rotational effect. As the 3D flow behaviour is affected by the chordwise location of the center of rotation, the current blade design approach can be improved based on this observation. This issue will be discussed further in the following section where the viscous effect is taken into account.

3.3 Viscous-Inviscid Effects on the 3D Rotating Blade

In the previous sections, the 3D inviscid flow response of blades undergoing rotational motion has been discussed in details. Despite that, the discussion is still not yet answered whether the Himmelskamp effect is driven by the inviscid or viscous effects. The surface pressures obtained from any inviscid calculation are, to a better approximation, the pressures acting on the outer edge of the blade boundary layer [36]. As already given in Chapter 1, the studies concerning the inviscid effects carried out by Wood [36] have raised a lively debate at that time especially the one given by Dumitrescu *et al.* [32, 41]. Shortly, Wood [36] concluded that the root sources of the 3D effects are the inviscid flow natures due to rotation. The reduction of the adverse pressure gradient was assumed to delay separation and causes the increased lift force in the rotor blade. Furthermore, it was inferred that the inertial force within the boundary layer flows is of minor importance for stall delay. Dumitrescu [32, 41] stated that these arguments were incorrect. The potential flow approach is not suitable to describe a phenomenon with complex dynamics, arguing that the centrifugal and Coriolis forces within the separated boundary layer are the root causes for stall delay.

3. 3D EFFECTS ON THE INVISCID AND THE VISCOUS FLOW

In the present studies, these conflicting arguments are intended to be answered. It will be shown in the following discussions that both arguments are correct. They are interacting each other and causing the 3D flow phenomena widely known as stall delay.

The computational setup employed in these studies is similar to what has been described in Section 3.2. The blade with the NACA 0010 airfoil shape is examined. The only difference is that the present examinations consider the effect of viscosity. Therefore, full 3D Navier-Stokes computations were carried out. The turbulent closure of the RANS equations uses the Menter SST $k - \omega$ model [102] assuming a fully turbulent boundary layer. Figure 3.24 presents the blade inviscid and viscous pressure distributions for the studied cases. Top figures (Figures 3.24a and 3.24b) are for $\lambda_{c/r=1.0} = 10.0$, middle figures (Figures 3.24c and 3.24d) for $\lambda_{c/r=1.0} = 5.0$ and bottom figures (Figures 3.24e and 3.24f) for $\lambda_{c/r=1.0} = 3.33$. Two radial stations are examined: $c/r = 0.5$ and 1.0. Solid black lines represent 3D inviscid results, dash dotted green lines are for 3D viscous results. Two-dimensional inviscid and viscous (at $Re = 40000$) results are also presented for comparison, represented by dashed red lines and solid blue lines, respectively.

In Figure 3.24, it is shown that the fluid viscosity reduces the tendency of the suction peak reduction for the 3D inviscid case, especially for the case with a larger c/r ratio. A similar behaviour is also observed for larger angles of attack. This agrees with the studies carried out by Snel [27]. As a consequence, the 3D viscous results become closer to the 2D inviscid situation. The difference between the 3D inviscid and viscous pressure distributions can be interpreted as the viscous rotational effects occurring on the blade. Despite that, the phenomenon contradicts routinely observed 2D inviscid - viscous aerodynamics. In 2D, due to frictional forces, a no-slip condition needs to be achieved on the blade surface, creating a momentum deficit on the streamwise velocity component. The displacement effect takes place causing a decambering effect, which reduces the suction peak in case of 2D viscous flows. At high angle of attack, this can lead to flow separation. Note that the decambering effect is defined as the reduction of camber or angle of attack effectiveness due to excessive boundary layer thickness and flow separation. The generated backflow opposes the main flow field, causing the flow to move normal to the wall at the separation line for the 2D case [142].

However, the situation is different in 3D conditions where the crosswise radial velocity component is generated due to the centrifugal force and radial pressure gradient. The Coriolis force is then perceived by the flow as a 3D response from the radially outward flow, causing a flow acceleration in chordwise direction. This becomes evident as the pressure coefficient becomes more negative on the suction side of the blade for the 3D viscous results. The centrifugal and Coriolis forces, acting within the boundary layer flows, are referred as the Himmelskamp force in the present studies. Beside that, the consideration of the fluid viscosity reduces the strength of the root vortex, allowing the blade section to have a stronger suction peak than in the 3D inviscid case described in Section 3.2. As becomes evident from the the radial distribution of the bound circulation (Γ) in Figure 3.25, the gradient of Γ in the
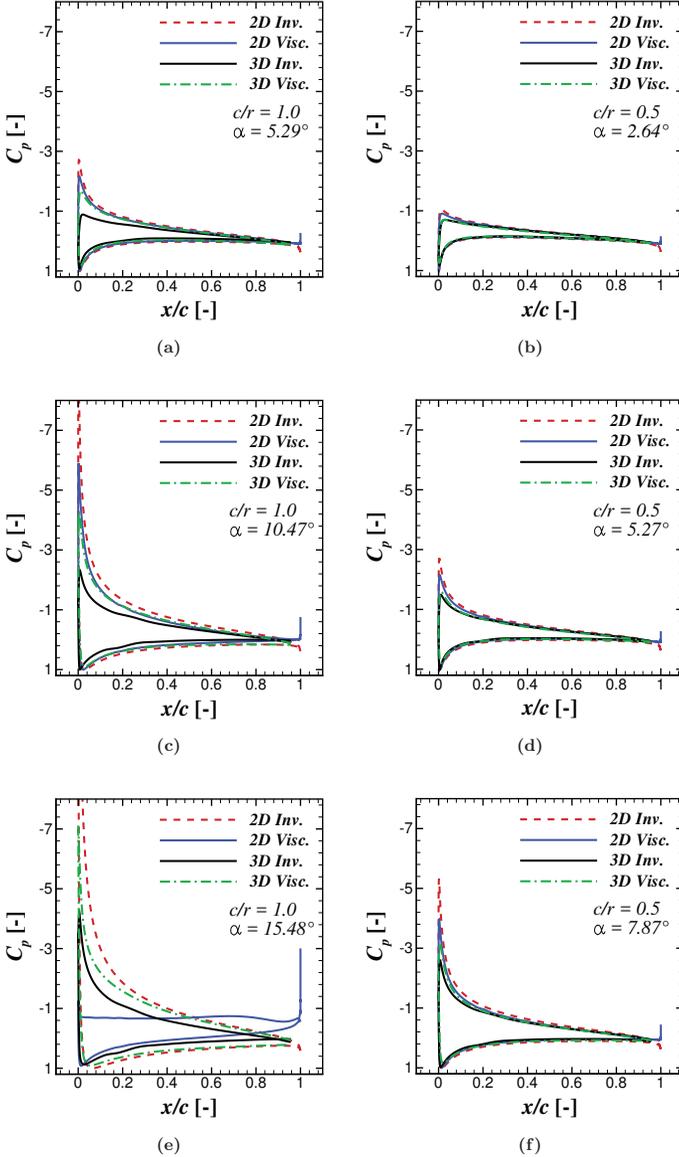
Figure 3.24: Viscous-inviscid pressure distributions on the blade with the NACA 0010 airfoil cross-section for $\zeta = 0.0$.
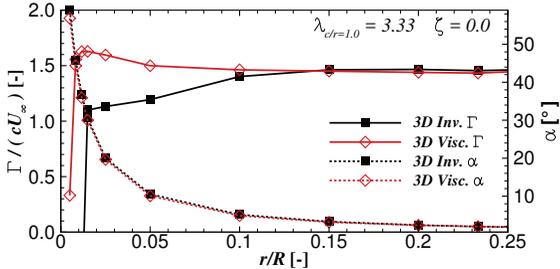
Figure 3.25: Bound circulation over the blade radius for $\zeta = 0.0$.

inboard area for the viscous case is less steep than the inviscid case.

Consider again the momentum equation in x-direction in Equation (3.4). The importance of the inertial forces in determining the viscous and inviscid flow field can be quantified. Figure 3.26 presents the distributions of the chordwise Coriolis (a_{crs}), centrifugal (a_{cs}), inertial ($a_{is} = a_{crs} + a_{cs}$) and convective ($a_x$) accelerations for the inviscid and viscous cases at two radial stations ($\zeta = 0.0$). It can be seen that the behaviours of the centrifugal and Coriolis terms change when the viscosity is introduced in the simulation. The magnitudes of a_{cs} and a_{crs} become more positive with increasing c/r, while a_{crs} remains negative for the inviscid flow regardless of the c/r value. a_{crs} is even stronger than a_{cs} in the front side of the airfoil at the extreme root area where $c/r = 2.0$, see Figure 3.26c. As a result, the inertial term is positive along the chord that helps the flow to overcome separation.

Figure 3.27 presents the variation of α when the center of rotation is shifted. It can be seen that the angle of attack distribution along the radius is influenced by ζ. The discrepancy is minimum in the extreme root area at $c/r = 2.0$. In Figure 3.28, the influence of the relative chordwise position of the center of rotation for the circulatory-viscous flow is presented for the blade section at $c/r = 2.0$. The value of ζ varies from -1.0 to 2.0. The minimum studied ζ corresponds to $1c$ upstream of the leading edge, while the maximum is for $1c$ downstream. The radial station of 0.5 m, corresponding to $c/r = 2.0$, was chosen in these evaluations. There is a possibility that the selected position is already inside the rotor hub, and the observation may not be directly applicable for wind turbine rotors. However, as already shown, the 3D effects become stronger approaching the root and it is interesting to investigate the 3D flow behaviour in the extreme root area. Furthermore, the variation of the angle of attack as ζ changes is minimum at this location. The computations were carried out for $\lambda_{c/r=1.0}$ = 3.33 at a sectional α of 28.17°. Two-dimensional viscous computation results at the same inflow conditions are presented for comparison. The employed Reynolds number is 40000. It is worthwhile to mention again that there is uncertainty of the angle of attack evaluation in the root area, which may affect the accuracy of the results.

It can be seen that pressure distribution varies significantly with variation of ζ. For
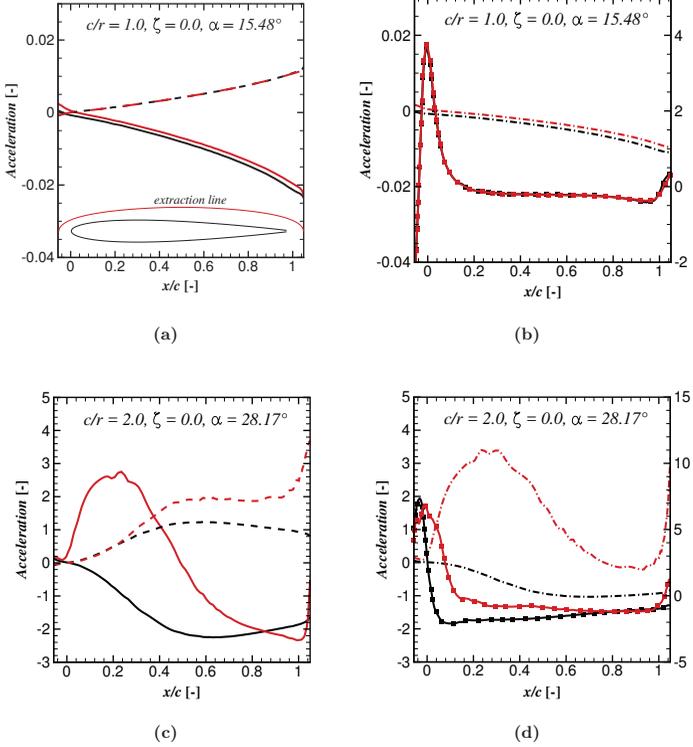
Figure 3.26: Acceleration terms quantification for the momentum equation in x-direction; a_{crs} (solid lines), a_{cs} (dashed lines), a_{is} (dash dotted lines) and a_x (symbolized lines). The suction side of the blade with the NACA 0010 airfoil shape is examined. The data are normalized by V^2/c. Black and red lines represent the inviscid and viscous cases, respectively. The figure scales for a_x are given on the right axis while the scales for the other parameters are shown on the left axis. The top figures show the data for $c/r = 1.0$ and the bottom figures are $c/r = 2.0$.

ζ = -1, the minimum pressure peak ($C_{p,min}$) is -16.35. This is significantly smaller than the pressure peak for the 2D case of $C_{p,min} = $ -1.31. It shall be noted that the flow is completely separated in the 2D viscous case. The minimum pressure becomes more positive successively with increasing ζ magnitude. It reaches $C_{p,min} = $ -2.68 for $\zeta = $ 2.00, but again this is still lower than the corresponding 2D situation. It is worthwhile
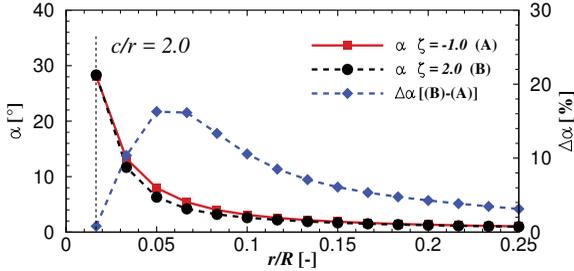
Figure 3.27: The effect of ζ on the angle of attack for the blade with the NACA 0010 airfoil shape. The angle of attack deviation is minimum at $c/r = 2.0$.
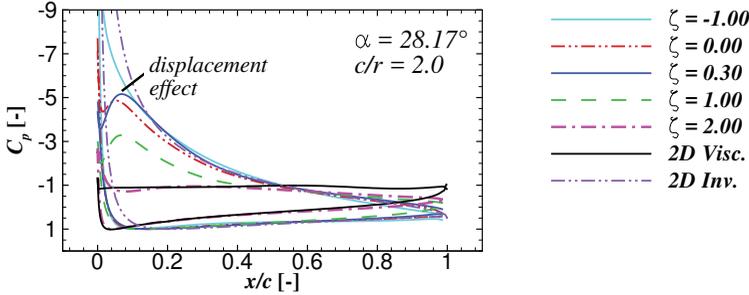
Figure 3.28: Effect of ζ on pressure coefficient of the blade with the NACA 0010 airfoil shape at $c/r = 2.0$.

to mention that $C_{p,min}$ for the 2D inviscid case is about -55.96. These observations are presented clearly in Figure 3.29a. The 2D inviscid minimum pressure is not presented for clarity.

Similar to the discussion for the non-circulatory flows in Section 3.1, the adverse pressure gradient alleviates for a larger ζ value. As a consequence from these C_p characteristics, the attained lift coefficient varies according to the chordwise location of the center of rotation, depicted in Figure 3.29b. It is shown that C_L generally reduces with increasing ζ. It shall be noted that the pressure gradient increases with decreasing ζ, indicating that the 3D effects become stronger with increasing pressure gradient. McCroskey & Yaggy [4] and Banks & Gadd [12] stated in their studies that the rotational effects become increasingly important as the chordwise pressure gradient becomes more adverse. Despite that, the theory was governed based on an assumption that the 3D effects are caused solely by the radial flow component, which is actually true as long as the flow is characterized by momentum deficit especially within separation
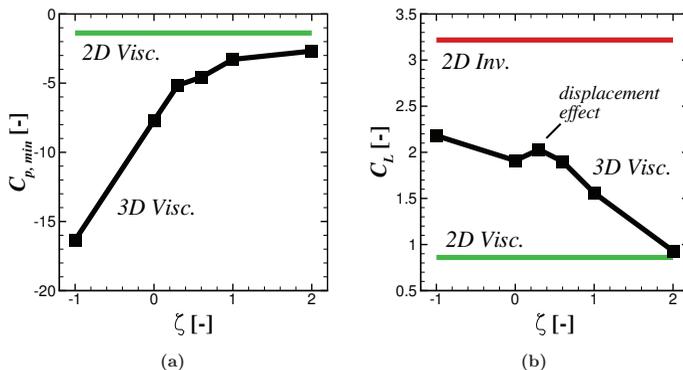
Figure 3.29: The minimum pressure (3.29a) and lift (3.29b) coefficients of the blade with the NACA 0010 airfoil shape at $c/r = 2.0$ as a function of ζ. The data are for $\lambda_{c/r=1.0} = 3.33$ at $\alpha = 28.17°$. Note that the 2D inviscid lift coefficient is obtained using XFOIL.

areas. The present studies demonstrate that the inertial forces have an influence on the three-dimensional flow characteristics in the root area even when the viscosity is completely removed from the analyses as long as the flow disturbance due to the rotor is present that further enhances the fundamental understanding of the three-dimensional effects.

Figure 3.30 presents the flow fields of the relative total fluid velocity (V/V_{kin}) obtained from the 2D and 3D viscous computations for various ζ values, where the total fluid velocity is redefined as $V = (v_x^2 + v_y^2)^{0.5}$. The extreme root area at $c/r = 2.0$ is investigated because this location shows a small variation of α as ζ changes. For the smallest studied ζ, it is shown that the flow is fully attached on the airfoil surface though the angle of attack is relatively high (28.17°). A small separation is observed near the leading edge for the case with $\zeta = 0$, *i.e.*, the center of rotation is located at the leading edge. This causes the minimum pressure level to become more positive and, as a consequence, reduces the lift coefficient of the airfoil as depicted in Figures 3.29a and 3.29b, respectively. The separation bubble increases in size at a higher ζ as shown in Figure 3.30c, and then the flow is reattached at $x/c = 0.58$. This enlarged bubble size, however, generates a stronger displacement effect than the other ζ values that locally enhances the velocity within this area as evident from the local pressure reduction for the case of $\zeta = 0.3$ presented in Figure 3.28. This causes the lift coefficient to increase up to $C_L = 2.03$. The effect is assumed to depend on the airfoil thickness. For example, the characteristics shall be different if the studied airfoil has no tendency to generate a separation bubble. Further increase of ζ enlarges the separation size greatly up to the trailing edge location. The occurring displacement effect is not able to compensate the strong reduction of the aerodynamic loss.
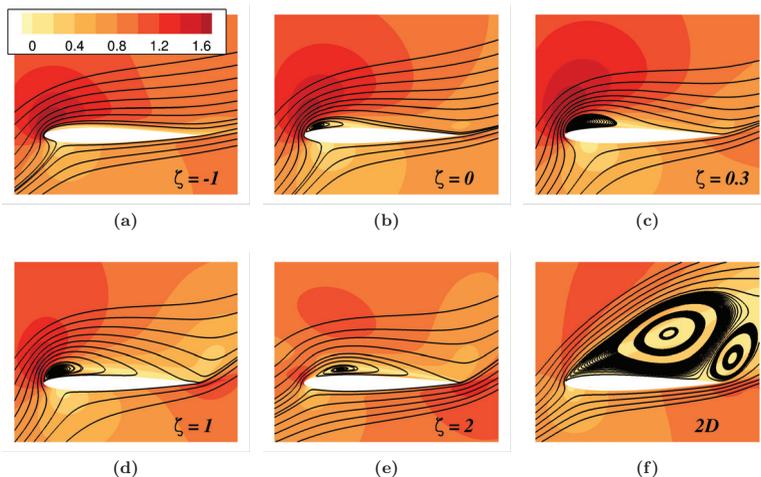
Figure 3.30: Flow separation characteristics for various ζ values coloured by the relative total velocity (V/V_{kin}) around the blade with the NACA 0010 airfoil cross-section at c/r = 2.0. All presented figures are from the viscous computations.
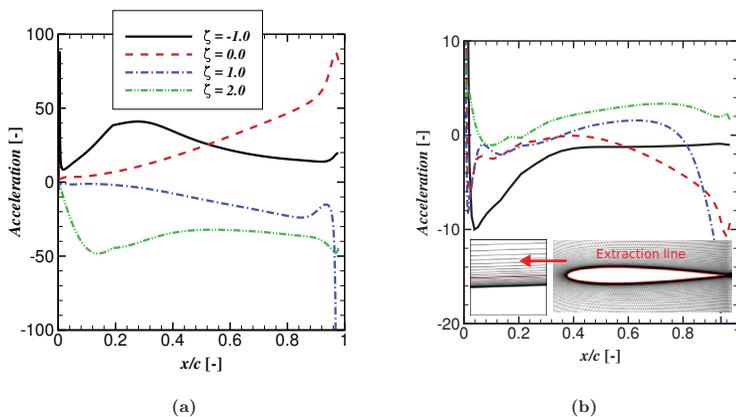
Figure 3.31: Acceleration terms quantification for the momentum equation in x-direction adjacent the wall; (a) a_{is} and (b) a_x. The suction side of the blade with the NACA 0010 airfoil shape at c/r = 2.0 is examined. The data are normalized by V^2/c.

Nevertheless, the size of separation area for all studied ζ is still smaller than in the 2D situation which shows strong massive separation. Additionally, Figure 3.30 reveals that the stagnation point moves upstream toward the leading edge with increasing ζ which becomes evident from the pressure distribution in Figure 3.28. The location of the stagnation point for the case of $\zeta = 2.00$ is similar to the 2D situation. This is caused by the superposition effect of the incoming velocity with the local blade circulation. As the lift coefficient reduces, the circulation magnitude also alleviates for a larger ζ which causes the upstream movement of the stagnation point.

It is interesting to see that separation becomes weaker with increasing pressure gradient (reducing ζ). In the 3D rotating blade, flow separation is not determined solely by the chordwise pressure gradient, but the inertial forces can play a huge role. Figure 3.31 presents the inertial and convective acceleration terms adjacent the blade wall at $c/r = 2.0$. Although a strong flow deceleration occurs just downstream of the leading edge for the case of $\zeta = $ -1.0, the inertial acceleration that acts in positive x-direction helps the flow to remain attached on the solid body.

3.4   Summary and Recommendation for the Blade Design

Studies on three-dimensional (3D) effects were commonly concentrated on the influence of radial flow on the viscous boundary layer. Accordingly, the effects of inviscid and viscous flow were mixed together so that the quantification of the inviscid effect was difficult. The studies on the inviscid effects are important because they drive the viscous effects and are already complex enough for the discussion of the 3D effects. On that basis, the present studies were conducted using both the Euler and the Navier-Stokes Computational Fluid Dynamics (CFD) approaches. Blades with elliptical and NACA 4 digit airfoil cross-sections were considered. Two different relative thicknesses, 10% and 20%, were chosen in the simulations. Various chordwise positions of the center of rotation (ζ) were investigated. The studies were divided into three main parts: (1) a steady flow without circulation was examined to isolate the inviscid effect from the influence of the trailing vortices, (2) the effect of circulation was investigated for the inviscid flow past rotating blades and (3) the inviscid - viscous effects were evaluated in detail to govern a fundamental understanding into the root causes of the 3D effects. From the studies, the mechanisms causing the 3D effects were identified:

- The inertial forces consisting of the centrifugal and the Coriolis forces (inviscid, non-circulatory flows, rotational effects).

- The downwash effect in the inboard area due to root vortices (inviscid, circulatory flows, root effects).

- The inertial forces consisting of the centrifugal and the Coriolis forces within the boundary layer (viscous, circulatory flows, rotational effects).

For the first part of the studies, the investigation shows that the C_p distribution in the vicinity of the blade root remarkably differs from the 2D case dependent on the

chordwise location of the center of rotation. If the center of rotation is shifted towards the trailing edge (higher value of ζ), a higher C_p value in the vicinity of the leading edge region is observed. The value is decreasing towards the trailing edge and the location of the minimum pressure is shifted. The effect increases with increasing chord to radius ratio (c/r), starting from $c/r \simeq 0.5$. It was observed that the present effect is more pronounced on the blade with the higher relative thickness of 20% chord. The flow curvature in the rotor and airfoil planes were observed to strongly influence the flow characteristics. The inertial forces consisting of the centrifugal and the Coriolis forces are identified as the main sources. These forces occur only when the flow is locally disturbed by the presence of the blade where the local flow acceleration is present and become zero far away from the blade. Depending on ζ, the inertial forces act in the same direction or against the main stream. The mechanism is described through the streamtube widening or contraction, resulting in a higher or lower pressure value, respectively. Furthermore, the acceleration terms contributing the momentum equation in streamwise direction are quantified and the effects are discussed. The present effect is strongly influenced by the location of the maximum airfoil thickness. The inviscid rotational effect has the weakest impact around this position (smallest difference in C_p value compared to 2D results was observed). In addition, the height for the minimum chordwise velocity tends to increase as the chordwise distance and c/r increase. The effect is expected to have a significant impact on boundary layer development of the flow near the root region of a rotating blade.

There are some consequences from the studies of the non-circulatory flows that need to be pointed out concerning the chordwise pressure gradient:

- For the non-circulatory flows, shifting the center of rotation more upstream tends to increase the adverse pressure gradient within the decelerating flow region.

- The adverse pressure gradient increases with c/r except near the leading and trailing edges.

- The location of the airfoil maximum thickness strongly influences the centrifugal force in the airfoil plane which defines the pressure gradient in the front side of the airfoil.

These studies are then further extended for the circulatory flows as discussed in the second part. It has been shown that the inviscid minimum pressure becomes more positive for a rotating blade compared to its corresponding 2D situation, reducing the pressure gradient on the blade suction side. The effect was observed to be stronger with increasing c/r and ζ as well as the angle of attack (α). The logarithmic difference between the minimum 3D inviscid to the minimum 2D pressure coefficients, $log(\Delta C_{p,min})$, almost linearly augments with increasing $log(\alpha)$. The finding shows that a simple correlation model for the 3D inviscid pressure coefficient can be derived based on simple 2D inviscid data. The phenomena are caused by the influence of strong vortices in the blade root area which confirms similar preceding studies. This generates the downwash effect that reduces the local angle of attack of the incoming

flow. A similar effect occurs near the tip due to a sharp radial gradient of the bound circulation. Therefore, this phenomenon can be categorized as the root effect instead of the rotational effect.

In the last part of the studies, the effect of viscosity is considered to distinguish the 3D effects caused by the inviscid or viscous flow involving massive separation. In these evaluations, it was shown that the viscous effect alleviates the tendency of the minimum pressure reduction for the 3D case, especially for a larger c/r magnitude or approaching the center of rotation. The downwash effect observed for the inviscid flow is weaker for the viscous flow. The Himmelskamp effect, generated mainly by two widely known inertial forces, the centrifugal and Coriolis forces, play an important role in determining the 3D flow field. The effects produce flow acceleration as becomes evident from the reduction of the pressure level on the suction side of the blade. It was observed that ζ has a strong impact on the 3D flow fields and the generated pressure distributions. The minimum pressure becomes more positive with increasing ζ, and accordingly the pressure gradient is weaker. These effects are present for both the inviscid and the viscous flows. A similar pattern is also observed for the lift coefficient where it reduces with increasing ζ, except at $\zeta = 0.3$ where the displacement effect of the separation bubble is stronger than the other ζ values. The size of the separated area enlarges at a larger ζ value indicating stronger separation. Despite that, the separation sizes for all the studied cases are still noticeably smaller compared to the 2D conditions. To sum up the studies, influences of the 3D effects on the pressure distribution are summarized in Table 3.1.

Based on these discussions, there are some concluding remarks and suggestions relevant for the airfoil/blade design which can be depicted from the present findings:

- The present studies answer the question related to the root cause of the 3D effects.

- The phenomena are generated by complex flow situations where both the inviscid and the viscous effects are of importance.

- The effects are controlled mainly by the the ratio of chord to radius (c/r) and chordwise distance of the center of rotation (ζ). The latter was not much evaluated in preceding studies for the 3D effects, but the importance was discussed in detail in the present studies.

Table 3.1: Influences of the 3D effects on the pressure distribution.

Case	Suction Peak	Separation Level
2D Inviscid	High	Attached
2D Viscous	Low	Massively Separated
3D Inviscid Small ζ	Medium	Attached
3D Viscous Small ζ	Medium-High	Lightly Separated
3D Large ζ	Medium-Low	Separated

3. 3D EFFECTS ON THE INVISCID AND THE VISCOUS FLOW

- It is possible to improve the aerodynamic performance of the blade section by applying the present knowledge for the 3D effects. It is suggested to shift the center of rotation in chordwise direction further upstream, reducing ζ, as it was shown to produce significantly weaker separation and a higher attained lift coefficient. Although the chordwise pressure gradient is increasing with reducing ζ, the positive inertial force helps the flow to overcome separation.

- If the upstream shift of ζ is not possible due to limitation of the structural constraints, ζ shall be set at a certain value so that the displacement effect of the separation bubble can lead to the increased lift benefit. For the present studies, this occurs at $x/c = 0.3$. The position may vary depending on the airfoil thickness, camber and separation characteristics.

Chapter 4

3D Flow on the MEXICO Rotor

This chapter is constructed based on the following articles:

- *G. Bangga, P. Weihing, T. Lutz, E. Krämer, Effect of computational grid on accurate prediction of a wind turbine rotor using delayed detached-eddy simulations, Journal of Mechanical Science and Technology 31(5), 2359-2364, 2017. Springer.*

- *G. Bangga, T. Lutz, E. Krämer, Root flow characteristics and 3D effects of an isolated wind turbine rotor, Journal of Mechanical Science and Technology 31(8), 3839-3844, 2017. Springer.*

The FLOWer code was extended for wind energy applications firstly at the IAG by Streiner [143] in his PhD thesis, and it was validated several times in numerous publications [59, 77, 78, 128, 129, 135, 144]. Despite that, the predictions become delicate if massive flow separation in the root area needs to be accurately resolved. As the complex separated flow in the blade inboard area is the main source for the viscous rotational effects, like it was described in Chapter 3, it is necessary to demonstrate that the employed CFD simulations are able to model the phenomena. Major parts of the present chapter are devoted to this purpose. The model rotor from the MEXICO project is used as a reference case since wind tunnel measurements are available [144]. The chosen test case for the simulation is presented in Section 4.1, where descriptions of the rotor, mesh and computational methods are given. The code validation is presented in Section 4.2. Then, in Section 4.3, the discussion is directed towards the root flow characteristics of the rotor in the near wake area, involving the near wall radial velocity component that has an impact on the 3D effects. At last, the 3D effects occurring on the blade is presented in Section 4.4.

4.1 Test Case and Computational Setup

The investigations were performed for the isolated MEXICO rotor from the new MEXICO experiment [119] operating at the wind speed (U_∞) of 24 m/s and

rotational speed (n) of 424 rpm ($\Omega = 44.4$ rad/s). A small tip-speed ratio of $\lambda = 4.2$ and a pitch angle of $\alpha_0 = $ -2.3° (towards stall) were considered. The conditions evoke massive flow separation over a wide range of the blade radius. This specific case was purposely chosen because 3D flows are often related to flow separation as pointed out in Chapter 3, and the new MEXICO measurements are considered a good validation case for the present numerical studies on 3D (separation) effects. Furthermore, the test case is challenging because CFD simulations usually struggle in predicting fluid flows involving massive separation.

The computational grid consists of several components, background (BG_m), wake refinement (R_m) and blade (B_m) meshes, shown in Figure 4.1. No hub, nacelle and tower were modelled in the present studies. This is done to simplify the geometry and to assess the effect of strong root vortices for a wind turbine blade consisting of relatively thick airfoils. In Chapter 3, discussion of the root vortex influence on blade pressure distributions was given, and further elaboration of the hub vortex importance is necessary. The overset (Chimera) method was applied, enabling high quality meshes to be built independently for each component. The size of the background grid is $10R$ in all distances, where R is the blade radius. The wake refinement mesh (R_m) starts from -$0.5R$ upstream of the rotor extending downstream up to $2.5R$. All meshes were built as 120° model, assuming flow periodicity using the periodic boundary condition. By doing so, cheaper computations can be performed.

At first, two different resolutions of the blade mesh were examined for the O mesh topology. The coarse mesh ($G1$) consists of 225x128x240 cells in chordwise, normal and radial directions, respectively. Among them, 40 cells are located across the boundary layer. The fine mesh ($G2$) consists of 256x152x384 cells. For $G2$, the cells are equally spaced in spanwise (radial) direction over a wide range of the blade, whereas $G1$ implies a tanh-type distribution. The meshes were refined near the root and the tip. The relative size ratios for cells on the blade surface of $G2$ are $\Delta/c \approx 3.8\%$ in spanwise and $\Delta/c \approx 1.5\%$ in chordwise directions. All the meshes use the same near wall grid distance of $y^+ < 1$ to properly resolve the viscous sublayer. The parameter changes slightly in the grid refinement and topology studies, but the variation is considered small as shown in Table 4.1. The cell size of the wake refinement mesh is of $\Delta = 0.045$ m. In total, the setup incorporating the fine blade mesh contains 27.3 million cells. Another mesh with C-H type topology was built using the same resolution as the fine mesh for comparison of the grid topology influence. However, due to the existence

Table 4.1: Grid statistics for the studied blade mesh. *Table is taken from [77].*

	O mesh		C-H mesh	
	$G1$	$G2$	$G1$	$G2$
Blade [million cells]	12.0	22.7	-	32.8
Total [million cells]	16.7	27.3	-	37.5
Averaged y^+ [-]	0.51	0.41	-	0.43
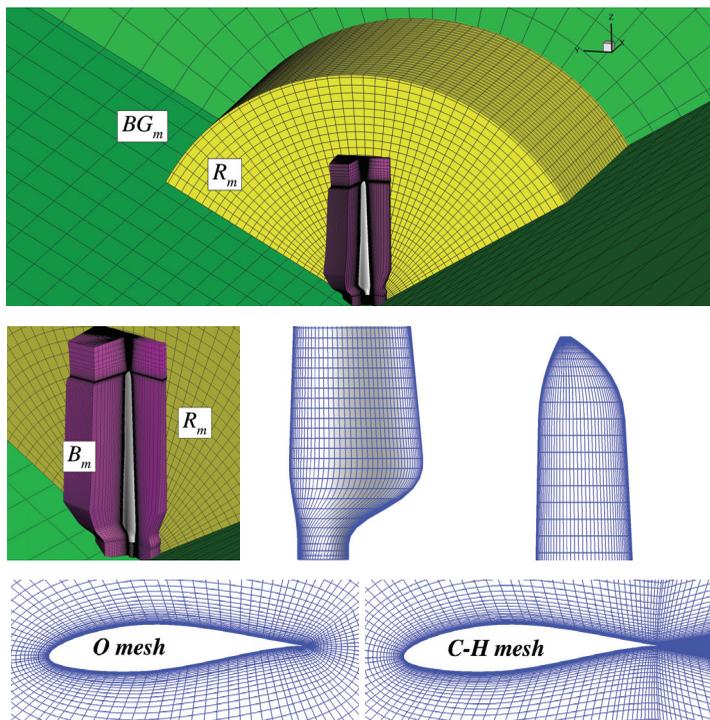
Figure 4.1: Computational mesh for the new MEXICO rotor. The background, wake refinement and blade meshes are indicated by BG_m (green), R_m (yellow) and B_m (purple), respectively. It shall be noted that the meshes are plotted at every 3th grid lines to avoid graphical interferences. *Figure is taken from [77].*

of the wake block mesh, the grid number increases up to 37.5 million cells. Detailed information of the number of cells can be seen in Table 4.1. All computations were carried out using 280 CPUs in parallel on the High Performance Computing Center Stuttgart (HLRS) employing the LAKI cluster.

The simulations were performed with the time step size of 0.000393 s, the equivalent to one degree blade revolution per physical time step. The time step can be calculated as $\Delta t[s] = \Delta t[°]/(\Omega.360°)$, where $\Delta t[°]$ is the azimuthal time step size in degree. The basic sensitivity to spatial and temporal resolutions for the 3-bladed rotor in the 120° model will be demonstrated for the isolated rotor, excluding the hub, nacelle and tower structures. Each physical time step is iterated towards a pseudo steady state using 35 sub-iterations. If not mentioned otherwise, the simulations use the DDES with the

RANS Menter SST turbulence model [83] near the wall and the WENO scheme [82]. However, due to stability concerns the latter is applied only outside of the boundary layer cells on the wake refinement mesh (R_m). The implementation and validation of the DDES approaches in FLOWer can be seen in [78]. The CFL numbers for the coarse and fine grid levels in the multi-grid scheme are 6.5 and 1.5, respectively. No laminar-turbulent transition is considered in the present studies.

4.2 Verification of the Numerical Schemes

4.2.1 Spatial Discretization Studies

Firstly, the calculations were carried out until the wake was fully developed, that was reached after 7 revolutions (see Figure 4.2). Afterwards, the simulations were restarted from this condition for additional 1 and 2 rotor revolutions. This was done for the data
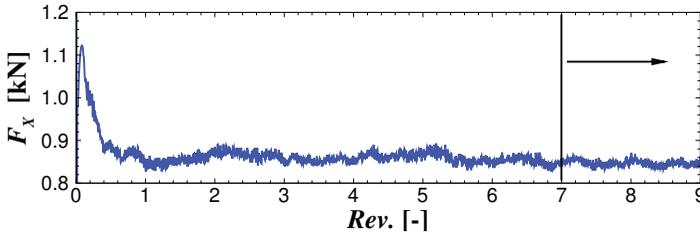
Figure 4.2: The rotor axial force (F_X) history during simulations. The arrow indicates the starting point of the data extraction.
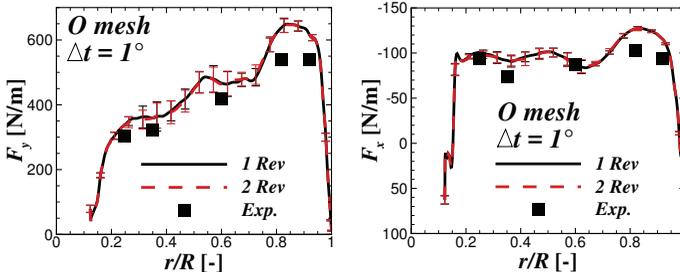
Figure 4.3: Time averaged chord normal (F_y) and tangential (F_x) loads over one and two rotor revolutions. The error bars indicate the standard deviation of the unsteady fluctuations. *Measurement data is obtained from [119]. Figure is taken from [77].*
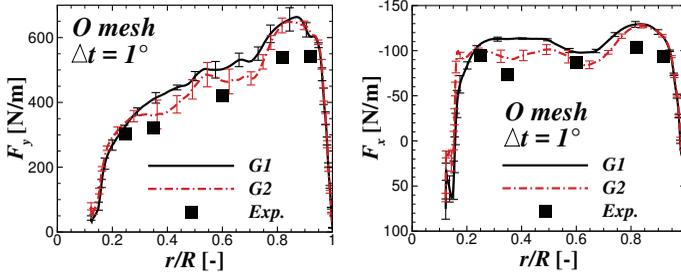
Figure 4.4: Impact of grid density on the blade loads. The error bars indicate the standard deviation of the unsteady fluctuations. Increased grid density improves the CFD predictions. *Measurement data is obtained from [119]. Figure is taken from [77].*
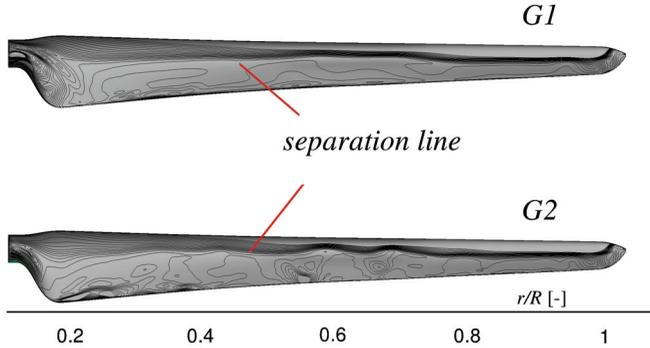
Figure 4.5: Instantaneous limiting streamwise velocity close to the blade surface at zero azimuth angle. Finer grid resolution resolves stronger unsteadiness that is not captured in the coarse mesh. *Figure is taken from [77].*

extraction purpose. Figure 4.3 shows the time averaged sectional loads in normal (F_y) and tangential (F_x) directions, relative to the local chord line. The standard averaging procedure, *i.e.,* the total sum of all values divided by the number of data, was applied over these additional simulations, excluding the first 7 rotor revolutions. The presented forces in Figure 4.3 were obtained from the simulation employing the $G2$ mesh with the O type topology. These forces were calculated by excluding the friction force from the blade load evaluation. This was done for consistency with the experiment [119] that used the pressure data only. It is worthwhile to mention that, in the experiment [119], the aerodynamic loads of the blade section were obtained by integrating the surface

pressure measurement. It was reported that the total number of pressure sensors is 148, distributed over 5 radial stations at $r/R = 0.25$, 0.35, 0.6, 0.82 and 0.92. It is shown in Figure 4.3 that the time averaged numerical results and their standard deviation have little dependency towards the number of revolutions from which the data are averaged. Thus, if no spectral data are of interest, the data extraction over one revolution is sufficient.

In Figure 4.4, the impact of grid density on the resulting aerodynamic loads is shown. It can be seen that the increased grid resolution improves the accuracy of the loads prediction especially within $0.25 < r/R < 0.82$. Smaller loads are observed for the fine mesh, which are closer to the measurement data [119]. It seems that the increased accuracy of the load prediction stems from the difference in separation characteristics, that is driven by the stronger unsteady effects for the fine mesh. It is shown in Figure 4.5 that the instantaneous wall shear stress distributions of the studied meshes at the same azimuth position are remarkably different. While the coarse mesh shows almost a linear line along the blade radius, the predicted separation line of the fine mesh is a bit wavy, indicating stronger unsteadiness. More complex wall shear stress pattern is also shown in the separation area. These phenomena are expected to influence the location of separation, that, as a consequence, affects the magnitude of the predicted forces.

4.2.2 Temporal Discretization and Mesh Topology Influences

This section demonstrates the impacts of two different mesh topologies and the temporal discretization on the CFD predictions. Figure 4.6 shows the sectional load distributions for the O and C-H meshes for three studied time step sizes, namely Δt = 1°, 2° and 3° of the blade rotation per physical time step. For definition of the time step, please refer to Section 4.1. In the rest of the studies, the time step size is defined in degree. It can be seen, for the O mesh, that the aerodynamic load prediction remarkably improves with increasing time step resolution from 3° to 1°, especially in the middle blade region between $0.27 < r/R < 0.8$ for F_y and within $0.27 < r/R < 0.7$ for F_x. On the other hand, it seems that the influence of the time step refinement on the blade load is weaker for the C-H mesh, inferring that the C-H mesh is less sensitive towards the temporal discretization.

This observation can be discussed based on the resolved wake adjacent to the blade trailing edge for the DDES simulations. The additional wake block existing in the C-H mesh leads to a finer grid resolution downstream of the trailing edge, see Figure 4.1. This smaller grid spacing (Δ) requires a significantly smaller time step for the CFD computations. According to Spalart [145], the required time step size for DES simulations can be estimated by $\Delta t = \Delta_0/U_{max}$, where Δ_0 is the target grid spacing within the LES area and U_{max} is the maximum convective velocity. Figure 4.7 illustrates the zone mapping of the DDES computations, the red and blue areas represent the URANS and LES zones, respectively. Note that a relatively large RANS area is still observed within the separated flow region due to the limitation of the spanwise grid resolution.

It can be seen that the C-H mesh employs a noticeably larger RANS area on the
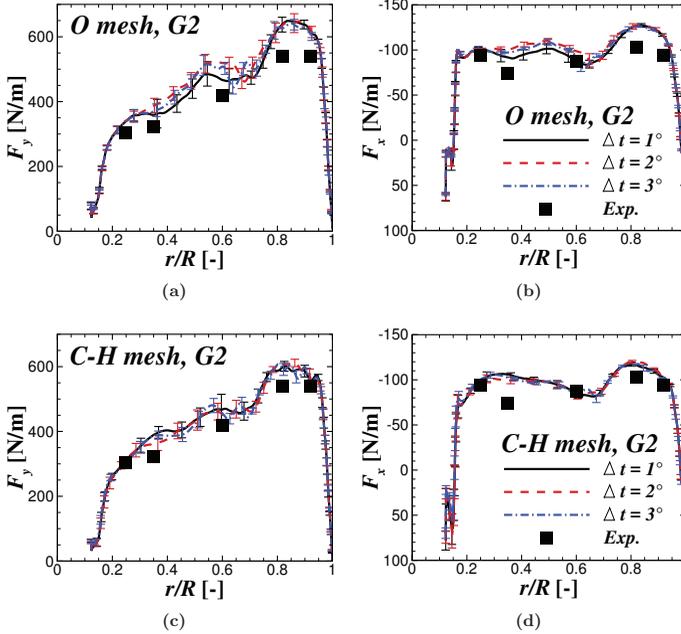
Figure 4.6: Temporal discretization influence on the blade loads for two studied grid topologies: O (top) and C-H (bottom) meshes. *Measurement data is obtained from [119].* *Figure is taken from [77].*

upper side of the blade compared to the O mesh topology. The first explanation may be related to the above explanation that the smaller time step is required for the C-H mesh for the DDES computations. This is supported by the fact that RANS area size does not considerably change for two different examined time step sizes in Figure 4.7. In contrast, a smaller RANS area is shown for the O mesh with decreasing temporal resolution. It implies that there is needlessly fine resolution to propagate from the viscous flow region to the Euler region for the C-H mesh. Spalart [145] defined the Euler region as the area that is never entered by turbulence.

The second explanation may be related to the shape and aspect ratio of the grid cells. From the mesh topology point of view, the existence of the wake block for the C-H mesh pushes the mesh on the upper and lower sides of the airfoil towards the leading edge, influencing the relative skewness angle of the cells within the LES area that affects the value of Δ. It is worthwhile to note that Δ is $f(\Delta_x, \Delta_y, \Delta_z)$. Hence the switching location of the LES to RANS regions obviously changes as a consequence.
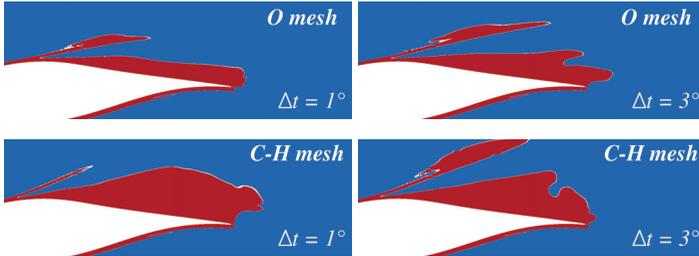
Figure 4.7: Representation of the LES and URANS areas around the blade section at $0.53R$ using DDES for O mesh (top) and C-H mesh (bottom). The inner red region denotes the URANS zone, the outer blue region the LES zone.

By default, in FLOWer, Δ is defined as

$$\Delta = \max(\Delta_x, \Delta_y, \Delta_z). \tag{4.1}$$

In terms of consistency and cost efficiency of the DES computations, the O mesh topology seems to be more promising. The general trend of the mesh topology influence, however, cannot be directly concluded. It is shown that the C-H mesh predicts slightly more accurate sectional loads at $0.25R$ compared to the O mesh. On the other hand the C-H mesh prediction is not so accurate at $0.35R$. However, this observation seems to be in good agreement with the other numerical studies by Weihing *et al.* [78] and Bangga *et al.* [77, 146] for the same rotor that also observed the over-prediction at $0.35R$. They argued that as no nacelle is modelled, the root vortex becomes significantly stronger compared to the case where the blade root is properly connected with the actual hub. This leads to a nozzle like acceleration in the rotor center, that both increases the "wind" velocity seen by the airfoil and its angle of attack, resulting in the overestimation of the loads at this position [78]. Nevertheless, the C-H mesh prediction in the outboard region of the blade is significantly more accurate than the O mesh.

Figure 4.8 shows the extracted pressure coefficient (C_p) at $0.6R$ and at $0.92R$. The pressure is non-dimensionalized by the local chord length and kinematic velocity $V_{kin} = (U^2 + (\Omega r)^2)^{0.5}$, with r being the radius of the blade section from the origin. The results are compared to measurement which was evaluated using the same kinematic velocity as in the present simulations. It shall be noted that the available data in [119] is the pressure data ($p = p_{static} - p_{inlet}$). From top to bottom are the radial positions of $0.25R$, $0.35R$, $0.6R$ and $0.92R$, respectively, for two examined time step sizes. It can be seen that the time averaged C_p distribution of the blade section is influenced by the mesh topology. The C-H and O mesh topologies have very similar C_p distribution for the radial position of $0.25R$ regardless the time step size. Slightly further outboard, at $0.35R$, both mesh types show similar results for the time step of 2°, but the O mesh prediction comes closer to the experimental data for $\Delta t = 1$° while the C-H mesh remains insensitive towards the time step influence. In the middle and outer
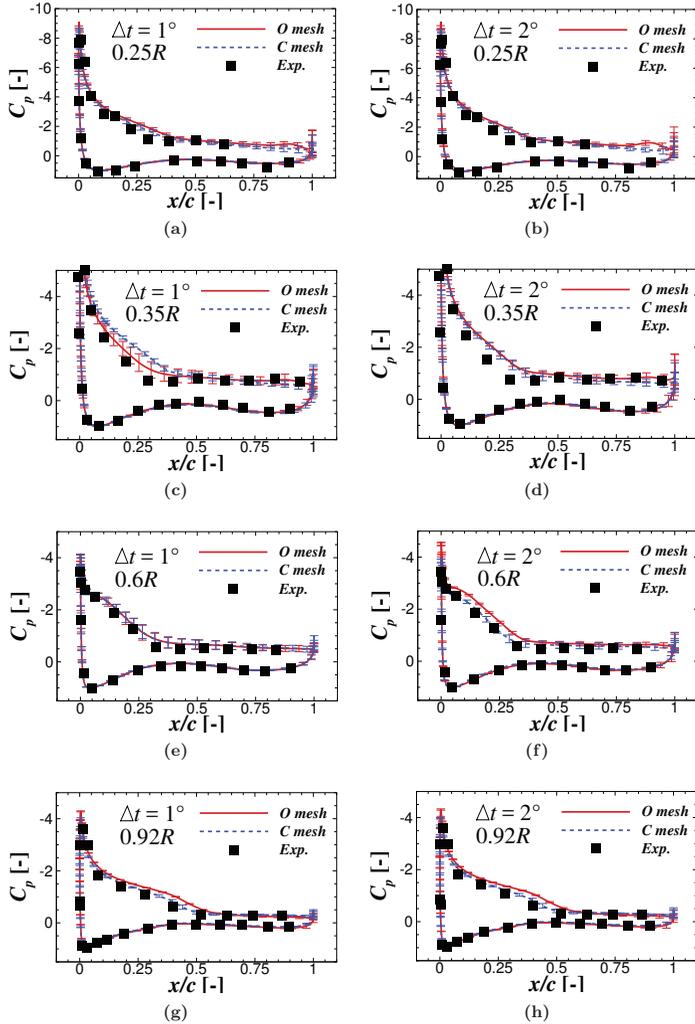
Figure 4.8: Time averaged C_p distribution of the blade section for two examined time step sizes, $\Delta t = 1°$ and $\Delta t = 2°$, at $0.25R$ (Figures 4.8a-4.8b), $0.35R$ (Figures 4.8c-4.8d), $0.60R$ (Figures 4.8e-4.8f) and $0.92R$ (Figures 4.8g-4.8h). *Measurement data is obtained from [119]. Figures 4.8e - 4.8h are taken from [77].*
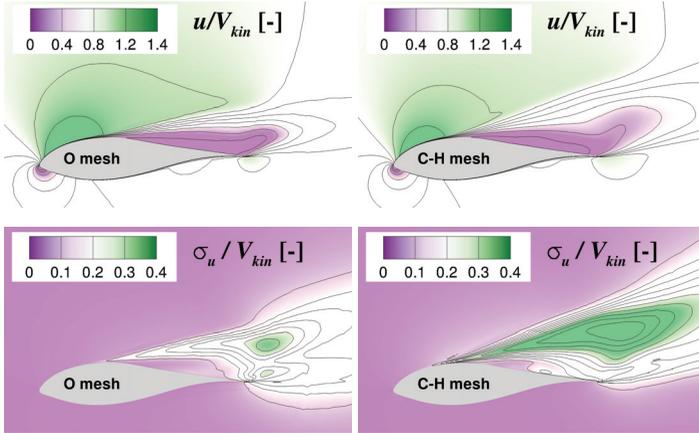
Figure 4.9: Time averaged streamwise velocity (top) and its fluctuation (bottom) contours around the blade section at $0.6R$ and at $\Delta t = 2°$. The C-H mesh predicts slightly stronger separation with remarkably stronger fluctuation within the separated flow region.

radial stations, at $0.6R$ and $0.92R$, the C-H mesh shows better accuracy compared to the O mesh topology especially within the decelerating flow regime downstream of the minimum C_p peak and prior to separation at large time step size ($\Delta t = 2°$). By refining the time step resolution, $\Delta t = 1°$, the accuracy of the CFD results using the O mesh is improved especially in the middle blade area, but less prominent for the outer blade area since there, one convection over the airfoil is resolved by only a few time steps. This observation stems from the fact that the circumferential velocity of the outer blade region is significantly higher than the blade inner and middle stations. As a consequence, a much smaller time step size is required for the blade outer region. In general, the CFD predictions for both examined grid topologies accurately capture the experimental data as long as the time step size is sufficient even though small deviations are shown.

It can be seen that deviations of the C_p distribution for the different mesh topologies are located upstream of separation, not within separated flow region. For example, in Figure 4.8d, the deviation is located from the suction peak up to $x/c = 0.37$, but the pressure recovery is similar for both meshes further downstream. This can be explained by observing the time averaged streamwise velocity field in Figure 4.9 (top). The simulation employing the O mesh predicts a higher velocity on the suction side of the airfoil compared to the C-H mesh. The separated flow region for the C-H mesh occupies a larger region in wall normal direction (purple area in the upper side of the airfoil) compared to the O mesh. This deflects the mean flow on the upper side of the airfoil that the fluid particles see a "thicker" obstacle than the actual airfoil body,

creating a displacement effect. Thus, a less negative pressure is observed for the C-H mesh upstream of separation that is closer to the measured data [119]. Furthermore, this effect is generally associated with the position of separation. It can be seen that the C-H mesh predicts earlier separation than those predicted by the O mesh, especially in Figures 4.8d, 4.8e and 4.8f. In addition, it seems that the C-H mesh, which consists of a lot more cells downstream of the airfoil, captures stronger unsteadiness compared to the O mesh as depicted in the normalized standard deviation contour in Figure 4.9 (bottom). This indicates that the C-H mesh is better in resolving the shedding of the small scale eddies. Nevertheless, both meshes show similar results in the aerodynamic loads inferring that the impact of the observed fluctuations is minor of importance for the mean properties.

4.2.3 Sensitivity Against the Employed RANS Model

It is already well known that accuracy of CFD computations depends strongly upon the employed turbulence models [104]. To study this issue, a DDES simulation using SA as the RANS model was carried out and compared to the DDES-SST results for the same time step size ($\Delta t = 1°$). This simulation was performed using the $G2$ mesh with the O-type topology, please refer to Section 4.1 for the description of the mesh resolution and the simulation strategy. Figure 4.10 illustrates the wake structures downstream of the MEXICO rotor. It presents the iso-surface of the λ_2 criterion and the vorticity field in Y-direction. Figure 4.10a represents the wake for the CFD computations calculated with the C-H mesh and DDES-SST turbulence model, Figure 4.10b is for the O mesh and DDES-SST turbulence model, and Figure 4.10c is for the O mesh and DDES-SA turbulence model.

It can be seen that the C-H mesh topology resolves smaller turbulent structures better than the O mesh topology around the blade. This is, however, already expected because it contains an additional wake block downstream of the blade that does not exist for the O mesh topology. Therefore, additional computational cost for the C-H mesh occurs as a consequence. It is worthwhile to mention that massive flow separation covers almost the whole blade radius, and the presented flow structures in Figure 4.10 are caused by the separated flow. These fine flow structures are significantly smeared out when the O mesh is used, especially if the DDES-SA turbulence model is employed. It can be observed that the selection of the grid topology and turbulence model becomes more crucial for the separated flow around the tip area, where the fine turbulent structures are less resolved.

The wake downstream of the rotor in Figures 4.10a and 4.10b look similar, characterized by randomly distributed vortices, while it seems to be more structured in Figure 4.10c. Although the regions outside of the boundary layer are computed with LES (depicted in Figure 4.7), the flow characteristics within these areas are observed to be influenced by the employed RANS model. In the DDES computations, the RANS model has a strong influence in modelling the onset of separation because it is employed within the boundary layer, and it has been widely documented that the location separation point often varies depending on the used RANS turbulence

(a)

(b)

(c)
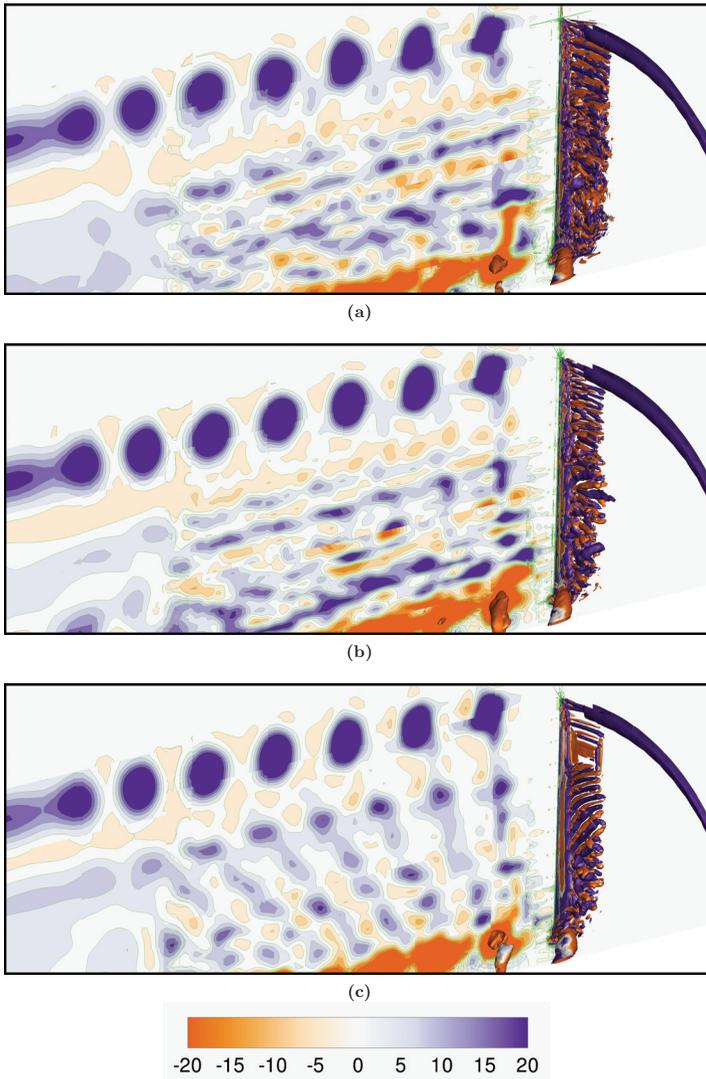
Figure 4.10: Instantaneous iso-surface of the λ_2 criterion ($\lambda_2 = $ -4136 s^{-2}) for $\Delta t = 1°$ coloured by the vorticity in Y-direction [1/s]. From top to bottom: C-H mesh (DDES-SST), O mesh (DDES-SST) and O mesh (DDES-SA), respectively. The C-H mesh employing the SST turbulence model shows the richest resolved structures. The fine turbulent structures become less resolved from top figure to bottom.
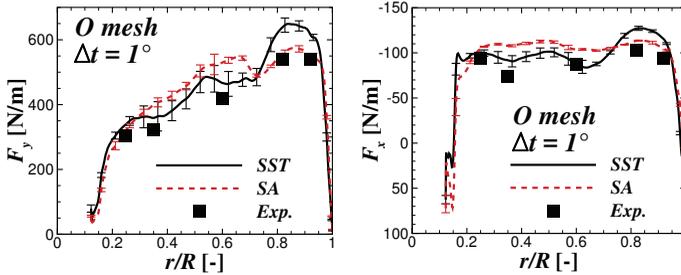
Figure 4.11: Impact of turbulence model on blade loads using O mesh for $\Delta t = 1°$. The SST turbulence model shows better agreement against measurement data for the blade inboard region, but not so accurate near the tip compared to the SA RANS model. *Measurement data is obtained from [119]. Figure is taken from[77].*

models [147]. The flow characteristics obtained from the RANS simulation act as an input for the LES mode in the RANS-LES switching boundary. As a consequence, the LES computations are less characterized by the random motion of turbulence if the RANS model predicts weaker flow separation.

The SA turbulence model is likely to be more "steady" than the SST model and, thus, triggers less unsteadiness in the LES area as made evident by the wake structures discussed above. This behaviour is shown in the sectional loads distribution in Figure 4.11, where the SA results present weaker fluctuations compared to the SST's, particularly for the tangential force (F_x). The DDES-SST turbulence model shows better results than the DDES-SA model for the whole blade radius, except around the tip area. However, the reason for the deviation near the tip seems rather ambiguous. Within this area, as shown in Figure 4.10c, the trailing vortices predicted by the DDES-SA model are smeared out and their inductive effects on the local lift distribution is moderated. The context becomes clearer when the inner region is considered as both models show similar eddy structures whereas the SST model gives better prediction against measurement data.

Generally, based on the above discussions, the DDES-SST model provides better prediction for the MEXICO rotor operating under massive flow separation. The over-prediction against the measurement data near the tip region is expected to stem from two main reasons, physically and numerically. As the physical explanation, no boundary layer tripping was used around the tip in the measurement [119], but was applied in the other areas. Thus, fully turbulent computations are not sufficient for that. Numerically, DDES computations require very small time steps to resolve the small structures in the blade outer area because the local circumferential flow velocity is large. It shall be noted that the time step size is inverse proportional to the convective velocity of the flow. The use of very small time steps was shown to improve the prediction around this area in [78]. Furthermore, different grid topologies are shown to have an influence.

As depicted in Figure 4.6, the C-H mesh has better agreement near the tip than the O mesh, but the results are similar for the rest of the blade area. For further simulations, this particular setup, employing the C-H mesh and DDES-SST turbulence model, is applied unless stated otherwise. For the MEXICO rotor, all evaluations of the 3D flows are carried out using $\Delta t = 1°$.

4.3 Root Flow Characteristics

It is worthwhile to mention again that no hub was modelled in the present studies. Hence, the rotor consists of a hole around the center of rotation. This approach is often found in the numerical analyses of wind turbine rotors [77, 78, 148, 149] because the hub geometry is considered to have little influence on the aerodynamic loads. Furthermore, it was shown in Section 4.2 that the CFD approaches are able to accurately predict the aerodynamic loads acting on the rotor. Despite that, neglecting the hub may evoke unrealistic root vortices, and evaluations of these phenomena are necessary. In Chapter 3, it was documented that the root vortices cause reduction of the suction peak for the inviscid flow, and this effect is alleviated when the fluid viscosity is considered. The present studies are intended to assess the effect of the strong root vortices on the global flow characteristics.

In this section, three-dimensional instantaneous flow fields for three different velocity components, namely axial, circumferential and radial directions, in the near wake region of the isolated MEXICO rotor are evaluated. The reader is suggested to refer to Section 4.1 for the operating condition of the rotor. The blade position for the present examinations is at zero azimuth angle. The upper side of the blade represents the suction side while the lower side is the pressure side. The evaluations are performed for three different azimuth planes, namely at $\theta = 0°$, $\theta = -45°$ and $\theta = -90°$. The cases for $\theta = -45°$ and $-90°$ correspond to 45° and 90°, respectively, downstream of the blade trailing edge. For the 120° simulation model, due to flow periodicity, the extraction plane for $\theta = -90°$ is represented by the plane at $\theta = 30°$ upstream of the leading edge. For the definition of the azimuth angle, please refer to Figure 2.5. The results are presented in Figures 4.12, 4.13 and 4.14. The presented velocity distributions are non-dimensionalized by the freestream velocity of 24 m/s. The wind speed is in positive X/R direction (in vertical axis), while the horizontal axis represents radial direction. In these figures, a positive axial flow is in $+X/R$ direction (same as the wind), positive radial velocity in $+r/R$ and the circumferential velocity in the third component of the coordinate axes, in counter-clockwise direction relative to θ. It shall be noted that the scale of the radial and axial axes as well as the contour scale are different between each velocity component.

The axial velocity contours in near the wake region around the root area for three azimuth positions are presented in Figure 4.12. A remarkable increase of the axial velocity is observed in the root where no hub is introduced. However, the influence of this nozzle-like flow field seems to be small as the predicted blade loads are in good agreement with the measured data even though the experiment employed a proper

hub connection, except at $r/R = 0.35$ where the axial and tangential forces are overestimated. At $\theta = 0°$, it can be seen that the axial flow acceleration in the root area is concentrated from the center of rotation up to the blade end section ($r/R \approx 0.12$). The root flow acceleration seems to occupy a larger area successively at $\theta = -45°$ and $\theta = -90°$, especially close to the rotor plane at $X/R = 0$. Akay *et al.* [150, 151] and Sherry *et al.* [152] observed also a similar phenomenon. Despite that, in their studies the increase of U was caused by the radial flow that is directed towards the center of rotation as a result from the nacelle flow interaction. In fact, if the blade was properly connected to the nacelle as in their studies, the velocity increase was not as high as the present observation. The magnitude of U/U_∞ is slightly higher than unity which is significantly above the expected axial velocities based on the momentum theory.

As can be seen in Figure 4.13a, the lower side of the blade is characterized by a negative azimuthal velocity component. This is caused by the local motion of the fluid flow around the blade from the stagnation point towards the leading edge of the blade, and its direction is the same as the rotor motion. In contrary, this particular fluid flow opposes the rotor direction on the suction side and its magnitude is increased by the displacement effect. Furthermore, it is shown that positive magnitude of the velocity component dominates the flow field downstream of the rotor at $\theta = 0°$. This observation shows that the inviscid part of the flow field rotates opposite to the rotor, in agreement with the momentum theory. A similar observation was also given in [150, 151].

Some regions downstream of the rotor ($X/R > 0$) are locally characterized by negative circumferential velocity fields. These are observed at $X/R \approx 0.4$ and 0.8 for $\theta = 0°$, $X/R \approx 0.1$ and 0.5 for $\theta = -45°$ and $X/R \approx 0.3$ and 0.7 for $\theta = -90°$, marking the location of the nearby vortices in the wake area along the blade radius. The origin of this phenomenon is expected to stem from two main factors: (1) the change sign of the trailing vortices due to the positive/negative gradient of the bound circulation along the blade; and (2) the interaction of the current and previous blade passages as discussed in [150–152]. Regarding to the latter effect, it is shown that the strength of the velocity interaction between the blade passages decreases with increasing streamwise distance. This effect starts just after the boundary layer materials shed into the wake area and are dragged together with the rotor motion [150, 151]. As no hub is introduced, this phenomenon becomes remarkably strong near the root area at $X/R \approx 0.27$. It is expected that the local root flow circulation in the wake is stronger than if the blade is properly attached on a nacelle. Furthermore, it is shown that the radial expansion of the most inboard root vortices seems very weak due to the nozzle effect.

The third component of the near wake flow, *i.e.,* the radial flow, for the isolated MEXICO rotor is presented in Figure 4.14. Similar to the observation of the circumferential velocity, the root vortices are clearly observed for this velocity component. The location of the vortices is marked by the change of sign of the radial velocity. In the inboard area, a distinct root vortex is observed approximately at $r/R = 0.15$. It can be seen that the root vortices move in helical fashion as the blade rotates, as can be depicted from the velocity contour planes at $\theta = 0°$, -45° and -90°

(a) $\theta = 0°$

(b) $\theta = $ -45°

(c) $\theta = $ -90°
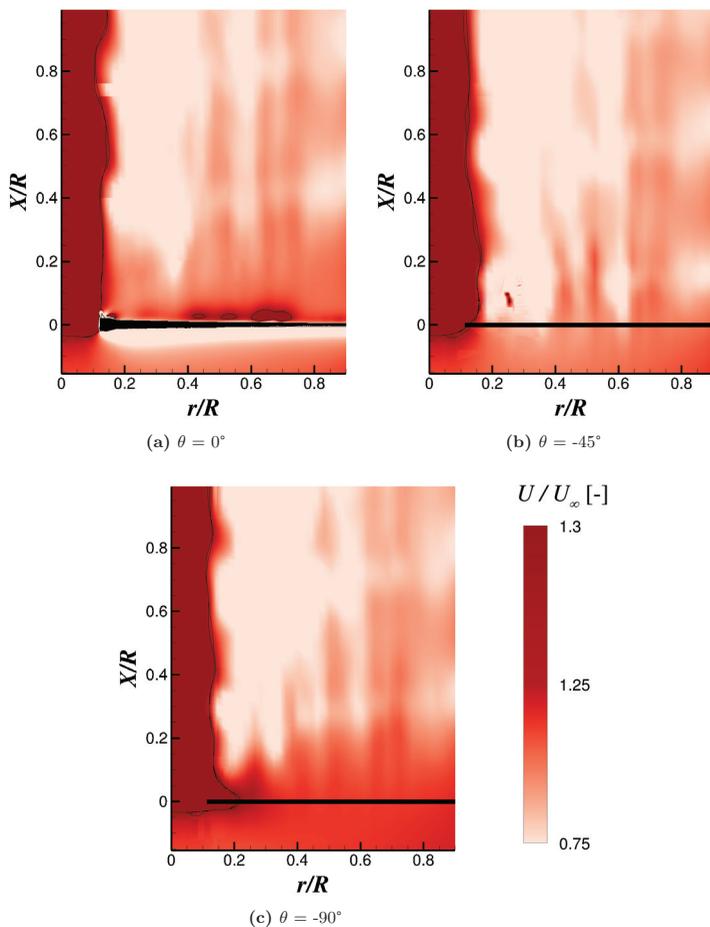
Figure 4.12: Dimensionless axial velocity distributions for three different azimuth angles, 0° (4.12a), -45° (4.12b) and -90° (4.12c). Inflow is in $+X/R$ direction. Black line indicates the position of the blade. The contour line indicates the magnitude of $U/U_\infty = 1$. A small discontinuity of the contour in Figure 4.12b at $r/R = 0.25$ and $X/R = 0.1$ is caused by errors in the Chimera interpolation within the overlapping meshes. *Figures 4.12a and 4.12b are taken from [146].*

(a) $\theta = 0°$

(b) $\theta = $ -45°

(c) $\theta = $ -90°
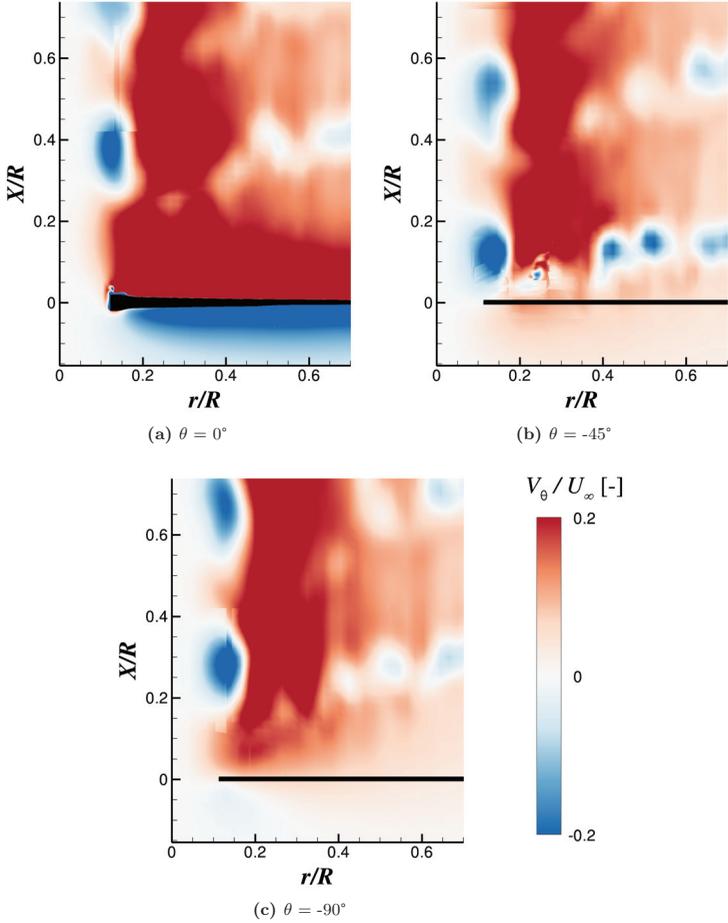
Figure 4.13: Dimensionless circumferential velocity distributions for three different azimuth angles, 0° (4.13a), -45° (4.13b) and -90° (4.13c). Inflow is in $+X/R$ direction. Black line indicates the position of the blade. A small discontinuity of the contour in Figure 4.13b at $r/R = 0.25$ and $X/R = 0.1$ is caused by errors in the Chimera interpolation within the overlapping meshes. *Figures 4.13a and 4.13b are taken from [146].*

(a) $\theta = 0°$

(b) $\theta = $ -45°

(c) $\theta = $ -90°
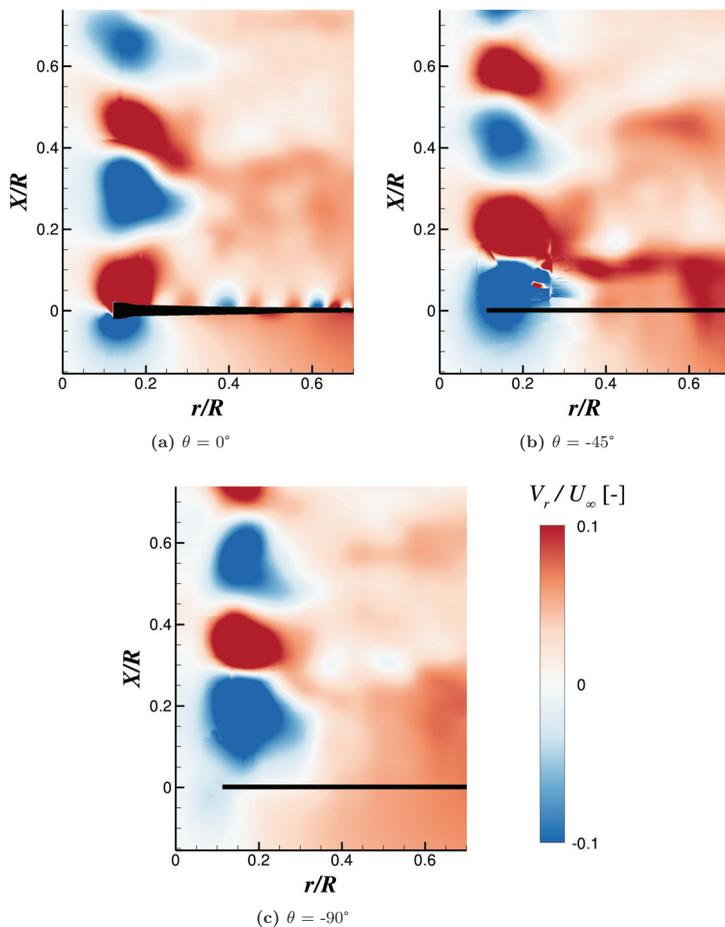
Figure 4.14: Dimensionless radial velocity distributions for three different azimuth angles, 0° (4.14a), -45° (4.14b) and -90° (4.14c). Inflow is in $+X/R$ direction. Black line indicates the position of the blade. A small discontinuity of the contour in Figure 4.14b at $r/R = 0.25$ and $X/R = 0.1$ is caused by errors in the Chimera interpolation within the overlapping meshes. *Figures 4.14a and 4.14b are taken from [146].*
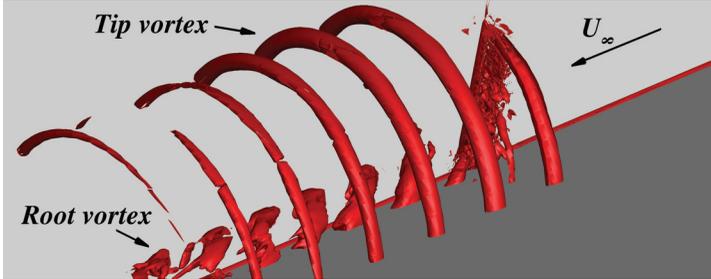
Figure 4.15: Iso-surface visualizing the vortical structures downstream of the rotor by $\lambda_2 = -413$ s^{-2}. *Figure is taken from [146].*

and from the iso-surface in Figure 4.15. At $\theta = 0°$, a powerful outboard motion of the fluid flow is observed adjacent to the suction side of the blade surface, dominating up to $r/R \approx 0.2$. This is caused by the root effect of the isolated rotor. A similar phenomenon was observed to occur near the tip area, but in opposite direction. In contrast, in the range of $r/R = 0.375\text{-}0.42$ and around $r/R = 0.6$, the flow motion is directed inboard and connected with the local induction effect of the blade loads, *i.e.,* it is related to flow separation. In the normal force distribution presented in Figure 4.6c, roughly representing the bound circulation, it is shown that the force locally decreases at the aforementioned locations causing a local change of the bound vortex direction and induction effect.

Figure 4.16 shows the velocity distribution extracted from Figures 4.12, 4.13 and 4.14 for $\theta = 0°$. It can be seen that the axial velocity increases up to around $1.075U_\infty$ at the edge of the blade root at $r/R = 0.12$ and around $1.01U_\infty$ in the near tip region. It is interesting to note that the axial velocity increase near the root is even higher than near the tip region. In the blade middle stations, between $0.2 < r/R < 0.8$, the magnitude of this velocity component reduces as it enters the wake region. This indicates that the axial flow component is less reduced near the blade, which may be related to the displacement effect. For the circumferential velocity component in Figure 4.16b, V_θ increases significantly around the blade and the influence becomes smaller for larger X/R, which clearly indicates that the effect is caused by the fluid flow around the blade due to displacement effect. Interestingly, it seems that the circumferential velocity augmentation becomes stronger approaching the center of rotation along the blade. The velocity suddenly drops at $r/R = 0.12$ where the edge of the blade root is located. In contrast, the radial flow increases significantly at this area shown in Figure 4.16c. The increased circumferential velocity component is in good agreement with the increased suction peak with decreasing blade radius as the angle of attack becomes larger. The pressure distributions for different blade stations can be seen in Figure 4.19 in Section 4.4. Unlike the axial and circumferential velocities, no considerable change

of the radial velocity component is observed along the blade, especially further away from the rotor plane. This confirms preceding studies of the 3D effects that the strong radial flow is only prominent within the separated boundary layer area.

Figure 4.17 presents the spanwise flow (v_z) in the rotating frame of reference, *i.e.,* the rotational speed of the blade (Ω) is taken into account, at several radial positions, namely $0.25R$, $0.35R$, $0.6R$, $0.82R$ and $0.92R$. This flow component is the same as V_r only at $\theta = 0°$. The term v_z is presented instead of V_r because the spanwise flow defines the chordwise component of the Coriolis force that is important for separation delay. The velocity component is non-dimensionalized by the local kinematic velocity. The red domains in Figure 4.17 represent the regions characterized by a strong spanwise flow. The spanwise velocity on the pressure side is small compared to the kinematic

(a) Axial component.

(b) Circumferential component.
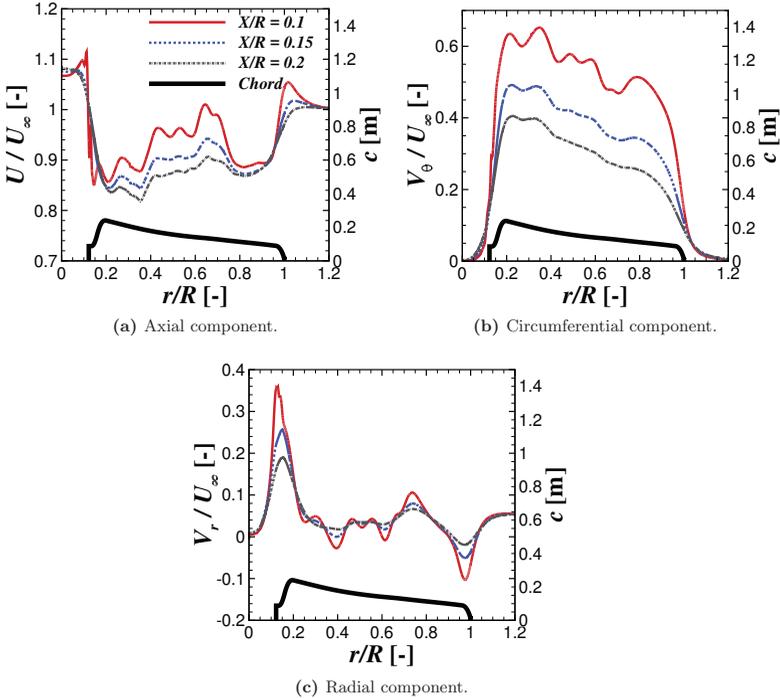
(c) Radial component.

Figure 4.16: Dimensionless velocity components for $\theta = 0°$ at several axial distances, $X/R = 0.1$, 0.15 and 0.2. *Figure is taken from [146].*

(a) $c/r = 0.4$.

(b) $c/r = 0.24$.

(c) $c/r = 0.1$.

(d) $c/r = 0.06$.

(e) $c/r = 0.05$.
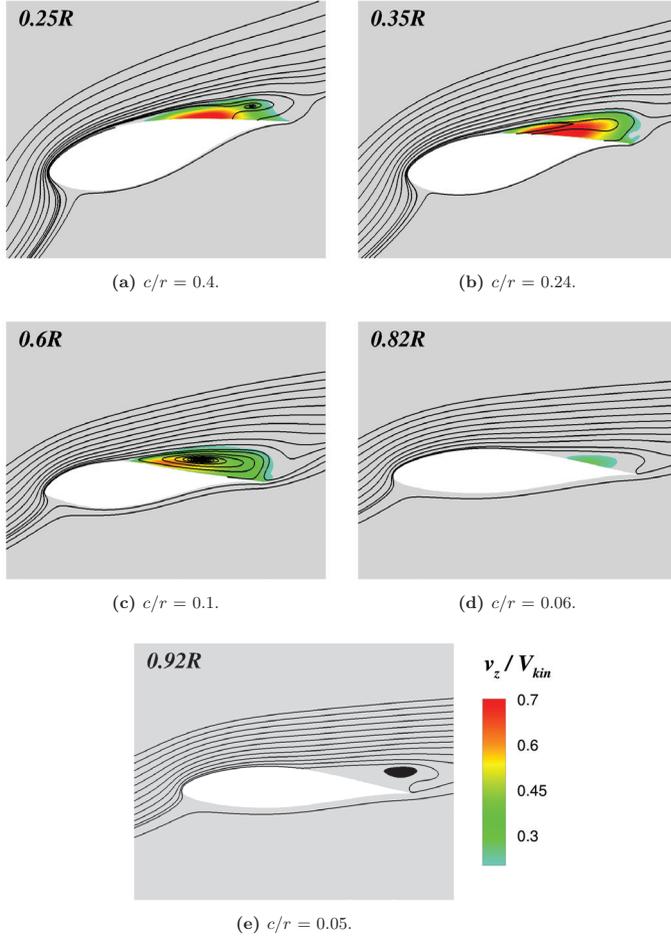
Figure 4.17: Time averaged dimensionless spanwise velocity in rotating frame of reference (v_z) at several radial stations, $r/R = 0.25, 0.35, 0.6, 0.82$ and 0.92. The contour level below than 0.2 is omitted for clarity purpose. *Figures 4.17b-4.17e are taken from [146].*

77

velocity. Furthermore, the flow is attached on the pressure side of the blade. On the other hand, it can be seen that the spanwise flow is remarkable on the blade suction side where separation occurs especially in the inboard area. It extends up to r/R = 0.6 but the magnitude significantly reduces even though the nature of the flow is massively separated, indicating that the spanwise flow is less dominant for $c/r \leqslant 0.1$. By means of this information, the 3D correction of the 2D polar for engineering codes like BEM can be applied for $c/r \geqslant 0.1$, and pure 2D polars can be used in the other region. Additionally, it is noted that the spanwise flow occurs only within the separated boundary layer supporting the studies for the 3D effects [1–4, 27, 29, 57].

4.4   3D Effects on Aerodynamic Coefficients

In this section, the influence of the 3D effects on the aerodynamic coefficients is discussed. Firstly, the angle of attack was extracted from the DDES results using the reduced axial velocity method [60, 126, 127] described in Section 2.4. Then, the resulting angle of attack was used to calculate the lift (C_L) and drag (C_D) coefficients from the CFD simulations, defined as:

$$C_L \; = \frac{L}{0.5 \, \rho \, V_{rel}^2 \, c} \quad \text{and} \quad C_D = \frac{D}{0.5 \, \rho \, V_{rel}^2 \, c}, \qquad (4.2)$$

where L and D are the lift and drag forces, respectively, and V_{rel} is the relative velocity including the induction effect. There is no information of α in the new MEXICO measurements [119]. Thus, the same angle of attack (as the extracted CFD results) was assumed to calculate C_L and C_D for the experimental data.

To demonstrate the 3D effects, the 3D rotating blade results need to be compared to the 2D data with consistent inflow conditions like the angle of attack and Reynolds number. For this purpose, two-dimensional simulations of the blade sections were performed. In these computations, the same angle of attack and Reynolds number as the 3D rotor were applied. The 2D simulations make use of the URANS approach employing the Menter SST [102] turbulence model. The DDES approach is not applied for the 2D case due to the 3D nature of the eddies. Similar to the 3D rotor computations, no laminar-turbulent transition was considered.

It shall be noted that two-dimensional measurement data for airfoils constructing the MEXICO rotor is available, documented in Ref. [153]. Despite that, it is worthwhile to emphasize that the 3D rotor blade operates at different Re than the 2D experiment. Furthermore, boundary layer tripping was applied in the 2D measurement while the 3D rotor simulations assume a fully turbulent flow. This indicates that there may be uncertainty induced if the 3D rotor results are directly compared to the 2D experimental data. In order to asses the accuracy of 2D CFD simulations, additional two-dimensional simulations of these airfoils were performed at consistent inflow conditions as in the experiment.

To sum up, in total, five different cases are employed in the present studies to assess the three-dimensional effects:

- **3D Exp.**: *3D experiment* obtained from Ref. [119].

- **2D Exp.**: *2D experiment* obtained from Ref. [153].

- **3D DDES**: *3D rotor simulations* employing the DDES-SST turbulence model.

- **2D URANS-A**: *2D rotor computations* employing the URANS-SST turbulence model at the same inflow conditions as the *3D rotor simulations*.

- **2D URANS-B**: *2D rotor computations* employing the URANS-SST turbulence model at the same inflow conditions as the *2D experiment*.

Details of the inflow conditions employed can be seen in Table 4.2. The angle of attack shown is obtained from the analysis described in the preceding paragraph. In the following paragraphs, it shall be noted that the 2D CFD accuracy is assessed by comparing *2D URANS-B* to *2D Exp.*, 3D CFD accuracy by comparing *3D DDES* to *3D Exp.*, and the three-dimensional effects are evaluated by comparing *3D DDES/3D Exp.* to *2D URANS-A/2D Exp.*.

Figure 4.18 presents the C_L and C_D distributions along the blade radius. In the most inboard position, at $r/R = 0.25$, the 2D and 3D CFD simulations accurately predict the measured aerodynamic coefficients, except for 2D C_D where the data is overestimated. It is clearly shown that the 3D effects cause C_L augmentation up to 2 times compared to the 2D situation. In Figure 4.19a, it can be seen that the distribution of C_p at $r/R = 0.25$ agrees well with the behaviour of C_L in Figure 4.18. The suction peak of C_p remarkably enhances from -4.8 in the 2D case to -8.85 in the 3D case, but

Table 4.2: Employed *Re* and α for the 2D and 3D cases. SS represents the suction side and PS is for the pressure side. The angle of attack is obtained from the 3D rotor computations employing the RAV approach [60, 126, 127].

r/R [-]	Airfoil	Re [-]	α [°]	Tripping [-]
		2D Experiment		
$0.25R$	DU91-W2-250	0.7×10^6	22.8	0.05 (SS) and 0.1 (PS)
$0.35R$	DU91-W2-250	0.7×10^6	19.7	0.05 (SS) and 0.1 (PS)
$0.6R$	RISØ-A1-21	1.6×10^6	16.9	0.05 (SS) and 0.1 (PS)
$0.82R$	NACA 64-418	0.7×10^6	13.8	0.05 (SS) and 0.1 (PS)
$0.82R$	NACA 64-418	0.7×10^6	13.7	0.05 (SS) and 0.1 (PS)
		3D Rotor Simulations		
$0.25R$	DU91-W2-250	0.50×10^6	22.8	fully turbulent
$0.35R$	DU91-W2-250	0.54×10^6	19.7	fully turbulent
$0.6R$	RISØ-A1-21	0.61×10^6	16.9	fully turbulent
$0.82R$	NACA 64-418	0.64×10^6	13.8	fully turbulent
$0.82R$	NACA 64-418	0.62×10^6	13.7	fully turbulent
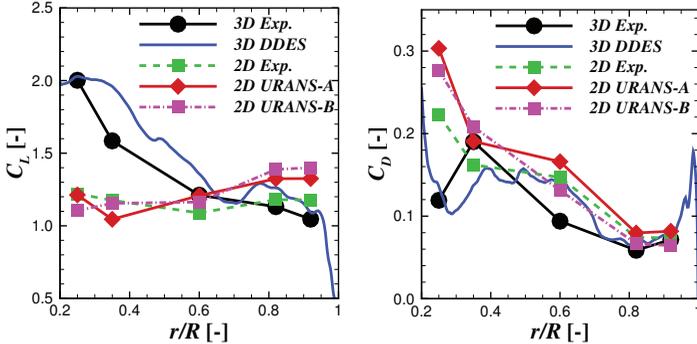
Figure 4.18: Lift (left) and drag (right) coefficients along the blade radius from the time averaged CFD results and experiments. Lift increases in the blade inner part while drag decreases. *Measurement data for the 3D and 2D cases are obtained from [119] and [153], respectively.*

reduces compared to the 2D inviscid C_p level of -17.65. This effect is caused by the delay of separation from $x/c \approx 0.2$ in the 2D case to $x/c \approx 0.4$ in the 3D case, which stems from mixed influences of the inviscid and viscous rotational effects described in Chapter 3. It worthwhile to mention again that the inviscid effect tends to reduce the suction peak and, consequently, the pressure gradient due to the influence of the root vortices. In contrast, the root vortices become weaker if the viscous effect is considered, and, as the radial flow presents, the Himmelskamp effect takes place delaying the occurrence of separation. However, it was shown in Chapter 3 that the pressure distributions for both the inviscid and the viscous cases do not much differ, indicating that the viscous rotational effect is driven by the inviscid characteristics of the blade. It is suggested to refer back to Chapter 3 for detailed discussion of the phenomena.

It is shown, at $r/R = 0.25$, that the 3D CFD results are similar to the measurement data although the nacelle was not modelled in CFD, see Figure 4.18. This may indicate that the root vortices have weaker influence to the 3D effects than the observation made in Chapter 3 despite the fact that a distinct hub vortex is observed in Figure 4.15. The reason seems to be related to the airfoil thickness. In the MEXICO rotor, the inboard region employs the DU91-W2-250 airfoil (25% relative thickness) which is characterized by trailing edge separation. This is in contrast to the NACA 0010 airfoil (10% relative thickness) employed in Chapter 3 which shows leading edge separation. Furthermore, the cylindrical portion of the most inboard blade area reduces the tendency of the distinct root vortex in affecting the blade sections further outboard.

A similar behaviour is shown at a larger radial position at $r/R = 0.35$. Surprisingly, the 2D URANS computations accurately predict 2D C_L in the inboard region even
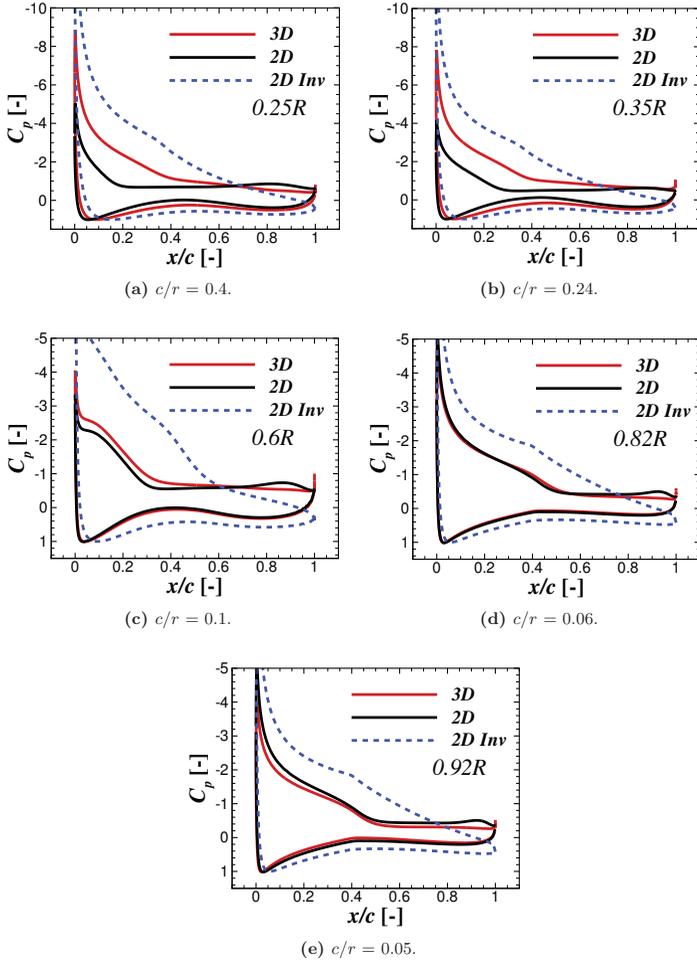
Figure 4.19: Time averaged C_p distributions of the blade section and 2D airfoil data for several radial stations obtained from *3D DDES* and *2D URANS-A*, respectively.

though the angle of attack is large involving massive flow separation, *e.g.,* at $r/R = 0.25$ the angle of attack is 22.8°. However, in the 3D CFD results, it can be seen

that C_L is overpredicted and C_D is underpredicted. This agrees with the behaviour for the prediction of F_y presented in Section 4.2. It was documented by Weihing et al. [78] that a proper modelling of the hub-nacelle geometry can fix the issue. Thus, it is quite reasonable to expect the cause of the phenomena based on the influence of the root vortex induction effect. Despite that, this shall not be confused with the root vortex influence for the inviscid flows described above. It was documented in Chapter 3 that the roll-up motion of the root vortex causes the vortex-induced centrifugal force which produce streamtube widening and reduces the suction peak. In this particular radial station, the root vortex creates the induction effect, which increases the local wind speed and, consequently, the local angle of attack perceived by the blade section. Furthermore, it is shown in Figure 4.17b that the relative spanwise flow component is stronger compared to the smaller radial station of $0.25R$, which seems strange because the values of α and c/r are smaller than those at $0.25R$. It is expected that the root vortices are responsible for this. As a consequence, the Himmelskamp effect within the blade boundary layer is overestimated and the rotational augmentation becomes stronger.

The enhancement of lift is observed up to $r/R = 0.6$, corresponding to the c/r ratio of 0.1 which is defined as the limit where the 3D effects are prominent in Chapter 3 and Section 4.3. These are observed in both the measurement data and the CFD simulations with good agreement. It is interesting to note that 3D C_L is comparable to the 2D case in the middle blade regions, namely at $0.6R$ and $0.82R$, even though strong separation occurs, see Figure 4.17. It shows that as long as v_z/V_{kin} is small, the airfoil section generally behaves like in the two-dimensional situation.

Particularly at $r/R = 0.6$, the locations of separation in the 2D and 3D cases are similar (Figure 4.19c), but the 3D lift coefficient in Figure 4.18 and the suction peak value in Figure 4.19c for the corresponding section are slightly higher than in the 2D case. The small lift augmentation is likely to be caused by the reduced pressure effect rather than the separation delay for this particular section. The centrifugal force seems to be responsible for this effect since the main mechanism of this force is on the boundary layer thinning. Similarly, Sicot *et al.* [154] also observed a lift enhancement for a small turbine rotor without the evidence of separation delay.

In the near tip region, the 3D DDES computations also deliver accurate results compared to the measurement data. On the other hand, the 2D URANS results for the outboard NACA 64-418 airfoil at $r/R = 0.82$ and 0.92 clearly overestimate the lift coefficient, but are accurate for the drag coefficient. It is already well known that URANS often inaccurately predicts the maximum lift coefficient of airfoils [68, 69, 104, 147, 155]. Considering the maximum lift for this airfoil is at $\alpha = 15°$, C_L overestimations for the radial stations of 82% and 92% become reasonable, because the airfoil sections operate at $\alpha = 13.8°$ and $13.7°$, respectively. Note that the 2D prediction for the inboard airfoil (DU91-W2-250) has a better agreement with the experimental data although the angle of attack is significantly larger. This discrepancy can be attributed to the airfoil-type (Table 4.2) dependency influence. Furthermore, it will be shown in Chapter 5 - Figure 5.6a (for different Re) that the prediction of the DU91-W2-250

airfoil is actually also inaccurate near the maximum lift coefficient but the accuracy increases with increasing angle of attack in the post-stall regime.

It is shown that the 3D lift coefficient decreases below the 2D condition in the near tip region. The reduced lift effect near the tip is expected to arise from two major causes: (1) inaccuracy of the α extraction and (2) tip loss effects. Considering the fact that the evaluation is not too close to the tip area with a strong wake expansion effect, the use of the averaged α method [60, 126, 127] seems to be plausible and the second reason is likely to be more dominant. This is similar to the studies carried out in [67]. Furthermore, the same situation is also observed in the experimental data. In addition, the total area of 3D C_p in the outer blade region is smaller than for the 2D case, resulting in the smaller C_L magnitude. It is shown that both 2D and 3D results show similar suction peaks, indicating that the 3D root effects are negligible in these areas.

The general observation of the C_D behaviour in Figure 4.18 indicates that rotation seems to have weaker influence on the drag coefficient compared to the lift, but C_D is generally reduced by the rotation. Apart from the uncertainty in the angle of attack extraction, the drag alleviation is connected with the behaviour of the separated boundary layer. It is observed in the present studies that the separation area becomes smaller for the rotating blade boundary layer. This observation is supported by Du and Selig [30, 31], Bangga *et. al.* [56, 57, 67] and Chaviaropoulos and Hansen [29]. Hence, it naturally contributes to the drag reduction. The drag coefficient reduction was also observed for the 10 MW AVATAR rotor [67]. Despite that, Chaviaropoulos and Hansen [29] in their 3D correction assumed the drag to increase contradicting the present observations. The drag increase was also observed in the results from the NREL UAE Phase VI wind turbine [52, 60]. Himmelskamp [3] and Lindenburg [156] argued this by stating that energy is required to pump the separated flow outboard which results in the drag augmentation.

4.5   Summary

Investigations of the three-dimensional flow occurring on the isolated MEXICO rotor blade have been carried out and discussed in the preceding sections. The rotor operates at a small tip speed ratio of 4.2 and at a high wind speed of 24 m/s. The pitch angle is -2.3°. The rotor is characterized by massive flow separation for the whole blade radius.

The simulations were carried out using the Delayed Detached-Eddy Simulation (DDES) approach. Initially, the computations were run for 7 rotor revolutions until the wake is fully developed. Then, one additional rotor revolution was simulated from the restart point for data extraction purpose, which is sufficient for computing the mean flow properties. Two different near wall RANS models were examined, the Menter SST and Spalart-Allmaras turbulence models. It was shown that the DDES-SST model gives better prediction of the aerodynamic forces along the blade than the DDES-SA approach. The C-H mesh topology resolves finer flow structures than the O mesh topology. This is particularly true because the C-H mesh contains an additional wake

block mesh. Despite that, the computational cost is larger as a consequence.

It was shown that the relative rotor axial flow component (U/U_∞) increases considerably around the center of rotation because no hub was modelled in the simulations. The relative magnitude is even larger than the axial velocity near the tip area. Despite that, the influence of this "nozzle-like" flow is not so significant for the axial flow distribution along the blade. Negative magnitude of the relative rotor circumferential flow component (V_θ/U_∞) was observed on the blade pressure side. Despite that, in contrary, V_θ/U_∞ becomes more positive on the blade suction side area. Downstream of the rotor, the magnitude of the circumferential flow is generally positive, indicating that the inviscid part of the flow field rotates opposite to the rotor. Both the relative rotor circumferential and the radial flow (V_r/U_∞) components illustrate the position of the root vortices, indicated by the change of sign of the velocity components. It was shown that a distinct root vortex near the blade-root-end area occurs for the isolated rotor. The vortex travels downstream in helical fashion similar to the tip vortex.

The 3D rotational augmentation effects were observed in the present studies. The 3D lift coefficient (C_L) in the blade inboard region increases compared to its corresponding 2D conditions. The augmentation extends up to the region where the ratio of chord to radius (c/r) equal to 0.1. Even though massive flow separation occurs for the whole blade, the rotational augmentation happens only if the relative kinematic spanwise flow (v_z/V_{kin}) is strong, and this corresponds to $c/r > 0.1$. Therefore, it is suggested to apply 3D corrections for the engineering models only in the inboard blade region up to $c/r = 0.1$. In the present studies, the drag coefficient (C_D) is less affected by the rotation compared to lift. However, 3D C_D generally is smaller than in the 2D situations. The effect is expected to stem from separation delay in the 3D conditions.

In connection to the inviscid-viscous rotational effects, the importance of root vortices has been evaluated in the present studies. The suction peak of the 3D rotor increases compared to the 2D viscous case, causing lift augmentation, but reduces compared to the 2D inviscid data. The effect originates from the mixed influences of the inviscid and viscous effects. It was shown that the root vortices have weaker influence on the pressure distribution than the generic blade consisting of the thin NACA airfoil. This seems to be related to differences in the airfoil thickness and in the separation characteristics. Furthermore, the extreme root area ($r/R < 0.15$) of the MEXICO blade consist of cylindrical shape and the radial expansion of the most inboard root vortices is weak. In addition, an overestimation of the measured lift coefficient was observed at $0.35R$. This is caused by the induction effect of the root vortices that increases the wind speed and the local angle of attack perceived by the blade section. It was documented that this generates a stronger radial flow, resulting in the overestimation of the Himmelskamp effect within the separated flow area.

Chapter 5

3D Flow on the AVATAR Rotor

This chapter is constructed based on the following articles:

- *G. Bangga, T. Lutz, E. Jost and E. Krämer, CFD studies on rotational augmentation at the inboard sections of a 10 MW wind turbine rotor, Journal of Renewable and Sustainable Energy 9(2), 023304, 2017. American Institute of Physics.*

- *G. Bangga, P. Weihing, T. Lutz and E. Krämer, Hybrid RANS/LES simulations of the three dimensional flow at root region of a 10 MW wind turbine rotor, New Results in Numerical and Experimental Fluid Mechanics XI. Notes on Numerical Fluid Mechanics and Multidisciplinary Design, vol 136. Springer.*

To meet the energy demand from wind power sources, the size of wind turbine rotor is increased nowadays to generate more electricity. This enforces blade designers to adopt much thicker airfoils in the inboard area of the rotor, extending farther outboard compared to the conventional smaller machines, to obtain the necessary structural stability. Furthermore, the increased size leads the turbine to operate at significantly higher Reynolds number. There are still open questions regarding the 3D effects under these situations, particularly when thick airfoils are employed in the root area. As already presented in Chapters 3 and 4, viscous rotational effects are driven by flow separation. This implies that the use of abundantly thick airfoils, which are prone to massive separation, may contribute to the 3D effects. In the present chapter, this aspect is evaluated for a generic 10 MW wind turbine rotor. The chapter is organized as follows: The description of the blade, test cases and numerical methods are described in Section 5.1. Section 5.2 presents the verification of the CFD simulations. In Section 5.3, consistency of the employed α extraction method is evaluated. The three-dimensional effects are discussed in Sections 5.4-5.7. The evaluations are focused on the viscous rotational effects occurring on the rotor, putting an emphasis on the influence of the Coriolis and centrifugal forces.

5.1 Test Case and Computational Setup

For the present studies, the generic 10 MW AVATAR blade [120, 121] was chosen. The rotor is designed based on the DTU 10 MW wind turbine [122] with a larger blade radius of $R = 102.9$ m. Uniform wind speeds (U_∞) ranging from 5 m/s to 25 m/s were considered for the CFD simulations of the rotor. The chosen rated wind speed for this turbine is 10.75 m/s. The rotational speed and the pitch angle were kept constant at 9.02 rpm ($\Omega \approx 0.94$ rad/s) and 0.0°, respectively, in order to obtain different angles of attack (α) seen by the blade sections with the variation of the wind speeds. The present operating condition was selected not according to the original designated blade operation [121]. This was purposely done to artifically generate massive separation, where the 3D effects are strongly associated with, and to study the impact of the Rossby number, defined as

$$Ro = \frac{\left(U_\infty^2 + (\Omega r)^2\right)^{0.5}}{\Omega c},\tag{5.1}$$

where r and c represent the local blade radius and airfoil chord length, respectively. The calculations were performed without tower to isolate the rotational augmentation from unsteady tower disturbances. A similar coordinate system as described for the MEXICO rotor in Chapter 4 was adopted in these studies, where the details are illustrated in Figure 2.4 and 5.2. In the rotating (local) coordinate system, x,y and z represent chordwise, normal and spanwise directions of the blade which rotate together with the rotor.

As described in Chapter 2, the FLOWer code [74–76] was used to numerically model the fluid flow over the rotor by solving the Navier-Stokes equations on the structured meshes. Unless stated otherwise, a central scheme based on the Jameson-Schmidt-Turkel (JST) formulation was employed for flux discretization, resulting in a second order accuracy on smooth meshes. For turbulent closure, the two-equation shear stress transport (SST) $k - \omega$ model according to Menter [102] was used. In the present analysis, fully turbulent computations were carried out for the 3D rotor, either as URANS or DDES, and 2D airfoils constructing the AVATAR blade to demonstrate the 3D effects. The simulations were performed with the time step size of 0.037 s which corresponds to two degree blade revolution per physical time step. The time step can be calculated as $\Delta t[s] = \Delta t[°]/(\Omega 360°)$, where $\Delta t[°]$ is the azimuthal time step size. The basic sensitivity to temporal resolution will be demonstrated in Section 5.2.2. Each physical time step was iterated towards a pseudo steady state using 35 sub-iterations, similar to the strategy used for the new MEXICO rotor simulations.

First, 2D structured grids of the airfoil geometries constructing the AVATAR blade were generated in order to study the grid dependency of the numerical results in 2D, which will be shown in Section 5.2.1. The airfoils at three different radial positions namely $0.25R$, $0.35R$ and $0.6R$ were chosen. In these studies, it will be shown that the grid of 280 x 128 cells in chordwise and normal directions, respectively, with 32 cells across the boundary layer sufficiently predicts the resulting forces of the 2D airfoils.
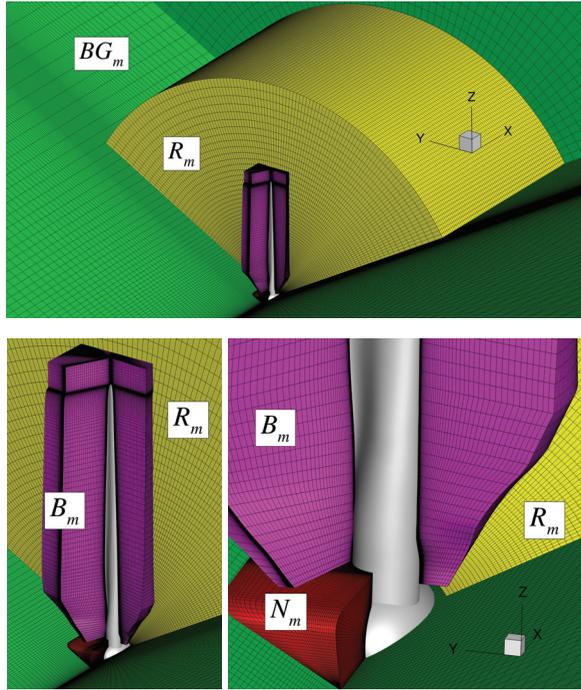
Figure 5.1: Grid setup showing blade (purple); spinner and nacelle (red); refinement (yellow) and background grids (green). Variables X, Y and Z represent coordinate system in the inertial frame of reference. *Figure is taken from [67].*

The distance of the first cell to the airfoil wall was set according to non-dimensional wall distance of y^+ less than unity.

The grid for the rotor simulations consist of several components, background (BG_m), wake refinement (R_m), blade (B_m) and nacelle (N_m) meshes as shown in Figure 5.1. Information obtained from the 2D grid studies was applied to the 3D mesh generation, *i.e.,* the blade mesh consists of 280x128 cells in chordwise and normal directions, respectively. The blade is discretized by 192 cells along the radius with significant refinement near the root area. Figure 5.2 shows the surface meshes and the sectional mesh of the blade used in the present investigations. The sensitivity of the CFD computations towards the blade grid resolutions will be presented in Section 5.2.2. The mesh of the blade is C-H type and was constructed using the commercial grid generator Gridgen with the "automesh" script [84] developed at the IAG. The 3D blade mesh quality is maintained as in the 2D grid with $y^+ < 1$.
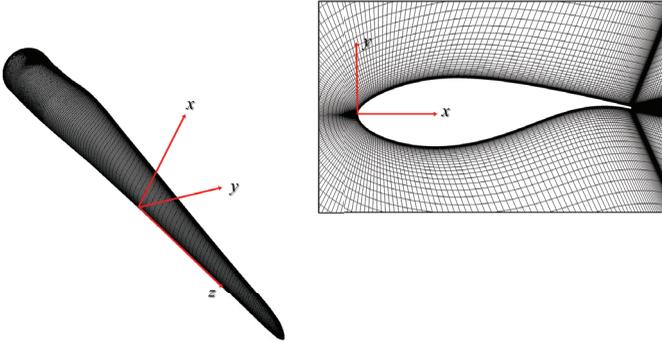
Figure 5.2: Surface mesh and detailed cross-section mesh of the blade. Variables x, y and z represent local coordinate of the blade section in the rotating frame of reference. *Figure is taken from [67].*
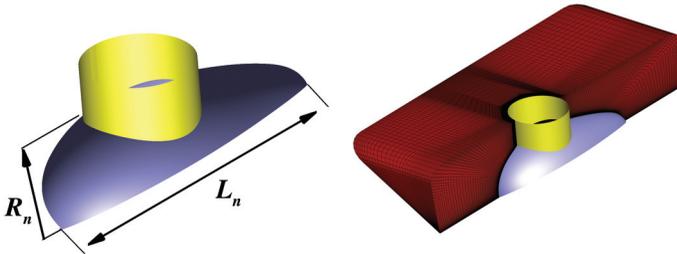
Figure 5.3: Nacelle shape and its computational mesh. The nacelle is indicated by purple color and blade-hub connector by yellow. Variables R_n and L_n indicate the nacelle radius and length, respectively.

In contrast to the simulations for the MEXICO rotor in Chapter 4 which assume an isolated rotor, the present works employ a proper connection of the rotor-junction. The shape of the rotor nacelle was not specifically defined in the AVATAR project [120, 121]. Thus, a generic nacelle with an elliptical shape, allowing a more streamlined hub flow, is used in the studies to reduce the unsteadiness and to better isolate the 3D effects. The mesh of the nacelle was generated using an automatic script developed at the institute for this specific nacelle type, allowing the user to easily change the mesh parameters while maintaining the quality of the resulting grid. Figure 5.3 shows the

shape of the employed nacelle in these studies. The nacelle/hub (purple colored) is joined by a connector with cylindrical shape (yellow colored) extending up to $r = 6$ m. The nacelle radius (R_n) and length (L_n) are 4 m and 16 m, respectively, corresponding to $R_n/R = 0.039$ and $L_n/R = 0.156$. R represents the blade radius of 102.9 m. The nacelle was discretized by 192 cells along L_n and 80 cells in circumferential direction. Again, 32 cells are located within boundary layer with $y^+ < 1$.

The meshes for the other structures were constructed by hand using Pointwise. The cell size of the wake refinement mesh (R_m) is 1 m in streamwise direction (X), corresponding to $\Delta/R = 0.01$. This resolution was chosen according to the study by Kim *et al.* [59] who observed that the vortex development and wake mixing downstream of the AVATAR rotor are sufficiently captured by employing this resolution. In crossflow direction, Z, the wake mesh was refined near the center of rotation as the main focus of the present works is in the blade inboard region, resulting in the grid spacing of $\Delta/R = 0.0034$ around the blade root and $\Delta/R = 0.01$ near the tip. In circumferential direction (θ), 305 grid points were used along 120° of the grid domain, resulting in $\Delta/R = 0.00023$ and 0.01 around the root and tip areas, respectively.

All the meshes were built 120-degrees symmetry of the wind turbine rotor by modelling only one blade, assuming flow periodicity using the periodic boundary condition. The background domain is a 1/3 cylinder containing the periodic symmetrical planes, while the farfield boundary condition was set on the other sides. All the structures rotate together around the center of rotation. A uniform inflow condition was imposed at the farfield boundaries. The computational domain size was set to 2000 m x 2000 m in streamwise (X) and crossflow (Z) directions. The meshes were built separately and combined together without sacrificing the quality of the meshes by applying the Chimera overlapping grid technique.

5.2 Verification of the Numerical Schemes

5.2.1 2D Airfoil Simulations

For the 2D airfoil simulations, a grid study was performed in order to show that grid independence is achieved with the chosen grid. Three different grid densities along the airfoil circumferential direction were examined; Grid 1: 200 cells, Grid 2: 280 cells, Grid 3: 360 cells. The studies were performed for three different sections of the AVATAR rotor [120], namely $r/R = 0.25$, 0.35 and 0.6. Table 5.1 presents the distribution of the Reynolds and Mach numbers for which the simulations were undertaken as well as the geometrical properties of the airfoil. It shall be noted that the airfoil shape presented in Table 5.1 is interpolated to the corresponding radial position based on the DU airfoils (Table 2.2) constructing the blade. In the 2D simulations, the calculations of Re and Ma were carried out using the kinematic velocity for the corresponding radial station. The closure of the URANS model uses the Menter SST [102] without employing any laminar-turbulent transition model. The time step size for the present 2D simulations is 0.00035 s, corresponding to 0.15% of the convective time of a fluid particle passing

Table 5.1: Employed Re and α for different radial stations along the blade for the test case of $U_\infty = 10.5$ m/s. Variables β and t/c represent the twist angle and relative airfoil thickness, respectively.

r/R [-]	Re [-]	Ma [-]	c [m]	β [°]	t/c [-]
0.10	5.4×10^6	0.042	5.533	16.64	0.94
0.15	7.1×10^6	0.053	5.775	16.64	0.75
0.20	9.2×10^6	0.065	6.105	15.16	0.57
0.25	11.3×10^6	0.078	6.223	13.02	0.46
0.35	14.2×10^6	0.105	5.832	8.87	0.36
0.60	17.6×10^6	0.174	4.340	5.85	0.25
0.80	16.8×10^6	0.231	3.134	4.22	0.24
0.95	14.2×10^6	0.273	2.225	3.43	0.24

the airfoil.

The results of the simulations are presented in Fig. 5.4 in terms of lift, drag and moment coefficients. The center of the aerodynamic moment is located at $0.25c$ from the leading edge. It is shown that the increased grid resolutions hardly produce any difference in all the examined aerodynamic coefficients for a large range of α, inferring that the grid is spatially converged, especially as the the grid resolution increases from Grid 2 to Grid 3. All the grid resolutions generally are in a good agreement within the linear region but Grid 1 slightly underpredicts the results in the post stall regime, similarly also for the negative stall angle. Thus, in all further simulations, Grid 2 with the streamwise resolution of 280 cells is used.

To examine the dependency of CFD results upon temporal resolution, 2D simulations were also carried out for various time step sizes. In Figure 5.5, the results are presented in terms C_L, C_D and C_M. The moment reference point is at quarter chord distance from the leading edge. It can be seen that that the aerodynamic coefficients for the airfoil at 25% radial section (at $\alpha = 14°$) show little dependency upon the time step size used. A similar behaviour was observed also for the other airfoils. Thus, the time step size of 0.00035 s is chosen for the 2D CFD simulations.

In confirming the accuracy of the 2D computations for simulating thick airfoils, the results need to be validated against experimental data. However, the measurement data for the DU airfoils constructing the AVATAR rotor is only available at Re of 3 million [157] which is smaller than the actual rotor operation displayed in Table 5.1. Contrasting the above fully turbulent computations, the experiment was performed by considering boundary layer tripping. Thus, a direct comparison between the results are not possible due to differences in the inflow and transition conditions. Furthermore, the above simulations were performed on the interpolated airfoil shapes that may lead to uncertainty. On this basis, additional 2D CFD computations for the DU airfoils (Table 2.2) need to be carried out at the same inflow and transition conditions as the experiment [157].

In Figure 5.6, results of the 2D unsteady CFD simulations are compared with the
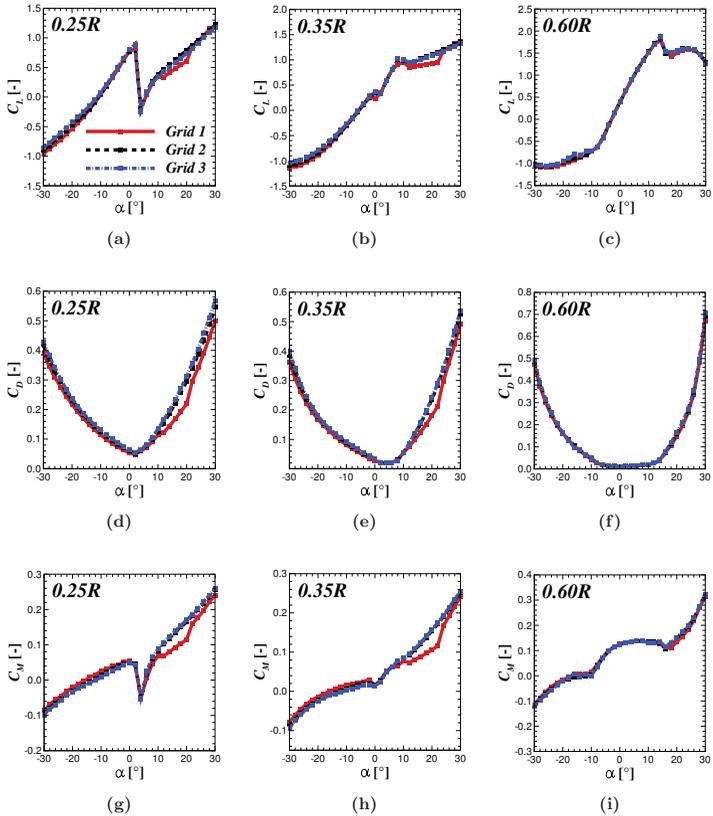
Figure 5.4: Impact of grid density on the 2D prediction of airfoil sections.

measurement data obtained from Rooij and Timmer [157]. The presented thick aerodynamic profiles are the airfoils constructing the AVATAR blade as shown in Table 2.2. The Reynolds number used in the experiment and in the CFD computations is $3.0e6$. The measurements were conducted for tripped conditions and detailed informations of the trip locations are given in Figure 5.6. SS and PS represent the suction and pressure sides, respectively. The transition was prescribed at turbulator position, *i.e.,* turbulence production was switched on at this location.
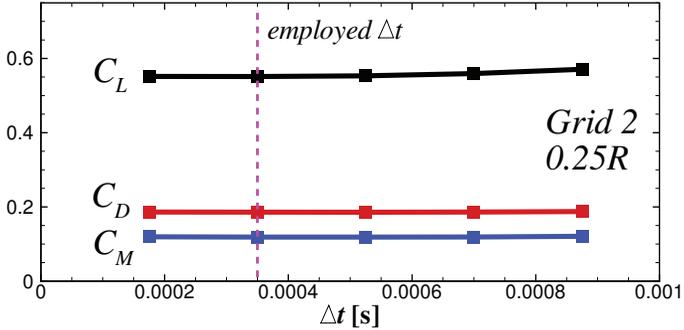
Figure 5.5: The effect of temporal discretization on the predicted aerodynamic coefficients. The simulations were carried out for the airfoil section of 0.25R, at $\alpha = 14°$ and $Re = 11.3\text{x}10^6$.

For the DU 91-W2-250 airfoil, in the experiment, the boundary layer tripping was introduced only on the suction side at $x/c = 5\%$ while natural transition occurred on the pressure side. Thus, the transition location on the pressure side was estimated using XFOIL [158] for each angle of attack, resulting in 20 different transition location data. In this prediction, the critical n-factor was set to 9 that corresponds to 0.070% turbulence level. The experiment was carried out in the low-turbulence tunnel having a turbulence level well below 0.1% [157]. For the airfoil with 30% relative thickness, DU 97-W300, boundary layer tripping was applied for both airfoil sides at $x/c = 5\%$ and 20% on the suction and pressure side, respectively. The same transition locations were applied in the CFD simulations. For the thicker airfoils, DU 00-W2-350 and DU 00-W2-401, the relative thicknesses are 35% and 40%, respectively. The turbulator was prescribed at $x/c = 2\%$ (suction side) and 10% (pressure side) on both airfoils. In addition to that, CFD computations for fully turbulent boundary layer were also performed for comparison. The transition location has an influence on the laminar or turbulent separation. As the size of separation has a strong impact on the 3D effects, it is important to have a clearly defined condition. For instance, it is shown in Figure 5.6 that the simulations with prescribed transition predict very similar results as for the fully turbulent case for all studied airfoils within the linear lift region. This happens because the tripping location on the suction side is close to the leading edge ($\leq 5\%$). However, in the stall region, the tripping affects the attained maximum lift and stall angle, especially in Figures 5.6a and 5.6b where the transition on the suction side is located at $x/c = 5\%$.

Figure 5.6a shows the C_L polar for the DU 91-W2-250 airfoil with 25% relative thickness. This airfoil is located at the outer sections of the AVATAR blade. A very good agreement of the present simulations compared to the experiment is achieved for
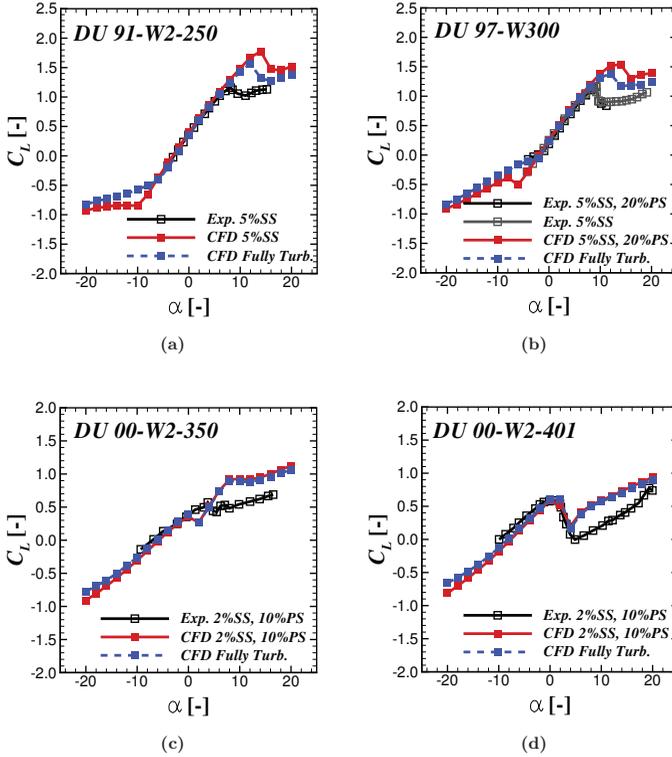
Figure 5.6: Comparison of the 2D CFD simulations with measurement data obtained from [157]. The calculations and measurements are conducted at $Re = 3.0e6$. SS and PS indicate the suction and pressure sides, respectively. *Figure is taken from [67].*

the linear lift region but the maximum lift coefficient and the stall angle are overpredicted in both, the fully turbulent and tripped computations. Figure 5.6b shows the prediction for the DU 97-W300 airfoil. The predicted C_L almost coincides with the measurements for the linear region; but similar to the thinner airfoil, the CFD simulation hardly predicts the stall accurately. Inaccurate results are shown for the nonlinear C_L in the post stall regime. However, the general behaviour of the C_L polar is reasonably captured using the 2D URANS computations. A greater challenge comes for the calculation of the thicker airfoils in Figures 5.6c and 5.6d where the polars show strong non-linearities and a very sharp change of C_L gradient is shown

especially for the DU 00-W2-401 with the relative thickness of 40%. Despite that, the CFD simulations can capture the general behaviour of the polar, and the stall angle of the DU 00-W2-401 is even accurately predicted although the undershoot is not correctly captured. It shall be noted that for these airfoils, flow separation occurs already at small angles of attack (even at $\alpha = 0$) on the pressure side. This makes the CFD predictions of the lift polar delicate as shown in Figure 5.6c.

The inaccuracy of the CFD predictions within the stall region could be expected as the simulations employ the URANS method. The simple two-equation eddy viscosity turbulence models often gave inaccurate results of the airfoil in stalled conditions [68, 69, 104, 155]. Furthermore, simulations are in two-dimensional configuration and no eddies are resolved, but modeled. Therefore, the choice of the turbulence model can add to the variability of the predicted maximum lift [147]. One possibility to improve the 2D URANS predictions is through the adjustment of some parameters in the turbulence model as suggested by Bangga and Sasongko [104]. However, the approach shall be handled with care because the tuning of the parameters can vary from one case to another [159]. Thus, this is not applied in the present studies.

5.2.2 3D Spatial and Temporal Discretization Studies

To show that the 3D CFD solutions are independent of the spatial resolution, 3D grid convergence index (GCI) studies according to Celik *et al.* [160] were performed to quantify the numerical uncertainty. For this purpose, the studies were conducted at a constant wind speed and rotational speed of 10.5 m/s and 9.02 rpm, respectively. This particular operating condition was defined as the baseline/benchmark condition in the AVATAR rotor simulations [120]. The flow field resulting from these operating conditions is massively separated in the inboard region that is crucial for the 3D effects. The centrifugal force has a strong impact within this area by transporting the separated boundary layer to the outer blade region, creating a strong radial flow component. A strong chordwise flow acceleration occurs as a response of the flow to the Coriolis force. Preceding studies [56, 57] showed that the lift coefficient was significantly higher than in the 2D conditions in the inboard area of the AVATAR turbine under the aforementioned operating conditions.

Three different resolutions of the blade mesh were examined. The mesh was refined systematically with the refinement factor about 1.4 in radial direction. The results of the converged 2D grid were applied in building the 3D mesh. Thus, the radial grid resolution is the only parameter evaluated for the 3D grid studies. The coarse blade mesh consists of 136 cells in radial direction (blade total cells number of 8.1 x 10^6), medium mesh of 192 cells (10.9 x 10^6) and fine mesh of 272 cells (15.9 x 10^6). The background, wake refinement and nacelle meshes consist of 1.9 x 10^6, 16.34 x 10^6 and 3.5 x 10^6 cells, respectively. They were maintained constant without refinement. The simulations were carried out until the wake was fully developed after 11 revolutions. Then, the data were extracted and averaged over the last revolution, excluding the initial 10 rotor revolutions. It is shown Figure 5.7 that time-averaging over one revolution after a fully developed solution is sufficient to capture the general
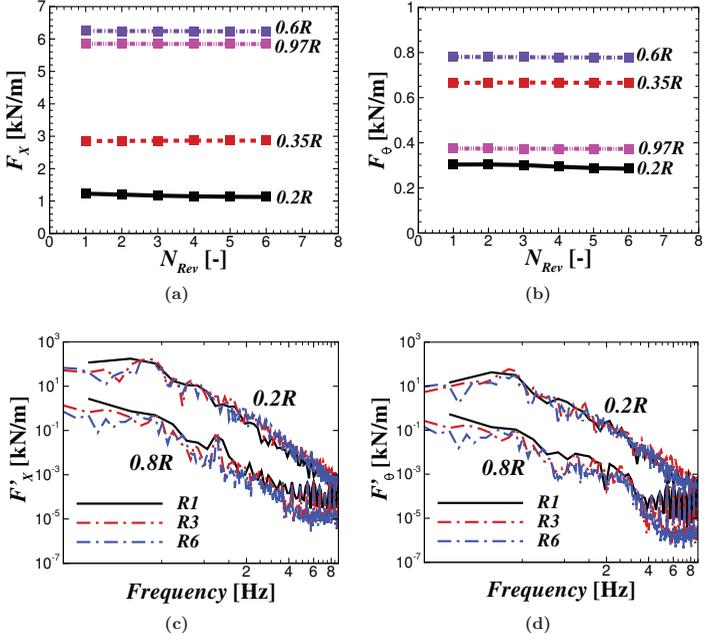
Figure 5.7: Impact of the number of revolution on the averaged sectional loads (5.7a and 5.7b) and frequency spectra (5.7c and 5.7d). R1, R3 and R6 indicate the number of revolutions. Variable F' represents the amplitude of the resulting forces. The calculations were carried out using DDES. *Figures 5.7c and 5.7d are taken from [141].*

behaviour of the aerodynamic loads at the inboard and outboard sections of the blade. Furthermore, the frequency spectra are very similar, though the amplitude for $R1$ is smaller in the blade inboard region and a bit higher in the outer blade sections compared to $R3$ and $R6$. The presented spectra are obtained only for one to six rotor revolutions. Thus, it is clear that statistical convergence is not yet achieved especially for the small frequency domain. It shall be noted that $R1$ is for 11 (10+1) rotor revolutions, $R3$ for 13 (10+3) and $R6$ for 16 (10+6). These evaluations were given in [141].

The results of the GCI for power and thrust are shown in Table 5.2. The grid convergence index for the fine grid is very small (less than 0.5%), stating that the solutions are spatially converged. It can be seen that the magnitude of power and thrust for the medium and the fine grids are very close. The extrapolated relative errors are less than 0.5% in both parameters, while a higher error is observed for the coarse grid due to inaccurate prediction of the sectional forces in the blade inboard

Table 5.2: Grid convergence study for the AVATAR blade using the GCI approach. Data are obtained from the URANS calculations. *Table is taken from [67].*

Parameter	Power	Thrust
Value fine	9.28×10^6 W	1.330×10^6 N
Value medium	9.26×10^6 W	1.328×10^6 N
Value coarse	9.20×10^6 W	1.326×10^6 N
Extrapolated rel. error		
-fine	0.12%	0.27%
-medium	0.36%	0.47%
-coarse	1.02%	0.58%
Grid convercence index	0.15%	0.34%

region as already shown in [56].

Figure 5.8 presents the CFD prediction using URANS and DDES for the studied blade mesh resolutions in terms of the axial force (F_X) and tangential force (F_θ). F_θ acts in the tangential direction relative to the blade in θ-axis. The reader is suggested to refer to Figure 2.4 for the description of the coordinate system. It shall be noted that the predicted sectional loads in Figure 5.8 for all the grids show a strong fluctuation in the inboard region, but this is not shown for clarity. It can be seen clearly that the behaviour of the predicted loads using URANS and DDES agrees well where the coarse mesh strongly underpredicts the sectional load at $r/R \approx 0.2$ for F_X and $r/R \approx 0.15$ for F_θ. This results in the smaller magnitude of the rotor power and thrust for the coarse mesh shown in Table 5.2. On the other hand, the time averaged results for the medium and the fine meshes are similar. Furthermore, it was observed that flow separation resulting from the medium and fine meshes is comparable, inferring that 3D assessment of the rotor using the medium grid is plausible. Detailed discussions of the 3D flow characteristics will be given further in Section 5.6. Therefore, considering the computational cost and the solution accuracy, the medium grid is chosen and used in all further simulations. The computational effort required for each 3D rotor computation was 8400 CPUh on the LAKI cluster from the High Performance Computing Center Stuttgart (HLRS).

In order to investigate the sensitivity of the CFD predictions against the temporal discretizations, the DDES computations were carried out for various time step sizes. The smallest time step, $\Delta t = 0.125°$, was used as the benchmark case. This particular time step resolution has been observed by Weihing *et al.* [78] to sufficiently capture the small vortices of the MEXICO rotor. Furthermore, they obtained good agreement with measurement data [119] by using this small time step size. Three other time step resolutions were examined in the present work, namely $\Delta t = 1°$, $2°$ and $3°$, and the results are depicted in Figure 5.9. The predicted rotor axial and tangential forces along the blade radius are similar for various time step sizes. Small deviations are observed in the root region for $r/R < 0.1$ where the shape of the blade section is
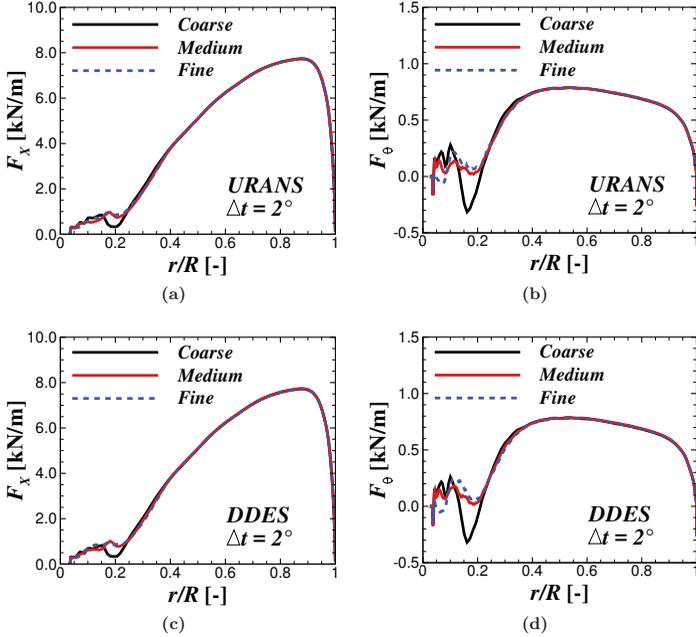
Figure 5.8: Impact of grid resolution on the predicted sectional loads using URANS (5.8a and 5.8b) and DDES (5.8c and 5.8d) computations. Increasing grid resolution hardly changes the CFD results from the medium to fine meshes, but a small deviation between the medium and fine meshes is observed in the inner part of the blade for F_θ especially in the DDES solutions.

almost cylindrical with the relative thickness of more than 94%, see Table 5.1. Thus, the time averaged solution becomes more sensitive towards the temporal discretization. One other possibility is that longer simulations, more than 11 (10+1) rotor revolutions, are required for this small time step size. Nevertheless, the results for all the examined time steps are consistent for $r/R \geqslant 0.1$. Considering the computational cost, the time step size of $\Delta t = 2°$ is used for the rest of the simulations.

5.2.3 Comparison with Other CFD Simulations

There is no measurement data available for the AVATAR blade. Hence, a code-to-code comparison was used in the AVATAR Report 2.3 [121] to verify consistency of the simulations. In these studies, the sectional loads predicted by CFD computations from
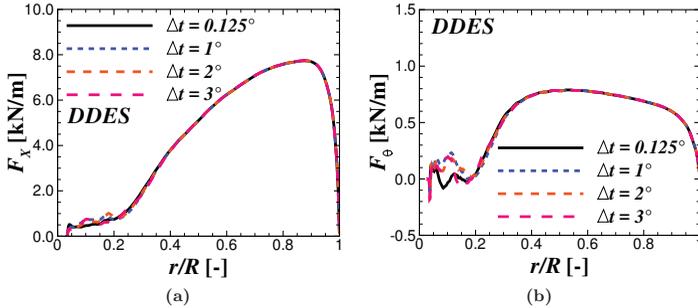
Figure 5.9: Impact of time step resolution on the predicted sectional loads using DDES. The predicted sectional loads are consistent for various time step resolutions for $r/R \geqslant 0.1$.
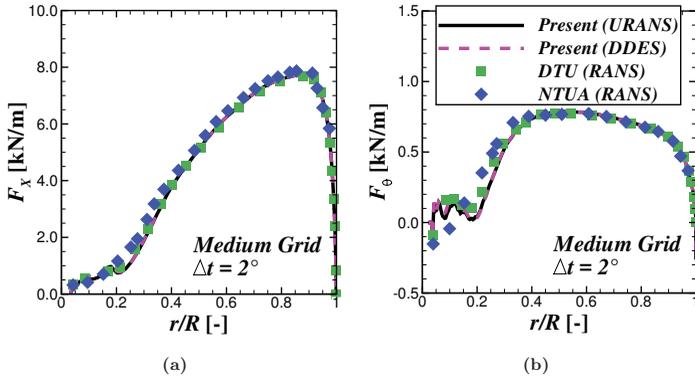
Figure 5.10: Comparison of the present simulations with the other CFD results obtained from [121]. Very good agreements are obtained in both the rotor axial and the tangential forces.

Denmark Technical University (DTU) using the Ellpsys3D code [161] and from National Technical University of Athens (NTUA) using the MaPFlow code [162] were used for comparison. All the simulations were carried out for the standard test case of $U_\infty = 10.5$ m/s [121]. Descriptions of the employed codes are given in the AVATAR Report 2.3 [121]. Different CFD results provided by the University of Stuttgart (USTUTT) in the report [121] were performed at the IAG employing a steady state condition and a coarser mesh resolution, *i.e.,* 200 x 140 cells in chordwise and spanwise directions, respectively. The RANS Menter SST $k - \omega$ turbulence model [102] was employed for

these computations [121]. Some of the simulations in the report [121] were conducted by employing transition prediction methods, but only the fully turbulent results are included in the present studies for consistency.

Figure 5.10 presents the comparison of the rotor aerodynamic forces from the present works with the other CFD computations. It can be seen that the predicted sectional loads agree well with the other reference CFD computations. The simulations compute the maximum axial force of 7.74 kN/m (USTUTT-DDES and -URANS), 7.68 kN/m (DTU) and 7.87 kN/m (NTUA) at $r/R \approx 0.88$. As the unsteady effects are considered in the URANS and DDES simulations, it can be seen that the forces slightly drop at $r/R \approx 0.2$. For this particular case, as already mentioned in Section 5.2.2, a strong radial flow component beyond the separation line was already observed in [56, 57]. The inboard region is operating in the post-stall condition with $\alpha = 16°$ for $r/R = 0.15$ and with $\alpha = 11.5°$ for $r/R = 0.2$, while the outer part of the blade is in the linear region of the lift curve. Thus, it is challenging to obtain good agreements in the inboard region of the blade because the flow is massively separated involving a strong unsteady fluctuation. Additionally, the present URANS results are very similar to the DDES computations. This was also observed for the higher wind speed case in [141]. In all further CFD computations, the URANS approach is then applied unless stated otherwise.

5.3 Evaluations of the angle of attack extraction methods

In this section, consistency of the angle of attack prediction is evaluated. Two approaches were investigated: (1) the reduced axial velocity (RAV) method [126] and (2) the SHS approach proposed by Shen *et al.* [130]. The latter employs a monitor point and assumes the bound circulation at the quarter blade chord position. The methods were coded in [128, 129] and tested in [57, 67, 146].

As described briefly in Section 2.4, the RAV method azimuthally averages the flow field in each monitor plane, upstream and downstream of the rotor. The axial distance of the extraction planes was set to $3c$ relative to the rotor position (Figure 5.11a). Then, linear interpolation was used to determine the effective velocity in the rotor plane. In the present studies, this procedure was performed each physical time step ($\Delta t = 2°$), resulting in a dataset consisting of 180 different velocity distributions for each rotor revolution. The angle of attack was calculated as

$$\alpha = \tan^{-1}\left(\frac{(1-a)U_\infty}{(1+a')r\Omega}\right) - \beta, \tag{5.2}$$

where a, a' and β are the axial induction, tangential induction and local twist angle, respectively. These are defined as

$$a = \frac{U_\infty - U_{rotor}}{U_\infty} \tag{5.3}$$

and

$$a' = \frac{V_{\theta,rotor} - \Omega r}{\Omega r} \tag{5.4}$$

where U_{rotor} and $V_{\theta,rotor}$ represent the axial and tangential velocities, respectively, in the rotor plane. Illustration of the velocity triangle is given in Figure 5.12. From the calculated angle of attack, the lift and drag forces acting on the blade section can be obtained. This procedure was carried out for each velocity distribution. As a
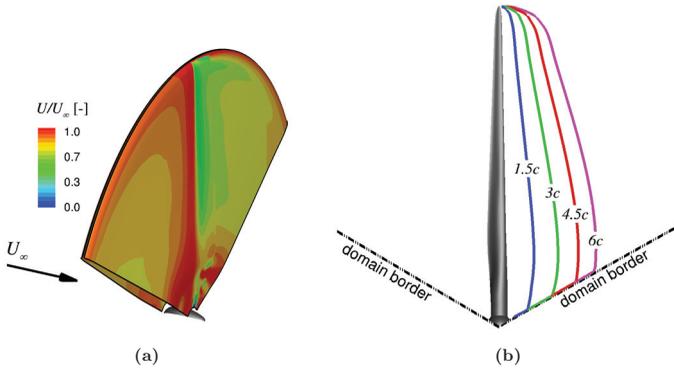
Figure 5.11: Schematic view of the angle of attack extraction method employed in the studies. (a) The axial velocity increases upstream of the leading edge in the root region. (b) The extent of monitor point is limited near the root for the SHS method in the 120° simulation model.
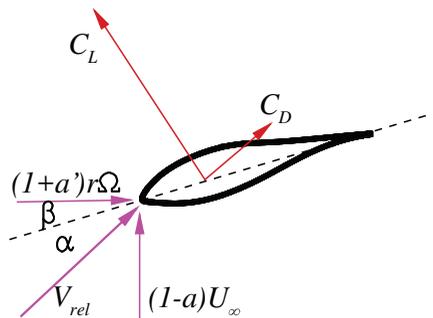
Figure 5.12: Illustration of the velocity triangle at a blade section.

consequence, this results in 180 different α data. Time averaging was then performed on the extracted data.

For the SHS method, the monitor point is located exactly in the rotor plane upstream of the leading edge. Four variations of the monitor point distance to the leading edge were examined, namely 1.5c, 3c, 4.5c and 6c. Each radial station is assigned to a monitor point distributed along the blade radius. Figure 5.11b illustrates the lines connecting the monitor points for different upstream distances. For the 120° simulation model, the extent of the monitor point is limited by the domain border near the root region. First, the initial flow angles were determined using the measured velocity at every control point. The lift and drag forces were then calculated using these initial angles. The obtained forces were used to calculate the circulation distribution over the blade radius. Then, the induced velocity can be determined. The new inflow angle can be obtained from the difference between the initial and the induced velocities. This procedure was repeated until convergence is achieved. Similar to the RAV method, the angle of attack distribution was estimated each physical time step before applying the time averaging.

Figure 5.13 presents the results of the angle of attack prediction using the RAV and SHS approaches for the wind speed case of 10.5 m/s. It is shown that the angle of attack distributions are similar regardless of the monitor point distance from the leading edge, especially for $r/R \geqslant 0.2$ (Figure 5.13a). Similarly, the lift coefficient distributions, depicted in Figure 5.13b, calculated using the two different methods agree well for $r/R \geqslant 0.12$. Despite that, it is shown that a higher lift coefficient is obtained by the SHS method with the monitor point distance of 1.5c compared to the others. On the other hand, the SHS method shows slightly higher values of α than the one estimated by the RAV method in the root area for $r/R < 0.2$. Further inboard in the extreme root area, $r/R < 0.12$, C_L drops significantly for all the SHS computations. In contrast, the RAV method shows a remarkable increase of the lift coefficient. The limitation of the monitor point distance for the 120° simulation model is expected to cause the deviation between the SHS and the RAV results in the extreme root area. This interesting phenomenon seems strange, as not only the magnitude of C_L from both methods differs but also the trend of the C_L distribution in the extreme root area. To investigate the cause of this inconsistency, the estimated axial (a) and tangential (a') induction factors are presented in Figures 5.13c and 5.13d, respectively. Similar to the lift coefficient behaviour, it is shown that the axial induction obtained by the SHS method drops significantly, even reaches a negative magnitude, for $r/R \leqslant 0.2$. In contrast, it increases for the RAV method. These observations explain the characteristics of the higher predicted α in the root area estimated by the SHS method, depicted in Figure 5.13a. It can be inferred that a stronger axial velocity in the rotor plane is predicted by the SHS method. It is shown in Figure 5.11a that the region upstream of the leading edge, where the monitor point is located, is characterized by an increased axial velocity. As the SHS method uses only a single monitor point in front of the leading edge, then it is already expected that the method produces a stronger axial velocity and, as a consequence, a lower axial induction. To account for the velocity drop downstream of the trailing edge, the wake
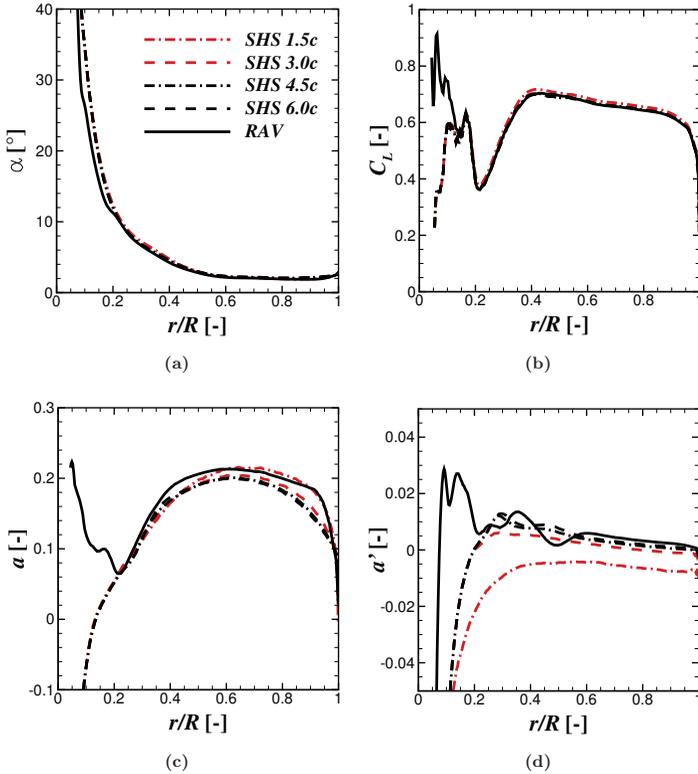
Figure 5.13: Characteristics of the predicted angle of attack, lift coefficient and induction factors using the RAV and SHS methods for the wind speed case of 10.5 m/s.

induced effect needs to be considered in the development of this approach. Additionally, it is interesting to see that the axial inductions coincide in the root region for various monitor point distances, similar to α and C_L. This is strongly expected to correlate with the limitation of the control point distance for the 120° simulation model (Figure 5.11b) where all the extraction lines collapse within this area.

In terms of the tangential induction, Figure 5.13d shows that RAV locally predicts an augmentation of the tangential induction in the root area before it drops at $0.1R$. This phenomenon is not observed for the SHS method. In fact, the tangential induction factor estimated by this approach gradually drops for $r/R < 0.25$. It is shown that

the tangential induction agrees fairly well for both extraction methods, except for the monitor point distance of $1.5c$. Thus, it is clear that setting the monitor point too close to the leading edge is not recommended. This conclusion was also given earlier by Shen *et al.* [125, 130].

To sum up, it can be seen that the α extraction near the hub shows uncertainties. This means, as already stated in Chapters 3 and 4, that discussions on the 3D effects for the thick airfoil and the cylindrical part of the blade in the extreme root area may be impaired by faults in the α prediction. Considering the strange behaviour of the SHS method near the root, as the control point is limited by the simulation domain border, the RAV method is suggested for the 120° simulation model and will be used for the rest of the simulations.

5.4   3D Effects on Aerodynamic Coefficients

To briefly recall the studied test case, the operating condition and simulation strategy for the AVATAR rotor are as follows. Five different wind speeds were examined ranging from below to above the rated condition ($U_\infty = 10.75$ m/s), namely $U_\infty = 5$ m/s, 10.5 m/s, 15 m/s, 20 m/s and 25 m/s. The pitch angle and rotational speed were kept constant at 0° and 9.02 rpm, respectively, to artificially generate massive separation for the high wind speed case. The URANS $k - \omega$ turbulence model assuming a fully turbulent boundary layer was employed. The time step size of 2° was chosen in these studies.

The effective angle of attack was evaluated using the reduced axial velocity (RAV) method [126] described in the previous section. The extracted angle of attack was then used to calculate the lift and the drag forces based on the calculated total force from the pressure and shear stress distributions. It shall again be noted that the resulting forces are sensitive against the accuracy of the effective angle of attack evaluation. The aerodynamic coefficients for the 3D rotating and the 2D non-rotating cases at six radial positions from the inboard to the outboard sections are compared in Figures 5.14 and 5.15 in terms of C_L and C_D, respectively. The local flow velocity, including induction effects, was used to non-dimensionalize the forces. The black lines represent the 3D case and the red lines represent the 2D case. Each point of the 3D case in the figure corresponds to a different wind speed. A higher angle of attack was obtained by increasing the wind speed and by maintaining the rotational speed and pitch angle constant. The Reynolds number of the blade sections increases slightly with increasing wind speed. On the other hand, the 2D simulations were performed at a constant Re. The magnitude is correlated to the Re of the blade section for the case of $U_\infty = 10.5$ m/s presented in Table 5.1. The difference between Re in the 3D case at maximum α to the 2D case is less than 10%. In the figures, the horizontal and vertical error bars represent the standard deviation of the unsteady fluctuations for the angle of attack and lift/drag coefficient, respectively. Large standard deviations in α and C_L in the inboard region at high α show that the case is highly unsteady.

Before discussing the 3D effects, the aerodynamic behaviour of the thick airfoils
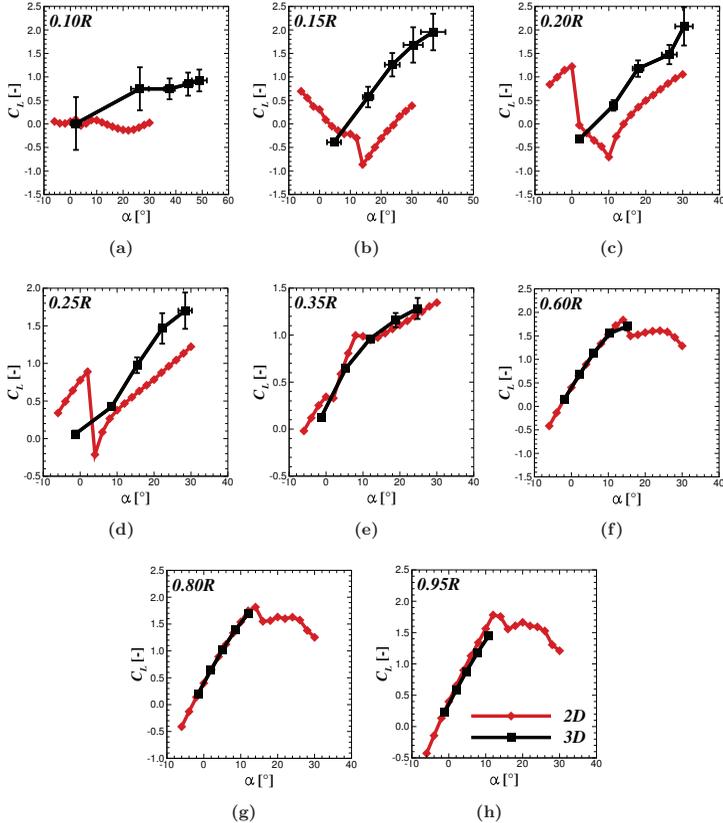
Figure 5.14: 3D and 2D C_L polars. 3D C_L is remarkably higher than in the 2D conditions, except in the middle and the near the tip regions. Unsteady fluctuations for the 2D case are not presented in the figure. *Figure is taken from [67].*

constructing the AVATAR blade will be discussed to establish a more credible basis for the subsequent 3D aerodynamics. Especially for the inboard airfoils where $t/c = 0.94$ (Figure 5.14a), 0.75 (Figure 5.14b), 0.57 (Figure 5.14c) and 0.46 (Figure 5.14d), the two-dimensional C_L response is complex, and deviates significantly from routinely observed responses for more conventional thinner airfoils like those employed in the
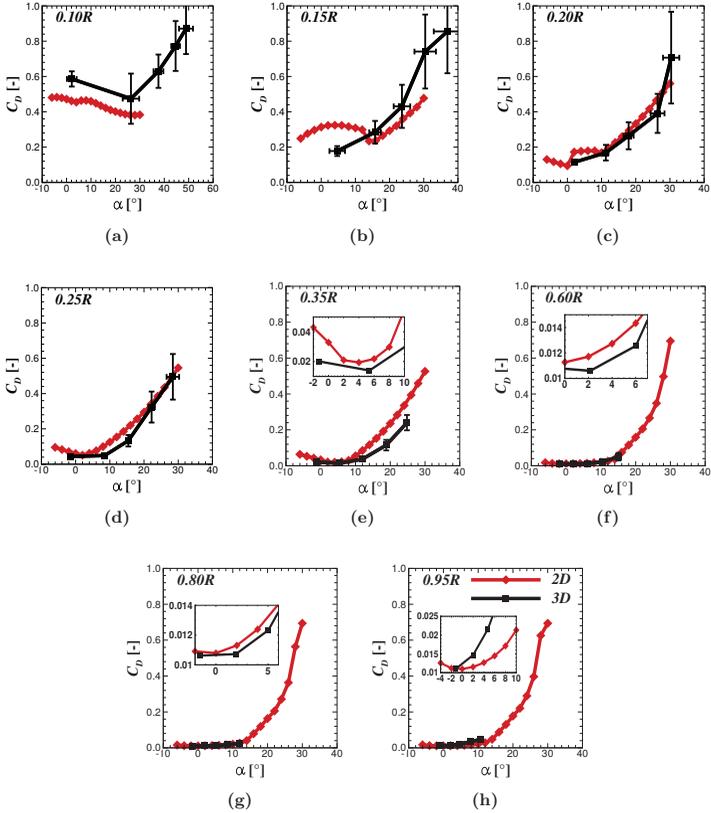
Figure 5.15: 3D and 2D C_D polars. 3D C_D is smaller than in the 2D conditions in general. It is higher than in 2D case near the tip and at high angle of attack in the inboard region. Unsteady fluctuations for the 2D case are not presented in the figure. *Figure is taken from [67].*

outer blade region, Figures 5.14f - 5.14h. For the most inboard airfoil, where $t/c = 0.94$, the two-dimensional lift magnitude is almost constant ($C_L \approx 0$) independent of the angle of attack. This can be expected because the airfoil shape is almost cylindrical. For the slightly thinner airfoils, it can be seen that C_L decreases with increasing angle of attack for a certain range. For the relative thickness of $t/c = 0.75$, this is observed

(a) 2D SS.

(b) 2D PS.

(c) 3D SS.

(d) 3D PS.
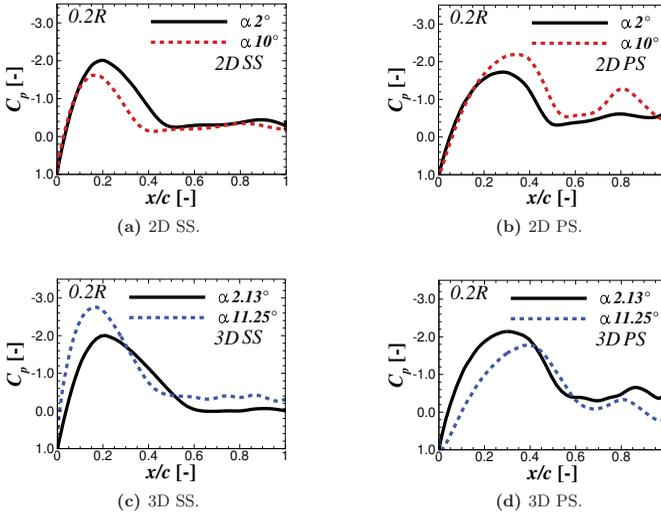
Figure 5.16: Time averaged C_p distributions of the 2D and 3D simulations at two different angles of attack. In the 2D case, C_p decreases on the pressure side and increases on the suction side at a higher angle of attack, marking the occurrence of the decambering effect due to excessive boundary layer thickness and flow separation. This is not observed in the 3D case. *Figure is taken from [67].*

up to $\alpha = 12°$. A lesser extent of the phenomenon is shown with decreasing relative thickness. This occurs within $-2° < \alpha < 10°$ for $t/c = 0.57$ and within $0° < \alpha < 4°$ for $t/c = 0.46$. To study the root cause of this observation in more detail, distributions of the pressure coefficient for the airfoil with $t/c = 0.57$ at $\alpha = 2°$ and $10°$ are presented in Figure 5.16; where Figures 5.16a and 5.16b are for the suction and pressure sides, respectively. It can be seen that the minimum pressure becomes more positive with increasing α for the C_p distribution on the suction side. On the contrary, C_p becomes more negative on the pressure side for increasing α. As a result, the lift coefficient reduces significantly for $\alpha = 10°$, even reaches negative values. It can be seen that even for these small angles of attack, massive separation is observed for both airfoil sides, causing displacement effect and reducing the effectiveness of the airfoil.

As massive flow separation is observed, a strong 3D effect is likely to occur for the inboard airfoils, even for small α. Figures 5.16c and 5.16d show the C_p distributions of the airfoil with relative thickness of 0.57 extracted from the rotating blade. Two angles of attack that are comparable with the 2D conditions are shown. It can be seen that the minimum C_p becomes more negative with increasing α on the suction
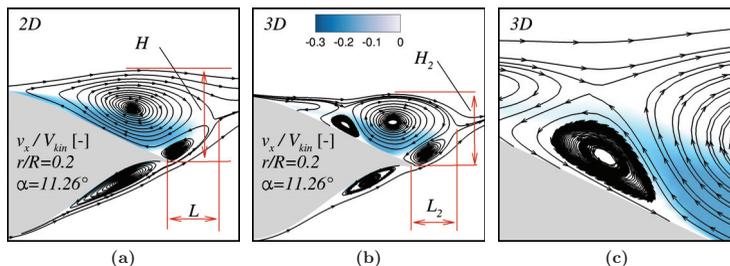
Figure 5.17: Time averaged relative streamwise velocity (v_x/V_{kin}) field near the airfoil section. The velocity is non-dimensionalized by the local kinematic velocity. Separation area is significantly reduced, $H_2 < H$ and $L_2 < L$. The area of the negative streamwise velocity (blue colour) is remarkably smaller in the 3D case. *Figure is taken from [67].*

side, and more positive with increasing α on the pressure side. As a result, the lift coefficient increases within this α-range creating a big difference between the 2D and 3D C_L slopes. In Figure 5.17, the velocity fields around the airfoil for the 2D and 3D conditions are shown. It can be seen that separation is delayed remarkably in the 3D condition. The size of separation and negative streamwise velocity areas become smaller. The displacement effect caused mainly by the thickness of the boundary layer reduces for the rotating blade. In Figure 5.17, the vertical height of the separation area relative to the trailing edge position is indicated by H (for 2D) and H_2 (for 3D). It is shown that H_2 is significantly smaller than H, see Figures 5.17a and 5.17b. As a result, the decambering effect that is strongly dependent upon the displacement thickness is weaker than in the 2D case. Note that the decambering effect is defined as the reduction of camber effectiveness due to excessive boundary layer thickness and flow separation. The shallower separation area in the 3D case is caused by the effect of the centrifugal pumping that transports the separated flow towards the blade outer area. This causes a boundary layer thinning that enhances the stability of the flow against separation [30]. The Coriolis force acts in chordwise direction and helps the flow to overcome the adverse pressure gradient, delaying the occurrence of separation on both airfoil sides. The latter was shown by Du and Selig [30] to have a stronger impact for the separation delay than the centrifugal pumping. In addition, a smaller secondary vortical structure exists in the 3D case downstream of the separation point that is not observed for the 2D condition (Figure 5.17c). This small structure is created due to the 3D response of the chordwise flow acceleration by the Coriolis force. This hypothesis will be confirmed by the occurrence of the strong Coriolis force influence around this area presented in Section 5.6. It can be seen that the direction of the vortex is counter-clockwise, which implies that the near wall flow is not separated even though the surrounding global flow feature is within the separated area.

In the most inboard region, at $r/R = 0.1$, C_L for the 3D case shows positive lift coefficients even though the shape is almost cylindrical ($t/c \approx 0.94$) while the 2D
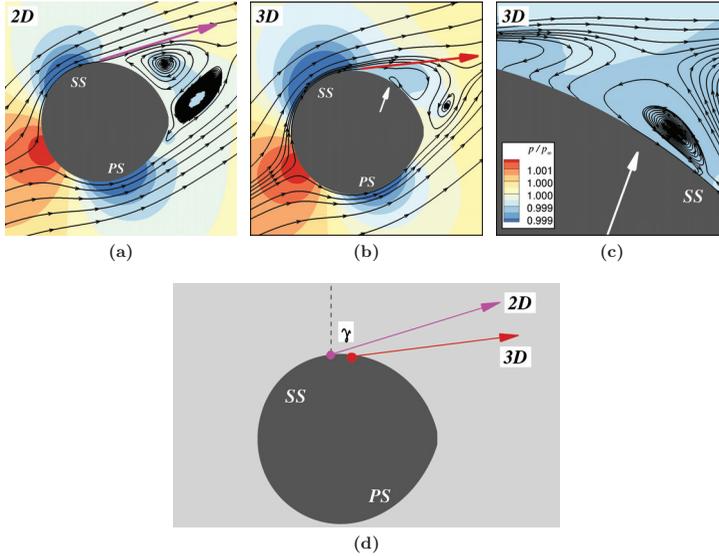
Figure 5.18: Time averaged pressure fields around the airfoil and rotor at $r/R = 0.1$ (5.18a and 5.18b). Figure 5.18c presents enlarged view of Figure 5.18b. Schematic view of the separation characteristics for the cylindrical shape in the root area is given in Figure 5.18d. Lift increase is caused by three main factors: (1) delayed separation, (2) increased flow angle, γ, and (3) reduced pressure effect due to radial flow.

lift coefficients lie around zero magnitude for the whole studied α. This intriguing observation leads to a hypothesis that rotation modifies the symmetrical behaviour of the flow around bluff bodies. Similar to what has been discussed in the preceding paragraph, the 2D pressure field around the airfoil is compared to the corresponding 3D situation in Figure 5.18. In agreement with the above discussion, separation is delayed in the 3D case (5.18a and 5.18b), and a counter-clockwise vortex near the separation point is observed (5.18c). The 3D case shows lower pressure level than the 2D condition on the suction side of the airfoil, upstream and downstream separation, that stems from the boundary layer thinning. This reduced pressure effect was also observed for the MEXICO rotor discussed in Chapter 4. In addition, it is also shown that vertical displacement of the separation area reduces in the 3D case, causing a larger flow angle (γ) as displayed in Figures 5.18a, 5.18b and 5.18d, supporting the observation in the preceding paragraph.

In the inboard region of the blade, a strong augmentation of C_L caused by the 3D effects is observed. The lift stall is remarkably delayed in the 3D case compared
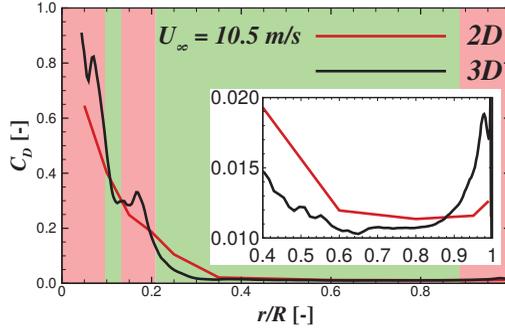
Figure 5.19: Distribution of the drag coefficient along the blade radius for the standard test case of the AVATAR blade. Enlarged view of the C_D distribution near the tip area is presented in the center of Figure 5.19. The areas marked by red colour represent the drag augmentation and the light green areas are for the reduced drag. Zone 1: C_D increase is caused by the reduced pressure effect, zone 2: by downwash and zone 3: by the tip loss effect.

to the 2D case. It is qualitatively in a good agreement with the Himmelskamp effect [3], where the 3D lift increases due to the centrifugal pumping and the Coriolis force [19, 26, 30, 52]. This observation confirmed the conclusion of the preceding studies [56–58, 63, 71, 72, 163] that rotational augmentation was not hindered by the thickness of the employed airfoil. Different from the 3D characteristics of the rotating blade in the root area, the rotation shows a smaller influence in the blade middle part where the C_L polars in both cases are close to each other, Figures 5.14f and 5.14g . When approaching the tip ($r = 0.95R$), the opposite effect on C_L is observed. The lift reduces compared to its magnitude in the 2D situation. It is shown that the reduction increases with the angle of attack, which may indicate the rise of the tip loss with increasing wind speed (decreasing TSR). However, it shall be kept in mind that this behaviour may also originate from the inaccuracy of the angle of attack extraction close to the tip because the wake expansion and distinct tip vortex are not well represented using the averaged method [60]. Despite that, the most outward region examined ($r/R = 0.95$) is still within the unaffected area of the strong wake expansion. Thus, the use of the averaging method is still plausible. In addition, it was observed that α increases close to the tip [57] that indicates the tip loss plays a major role, *i.e.,* a smaller amount of energy is extracted from the wind.

In terms of the drag coefficient, 2D C_D for thick airfoils slightly decreases with increasing angle of attack around $0° < \alpha < 10°$. It is caused by the reduction of the separation zone within the rear-pressure side of the airfoil, see Figures 5.17 and 5.16 for illustration, which contributes to the drag alleviation. It is shown that the point of separation, on the pressure side, is shifted further downstream. Furthermore, a smaller

pressure side loading is observed for the higher α case. This decreases the chord axial force that results in the further drag reduction.

In Figure 5.15, the effect of rotation on C_D is shown. The drag is influenced by the 3D effects for all examined radial positions. It is shown that 3D C_D is lower than the 2D magnitude, except for $r = 0.1R$, $r = 0.15R$ and $r = 0.2R$ at high α; and also for $r = 0.95R$ for all studied α. Especially in the near tip area, the drag augmentation in Figure 5.15h may be associated with the tip loss as also observed for the lift coefficient. The drag increase in the inboard region is expected to stem from two main reasons: (1) the reduced pressure effect in the separation area due to radial flow as shown in Figure 5.18b and (2) the downwash phenomenon which will be discussed further in Section 5.5. A better overview to classify the mentioned effects can be seen in Figure 5.19.

The drag reduction for the AVATAR rotor agrees well with the assumption made by Du and Selig [30, 31] regarding drag alleviation in their 3D correction model [30]. The delay of separation, which is mainly caused by the Coriolis acceleration, is identified as the main actor behind the phenomena. Contradicting the present observation, the results from the NREL UAE Phase VI wind turbine showed that the rotational effect was accompanied by a significant drag increase [52, 60]. According to Lindenburg [156], the drag increase might be associated with the energy needed for the radial pumping. In this study, the local drag augmentation for the cylindrical portion of the blade is explained by the reduced pressure effect. On the other hand, the results of the MEXICO measurements showed that the drag was not severely affected by the rotational effect. Guntur *et al.* [66] tested several correction models for drag on the MEXICO rotor, showing that the 3D correction for drag might be unnecessary. This study was confirmed by Herráez *et al.* [55] who studied the same turbine. They claimed that the 3D effect for drag might be airfoil type dependent. A lower drag was observed for the MEXICO rotor at a radial station of $0.6R$ but was not shown at the inboard stations. Different type of airfoils are used for the MEXICO rotor; the DU91-W2-250 airfoil at $r = 0.25R$ and $r = 0.35R$, and the RISØ-A1-21 airfoil at $r = 0.6R$ [55]. In contrast, the 3D drag coefficient reduces for the MEXICO rotor evaluated in the present study, see Chapter 4. This contradicting conclusions are expected to arise from the variation of the studied operating conditions or in the accuracy of the α extraction. Because of the uncertainty of the rotational effects on drag, a careful selection of the 3D correction models should be taken into account. Therefore, it is clear that the drag correction models which assume the drag increase, *i.e.,* [70, 156, 164], should not be applied for the AVATAR blade, instead suggesting the drag correction models proposed by Du and Selig [30] or Corrigan and Schillings [165].

5.5 Bound Circulation along the Blade Radius

It is worthwhile to mention again that the rotational speed and pitch angle are kept constant in this study to artificially generate stronger separation at the higher wind speed cases. This was done to study the 3D aerodynamic characteristics at the inboard blade region which is strongly influenced by separation. In this section, the bound

circulation distribution of the blade is evaluated. This is estimated by $\Gamma = 0.5cC_LV_{loc}$, where C_L is obtained from the reduced axial velocity technique and V_{rel} represents the local flow velocity including the wake induction effects. The characteristics of the bound circulation over the blade radius is expected as the cause of the local drag increase in zone 2 as depicted in Figures 5.15 and 5.19.

Figure 5.20a presents the time averaged bound circulation for three examined wind speed cases, namely 10.5 m/s, 15 m/s and 25 m/s. It is shown that the circulation magnitude locally changes near the blade root area. Any variation in the radial circulation causes trailing vortices, depicted in Figure 5.21, which has an induction effect on the blade. The trailing vortices plot is coloured by the vorticity in Y-direction to roughly visualize the direction of the vortex; yellow colour is in clockwise direction and purple colour is in counter-clockwise. These root vortices are the consequence of flow separation for the thick airfoils operating at high angles of attack in the root region. It is shown that some distinct trailing vortices are characterizing this area. Relating Figure 5.20a with Figure 5.21 leads to an expectation that a strong downwash is likely to occur in between these vortices due to the variation of their direction, see the direction of the arrow in Figure 5.21c. These distinct vortices grow with increasing wind speed. This has the consequence that the downwash also increases at higher wind speeds. It is shown that the vortex system is weak and not dominant for $U_\infty = 10.5~m/s$, but it becomes noticeably stronger for $U_\infty = 25~m/s$, see Figure 5.21. This is supported by the experimental studies on a model rotor by Akay *et al.* [150, 151], who showed that the root vortices are more concentrated for the blade operating at a smaller tip speed ratio (higher wind speed).

In Figure 5.20, a more rigorous examination towards the phenomenon is given. It
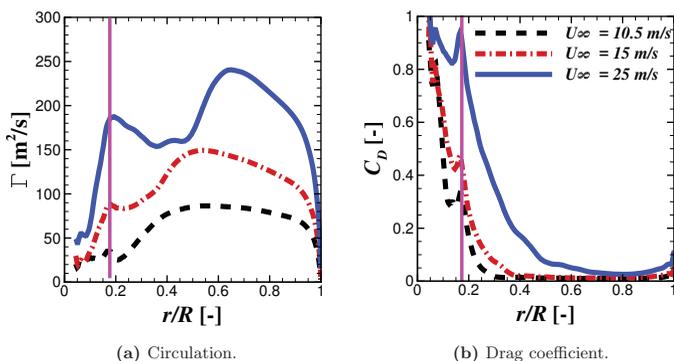
Figure 5.20: Time averaged circulation and drag coefficient distributions over the blade radius. A local increase of the bound circulation is observed in the inboard region which is expected to cause the downwash. *Figure is taken from [67].*
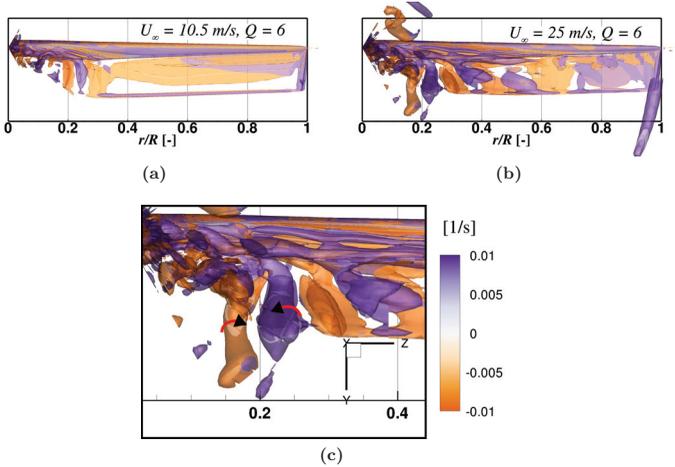
Figure 5.21: Trailing vortices in the inboard region of the blade illustrated by Q-Criterion coloured by vorticity in Y-direction [1/s]. The inboard vortex system becomes stronger with increasing wind speed, showing distinct counter-rotating trailing vortices which induces downwash. *Figure is taken from [67].*

is shown that a local increase of the bound circulation is observed around the radial station of 17% indicated by a solid vertical line. The total induction at this location is influenced by the total trailing vortices along the blade radius, that depends on its radial gradient and the distance to the reference position. It is shown that exactly at the same position, where Γ locally increases, the drag coefficient remarkably enhances as depicted in Figure 5.20b. It implies that the counter-rotating vortices in the inboard/outboard of the Γ peak induce a downwash at the peak location, locally increasing pressure drag higher than the 2D condition. Consistent with the observation for the trailing vortex system in Figure 5.21 and circulation distribution in Figure 5.20a, the drag coefficient is augmented locally by the downwash and is more pronounced at higher wind speeds.

In addition, the fact that these inboard regions use very thick airfoils with maximum thickness more than 40% leads to the expectation that these phenomena might be associated with massive flow separation and unsteady characteristics, compared to the usual downwash near the tip that is more steady. Further investigation in this regard is suggested to quantify the interaction between the trailing vortices (due to spatial gradient) and the shed vortices (due to temporal gradient).

5.6   Root Flow Characteristics

5.6.1   Near Wall Flows around the Rotating Blade

Three-dimensional flow field for the rotor aerodynamics, especially in terms of the radial flow, is complex and influenced by many aspects, among them are the radial pressure gradient due to the difference of the local flow velocity and airfoil shapes, viscous effect, and also the Himmelskamp effect [3] governed mainly by the Coriolis and centrifugal forces. These forces will be called as the *Himmelskamp force* ($\vec{F} = \vec{F}_{Coriolis} + \vec{F}_{centrifugal}$), acting in orthogonal direction to each other. The Himmelskamp effect is the main focus in the present studies and quantification of the Himmelskamp force is necessary. On this basis, the ratio of the Coriolis to centrifugal forces (η) is considered in this section which can be interpreted as the acting angle of the resulting force from the blade axis. The physical meaning of this parameter can be given as follows. In the extreme case, for $\eta = 0$, the resulting Himmelskamp force acts solely in positive spanwise direction while for $\eta \to \infty$ the force is solely in chordwise direction. The latter results in a strong streamwise flow acceleration. The relative magnitude of the forces can yield information about the impact of three-dimensionality of the boundary layer. In this analysis, the ratio of these forces is weighted by the Rossby number defined as:

$$\eta \; = \; \frac{\vec{F}_{Coriolis}}{\vec{F}_{centrifugal}} \frac{1}{Ro} = \frac{-2\left(\vec{\Omega} \times \vec{V}\right)}{\vec{\Omega} \times \left(\vec{\Omega} \times \vec{r}\right)} \frac{\Omega c}{\sqrt{U_\infty^2 + (\Omega r)^2}}, \tag{5.5}$$

where $\vec{\Omega}$ is the rotational speed, $\vec{r}$ is the distance of the specific point to the center of rotation and $\vec{V}$ is the fluid velocity in the rotating frame of reference. Ro is the Rossby number defining the ratio between the inertial force and the Coriolis force. In this case, Ro is included, instead of only the Coriolis to centrifugal ratio as used in [57], because a variation of the wind speed produces a variation in the inertial force. The results for three different wind speeds are plotted in Figure 5.22; for $U_\infty = 10.5$ m/s (5.22a - 5.22c), $U_\infty = 15$ m/s (5.22d - 5.22f) and $U_\infty = 25$ m/s (5.22g - 5.22h). Three different radial stations are evaluated, namely $0.15R$, $0.2R$ and $0.35R$.

The contour of η for the wind speeds of $U_\infty = 10.5 \; m/s$ at $r/R = 0.15$ is presented in Figure 5.22a. It can be seen that the magnitude of η reduces with increasing radial distance, as shown in Figures 5.22b and 5.22c. The other studied wind speed cases, $U_\infty = 15 \; m/s$ and $25 \; m/s$, also show a similar behaviour. It is also shown that the affected region of the Coriolis force enlarges with increasing separation size. The Coriolis term increases its magnitude depending on the spanwise flow strength and becomes stronger with increasing c/r [27, 28, 166]. This observation implies that the acting angle of the Himmelskamp force is larger approaching the center of rotation, which clearly indicates that the Coriolis effect dominates over the centrifugal force. As a consequence, separation is delayed mainly by the Coriolis force and slightly by the centrifugal effect. This physical behaviour might be the reason why Du and Selig [30] observed that the Coriolis force is more dominant for separation delay.
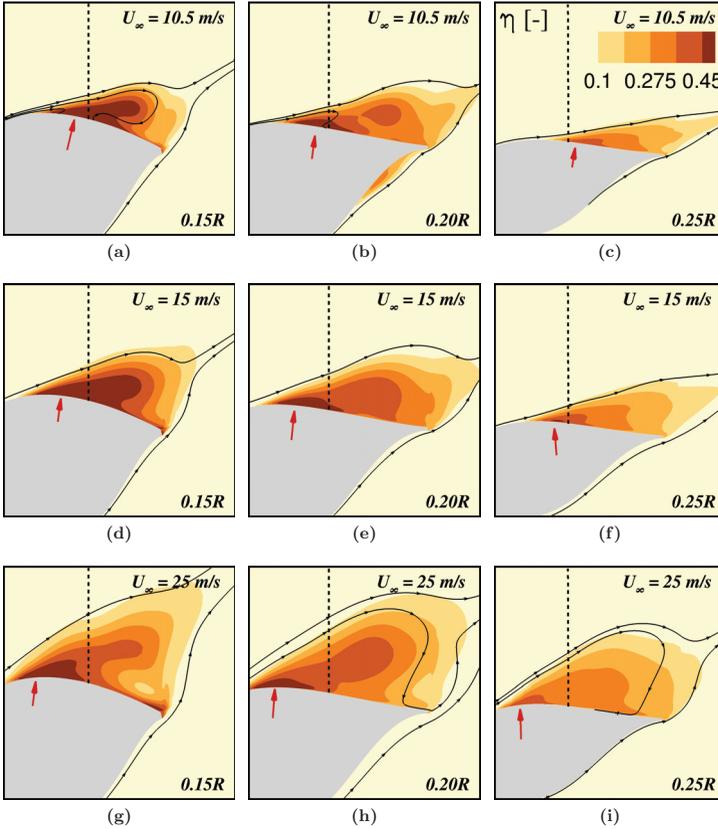
Figure 5.22: Time averaged ratio between the Coriolis and the centrifugal forces weighted by the Rossby number at some selected inboad stations ($0.15R$, $0.2R$ and $0.35R$) and for three different wind speeds: $10.5 \ m/s$ (5.22a-5.22c), $15 \ m/s$ (5.22d-5.22f) and $25 \ m/s$ (5.22d-5.22f). η decreases with radial distance and wind speed while it is strongest close to the separation point. The red arrows indicate the area with a strong Coriolis acceleration. Dashed vertical lines represent the extraction positions for the η, v_z/V_{kin} and v_x/V_{kin} profiles. *Figure is taken from [67].*

With increasing wind speed, the angle of attack increases accordingly. It can be seen that the size of separation is larger for the wind speeds of $15 \ m/s$ and $25 \ m/s$ compared to $U_\infty = 10.5 \ m/s$. On first thought, one might think that stronger separation will lead
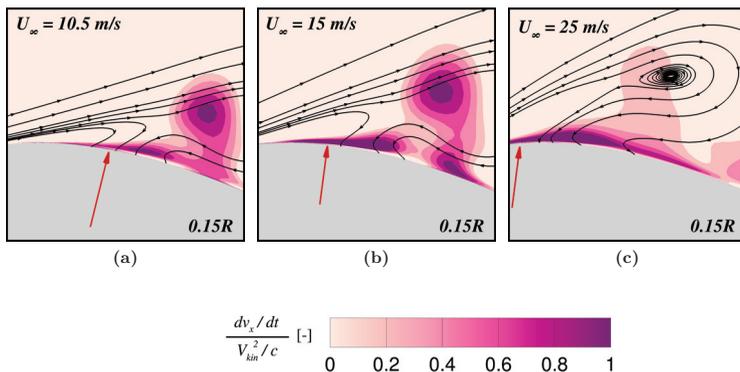
Figure 5.23: Time averaged dimensionless velocity acceleration in chordwise direction at $0.15R$ for three different wind speeds: 10.5 m/s (5.23a), 15 m/s (5.23b) and 25 m/s (5.23c). A strong accelerating flow region is observed starting from the separation point.

to a stronger Coriolis effect. However, this is not necessarily true for all cases. It is clearly shown that η alleviates for the larger wind speeds. This confirms the conclusion made by Du and Selig [30] regarding the weakening of the separation delay at higher wind speeds. In addition, the higher angle of attack (for the higher wind speed case) leads to a shift of the region with a strong Coriolis acceleration (denoted by the red arrow) further upstream. It is logical because the separation point also moves further upstream. It supports the evaluation of Banks and Gadd [12] and McCroskey and Yaggy [4] that the spanwise flow is strongest in the beginning of separation.

As the region with high η magnitude is characterized by a strong Coriolis force, it is expected that the fluid particles in this area are strongly accelerated. To confirm this hypothesis, the convective flow acceleration in chordwise direction can be calculated as

$$\frac{dv_x}{dt} = v_x \frac{\partial v_x}{\partial x} + v_y \frac{\partial v_x}{\partial y} + v_z \frac{\partial v_x}{\partial z}, \tag{5.6}$$

where v_x, v_y and v_z denote the local fluid velocity in rotating frame of reference, *i.e.,* the effect of blade rotation is included. The ratio of the kinematic velocity (squared) to the local chord length is used for the non-dimensionalization parameter. The results are plotted in Figure 5.23. The arrows point on exactly the same position as the arrows in Figure 5.22. It can be clearly seen that a strong flow acceleration is observed starting from the separation point extending downstream along the airfoil surface. It becomes evident that the streamlines of the separated flow field start to bend in this area, creating a positive near wall flow even though the mean flow field is separated. This behaviour was shown already in the discussion of the decambering effect alleviation depicted in Figure 5.17. Additionally, there is a region a bit farther from the wall

with a strong chordwise velocity acceleration located near the edge of the separation area. This is caused by the displacement effect of the vortical structure that lies on the upper side of the airfoil. It seems that this local flow acceleration is connected with the magnitude of η. It can be seen that the flow acceleration is strong for the wind speeds of 10.5 m/s and 15 m/s, but alleviates significantly for the case of $U_\infty = 25$ m/s. A similar finding is made for η on the same position, as depicted in Figures 5.22a, 5.22d and 5.22g for the wind speeds of 10.5 m/s, 15 m/s and 25 m/s, respectively. These observations imply that the mean flow acceleration within the separated flow regime is driven by the Coriolis effect, $i.e.,$ influenced by the spanwise flow.

Figure 5.24 shows the profile of η, v_z/V_{kin} and v_x/V_{kin} for several radial distances. The location of the extraction is illustrated by the dashed vertical line in Figure 5.22. The magnitude of the presented velocities are normalized by the kinematic velocity and y is normalized by the boundary layer thickness (δ) for a better comparison between different wind speed cases. δ is calculated as the distance from the wall to the point where $v_x \approx 0.99 v_{x,inv}$ along the dashed vertical line in Figure 5.22. $v_{x,inv}$ is the inviscid part of v_x outside of the boundary layer area.

In the outer boundary layer regime, it is shown that $\eta \to 0$ which indicates that the Coriolis force is negligible, supporting the discussion given above. In Figure 5.24a, it can be seen that the acceleration angle increases closer to the wall. This implies that the viscous 3D effects act only within the boundary layer. The maximum η magnitude near the wall decreases with increasing radial distance. It can be also seen that η near the wall reduces for the higher wind speed cases. Interestingly, the strength of the reduction becomes more noticeable for the smaller radial position. However, the opposite phenomenon is observed at larger y/δ, where η enhances with increasing wind speed. These effects are explained in the following discussion.

Outside of the negative streamwise velocity area, $e.g.,$ on the region above the shaded-green mark for the case of $U_\infty = 10.5$ m/s, the increasing wind speed reduces the streamwise flow but increases the spanwise velocity component. This is caused as the response of the 3D boundary layer toward the change of the chordwise pressure gradient. As the angle of attack increases (higher wind speed), the increasing pressure gradient alleviates the streamwise momentum of the flow. This causes the boundary layer to be more sensitive toward changes of the flow condition. The centrifugal force and the radial pressure gradient are believed to have a prominent effect within this area, creating a positive spanwise velocity component. As a consequence, the lower magnitude of the streamwise velocity results in the stronger spanwise flow.

In the near wall region, marked by the shaded-green area, the viscous effect due to friction and the chordwise pressure gradient are strong, and the flow is separated as can be depicted from the profiles of v_z/V_{kin} and v_x/V_{kin} in Figure 5.24. The spanwise velocity deficit increases with increasing U_∞. For example, in Figure 5.24d, the near wall spanwise flow is significantly lower for the wind speed of 25 m/s than the other wind speed cases, similar to the η characteristics. This characteristic is expected to arise due to the viscous losses. On the other hand, no much impact of U_∞ on the streamwise velocity is observed, except for the radial position of $0.25R$ where the larger
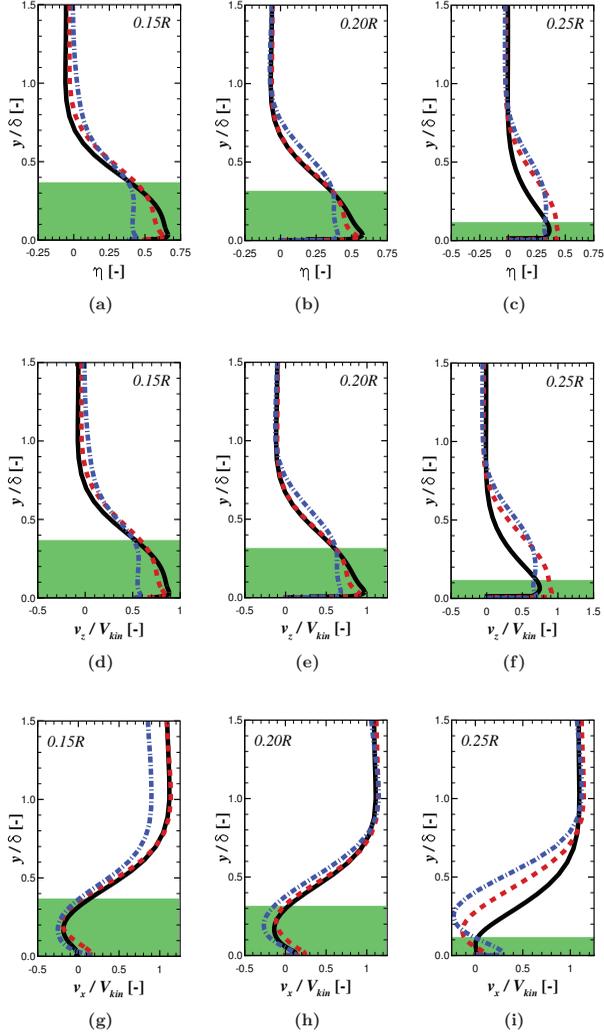
Figure 5.24: Time averaged profiles at some selected inboard stations for η (5.24a-5.24c), v_z/V_{kin} (5.24d-5.24f) and v_x/V_{kin} (5.24g-5.24i). Solid line: $U_\infty = 10.5$ m/s, dashed line: $U_\infty = 15$ m/s and dashed-dot line: $U_\infty = 25$ m/s. Variable y is non-dimensioanlized by the boundary layer thickness (δ). Green area represents the region with the negative v_x/V_{kin} magnitude for the case of $U_\infty = 10.5$ m/s. *Figure is taken from [67].*

wind speed shows stronger v_x/V_{kin}. The latter phenomenon is expected to arise due to the local secondary vortex influence illustrated in Figure 5.17c. This behaviour is shown also for the larger radial positions. It is worthwhile to mention again that the spanwise velocity is normalized by the kinematic velocity. The absolute spanwise velocity was observed to be stronger for the higher wind speed case.

Snel *et. al.* [27, 166] mentioned that 3D correction models often overpredict the magnitude of C_L at large c/r because the models did not properly consider the viscous losses. In Figure 5.24, the viscous losses for the spanwise flow are clearly shown and, thus, need to be taken into account in 3D correction models. The fact that the losses become stronger for the smaller radial position leads to a thinking that this may be related to increasing angle of attack and airfoil thickness. It shall be noted that the studies for 3D effects were usually limited to blades with moderate relative thickness, and the viscous losses are expected to be weaker in this situation.

5.6.2 Near Wake Flows in the Root Region

Similar to the investigations carried out for the new MEXICO rotor, three-dimensional instantaneous flow fields for three different velocity components, namely axial, circumferential and radial directions, in the near wake region of the AVATAR rotor are evaluated. The standard operating condition of $U_\infty = 10.5$ m/s was chosen in this investigation. Three different azimuth positions, at $\theta = 0°$, -45° and -90°, are examined. Again, the evaluation planes at azimuth angle of -45° and -90° represent the planes at 45° and 90°, respectively, downstream of the trailing edge. For the 120° simulation model, due to flow periodicity, the extraction plane for $\theta = $ -90° is represented by the plane at $\theta = 30°$ upstream of the leading edge. The definition of the azimuth angle is given in Figure 2.5. The inflow wind speed of $U_\infty = 10.5$ m/s is used to non-dimensionalize the flow fields. The results are presented in Figures 5.25, 5.29 and 5.30. The horizontal and vertical axes represent radial and axial directions, respectively. In these figures, a positive axial flow is in $+X/R$ direction (same as the wind), positive radial velocity in $+r/R$ and the circumferential velocity in the third component of the coordinate axes, in counter-clockwise direction relative to θ. It shall be noted that the contour scales are different between each velocity component.

Figure 5.25 presents the instantaneous axial velocity field in the near wake region of the AVATAR blade, particularly in the blade root, for the wind speed case of 10.5 m/s. Three azimuthal positions at and after the blade passing are examined, namely 0°, -45° and -90°. It can be seen that, at $\theta = 0°$, the magnitude of U close to the center of rotation is not as high as when no proper nacelle is introduced like for the isolated MEXICO rotor depicted in Figure 4.12. The axial flow increases locally around the nacelle at $X/R \approx 0.075$ which is caused by the nacelle flow interaction. This observation is qualitatively in a good agreement with the studies by Akay *et al.* [150] and Sherry *et al.* [152]. One most noticeable observation in the axial velocity field is the local increase of U/U_∞ at $r/R = 0.2$ that extends downstream of the rotor. This is expected to stem from the tailing vortices behaviour in the root area. In order to clarify this hypothesis, please refer back to the lift coefficient and axial induction (a) distributions

(a) $\theta = 0°$

(b) $\theta = $ -45°

(c) $\theta = $ -90°
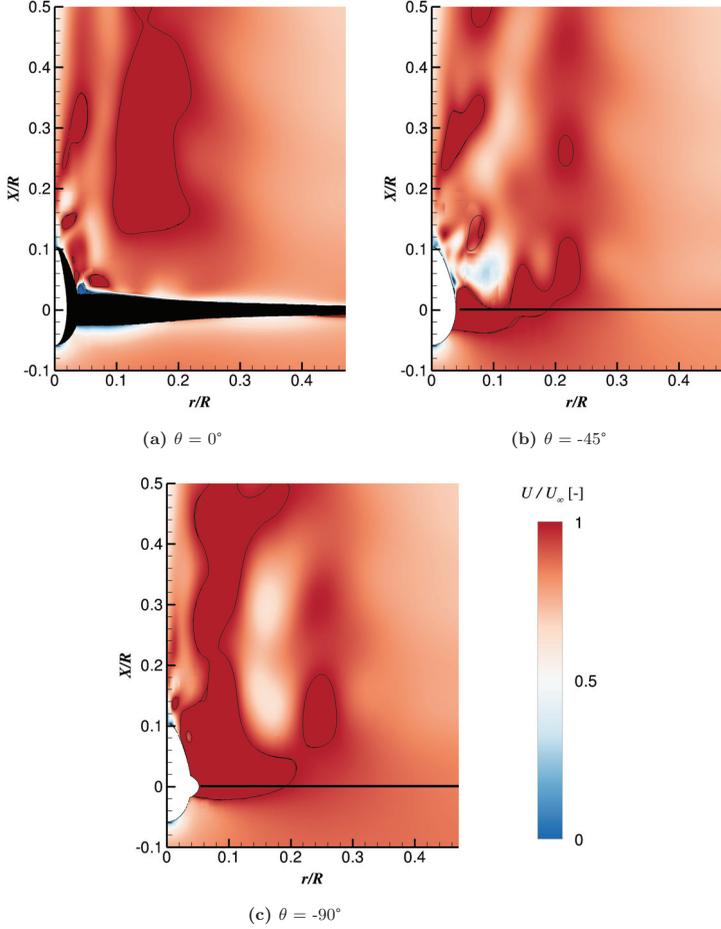
Figure 5.25: Dimensionless axial velocity distributions for three different azimuth angles, 0° (5.25a), -45° (5.25b) and -90° (5.25c). Inflow velocity of 10.5 m/s is in $+X/R$ direction. Black line in the figures indicates the position of the blade. The contour line indicates the magnitude of $U/U_\infty = 1$.
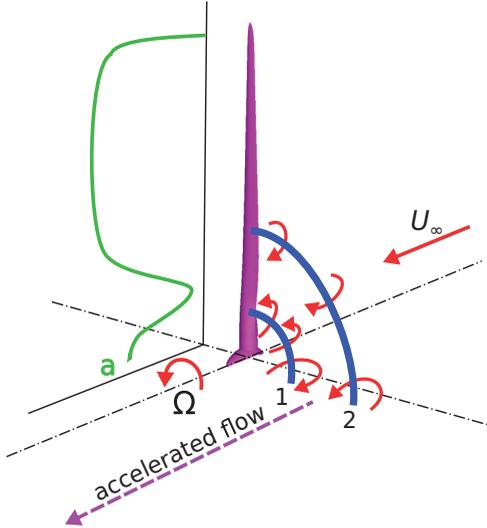
Figure 5.26: The mechanism of the local increase of the axial flow in the root region for the wind speed of 10.5 m/s. For clarity, on the the current blade passing vortices are shown.

of the studied case depicted in Figures 5.13b and 5.13c, respectively. It can be seen that the lift force drops locally around the radial distance of $r/R = 0.2$. In case of the RAV approach, the local drop is also observed for the axial induction at the same location. The local reduction of the axial induction for the same rotor at this position is also observed by Schepers *et al.* [123]. On the other hand, the SHS approach does not indicate an increase of a for $r/R < 0.2$. It was already discussed in Section 5.3 that limitation of the control point distance causes this discrepancy.

The fact that a smaller velocity deficit is observed in Figure 5.25 around the above mentioned position gives a strong indication that the lift (as well as the axial induction) distribution in Figure 5.13 and the axial flow field in Figure 5.25 are related to each other. In Figure 5.26, a sketch describing the mechanism of this phenomenon is given. The axial induction distribution is also illustrated close to the rotor to make the explanation easier to follow. Any changes in the axial induction, and accordingly also in the radial circulation distribution depicted in Figure 5.20a, results in the trailing vortices generation in the wake region. Especially in the root region at $r/R = 0.2$, the local decrease of a (and Γ) towards the hub changes the trailing vortex direction, resulting in a pair of strong counter rotating vortices around

(a) $\theta = 0°$

(b) $\theta = $ -45°

(c) $\theta = $ -90°
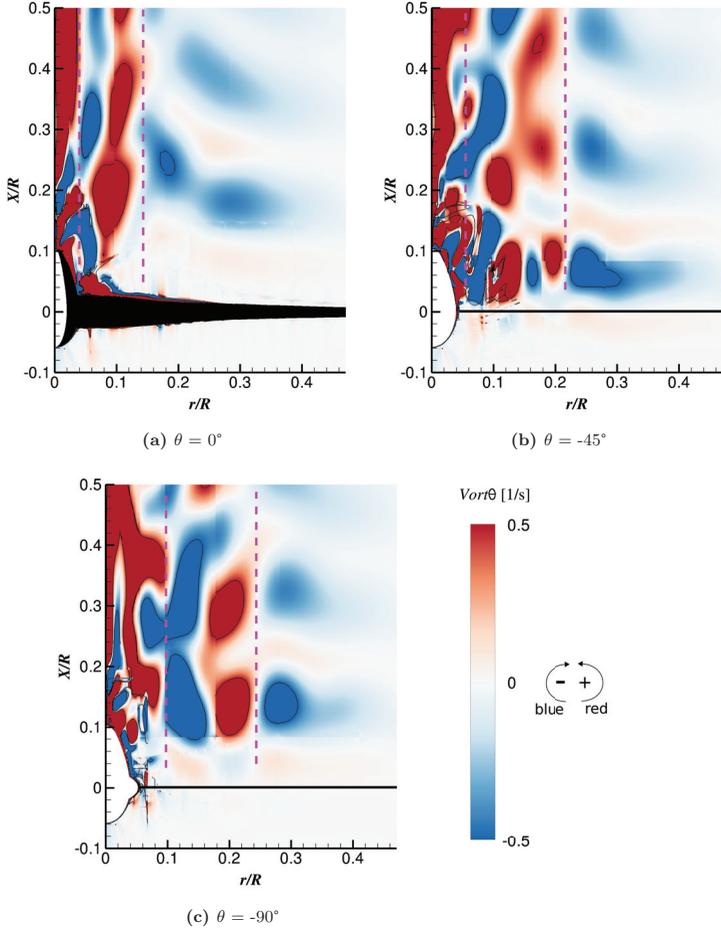
Figure 5.27: Circumferential vorticity distributions for three different azimuth angles, 0° (5.27a), -45° (5.27b) and -90° (5.27c). Inflow velocity of 10.5 m/s is in $+X/R$ direction. Black line in the figures indicates the position of the blade. Dashed purple lines represent the region where the axial flow accelerates.
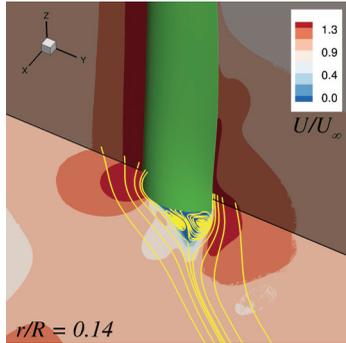
Figure 5.28: Axial flow acceleration in the blade root due to displacement effect.

this area. In Figure 5.26, these vortices are denoted as vortex 1 and vortex 2 (blue lines in the figure). Vortex 1 shows positive direction while vortex 2 is negative. As a consequence, the area between the vortical structures receives additional positive axial flow components from both vortices, that prevents a massive reduction of U.

In Figure 5.27, the above hypothesis is confirmed. The circumferential vorticity distributions downstream of the rotor are plotted for three examined azimuth angles. Blue colour indicates that the vorticity is negative and the vortex direction is inside of the paper (clockwise), while otherwise for red colour (counter-clockwise). This means that in the region between the red and blue coloured vortices, the direction of the local flow from the vortices are the same either in $+X/R$ or $-X/R$. Thus, this increases or decreases the inflow velocity. For example, the dashed-purple lines represent the region where the local flow vortices are in $+X/R$ that enhances the axial flow. In Figure 5.25, it is shown that the axial flow does increase at the marked positions which clearly indicates the relation of both parameters.

Despite the above discussion, the effect is not general and depends on the α and Γ distributions as well as separation situation. It was already shown that the distribution of Γ for the wind speed case of 10.5 m/s (in Figure 5.20a) shows a remarkable drop at this position ($r/R = 0.2$), resulting in the mentioned effect. However, as the wind speed increases to 25 m/s, the local reduction of Γ takes place further outboard at $r/R = 0.5$. It can be seen that the slope and strength of the vortices are stronger. Beside that, a local increase of the circulation is observed at $r/R = 0.17$, resulting in the downwash phenomenon as already discussed in Section 5.5. This implies that as the angle of attack changes, the behaviour of the root vortices varies.

In addition to the wake induced effects, the axial velocity augmentation is partly contributed by the displacement effect around the blade surface. Figure 5.28 illustrates this characteristic, showing that the axial flow increases locally around the blade due to the blade curvature and flow separation. Especially downstream of the trailing edge,

(a) $\theta = 0°$

(b) $\theta = \text{-}45°$

(c) $\theta = \text{-}90°$
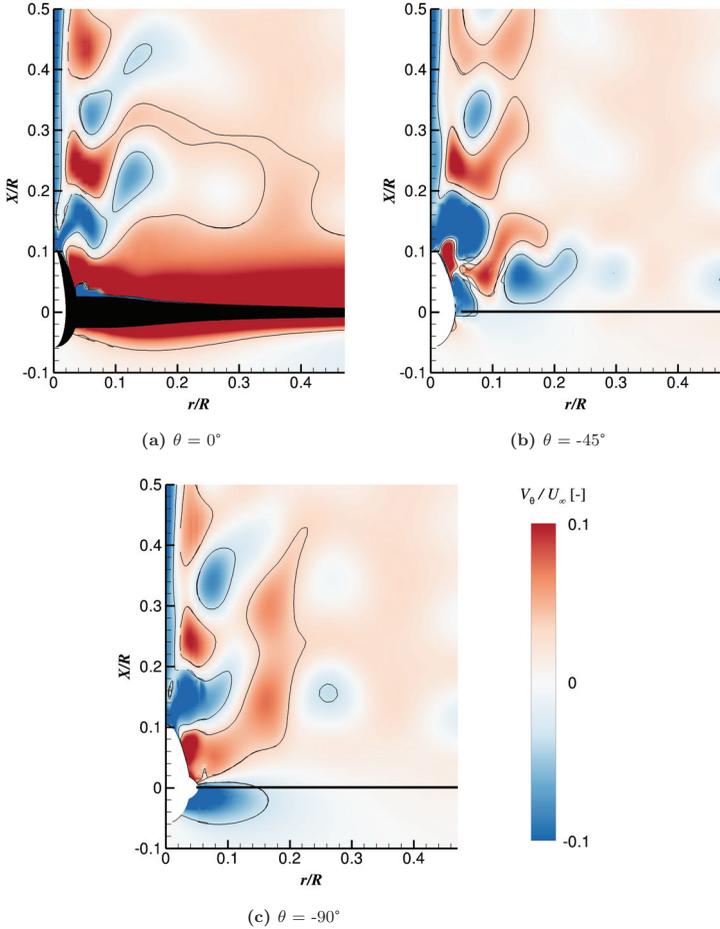
Figure 5.29: Dimensionless circumferential velocity distributions for three different azimuth angles, 0° (5.29a), -45° (5.29b) and -90° (5.29c). Inflow velocity of 10.5 m/s is in $+X/R$ direction. Black line in the figures indicates the position of the blade.

(a) $\theta = 0°$

(b) $\theta = -45°$

(c) $\theta = -90°$
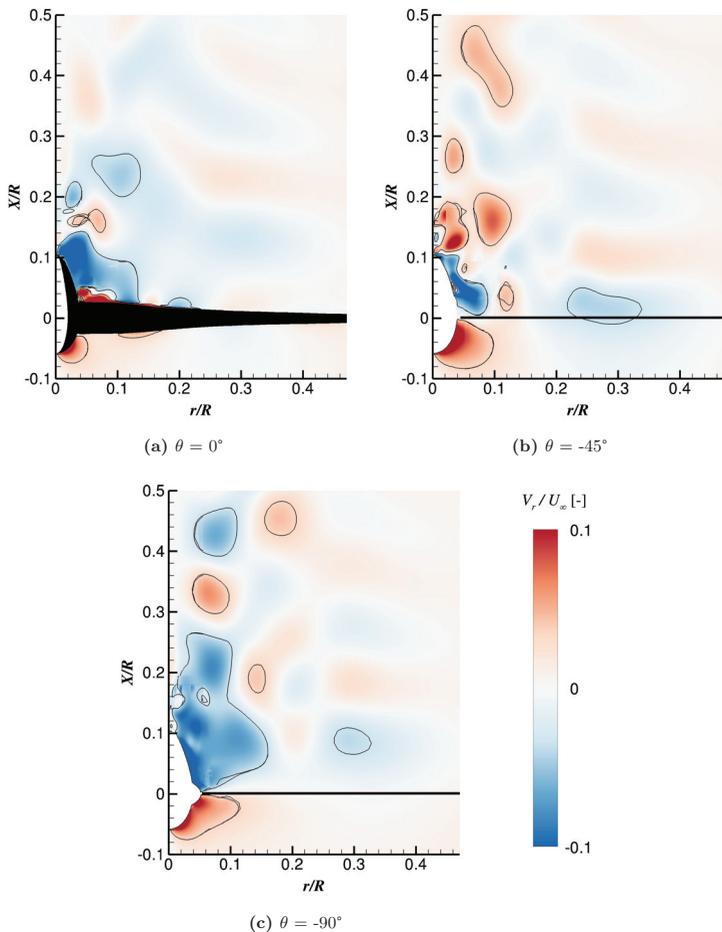
Figure 5.30: Dimensionless radial velocity distributions for three different azimuth angles, 0° (5.30a), -45° (5.30b) and -90° (5.30c). Inflow velocity of 10.5 m/s is in $+X/R$ direction. Black line in the figures indicates the position of the blade.

the influence of the separated area is more dominant.

The relative circumferential velocity (V_θ/U_∞) distribution is presented in Figure 5.29. Similar to the observation for the MEXICO rotor, positive magnitude of the circumferential velocity dominates the near wake flows downstream of the rotor. Adjacent to the blade surface, at $X/R \approx 0.025$, there is a region where $V_\theta < 0$, starting from the blade root extending outboard up to around $0.25R$. This area is related to the backflow within the separation zone on the suction side of the rotor blade. Inside the wake area, some regions with negative circumferential velocity component are also observed. These areas are related to the "scars" of the current and previous blade passages as already observed also by Akay *et al.* [150]. The fact that this is also observed on the edge of the nacelle and around the center of rotation leads to an insight that the nacelle flow interaction may contribute to the phenomena. Furthermore, as the present observation is derived from the completely rotating nacelle, the proper split of the non-rotating and rotating parts of the nacelle may have an influence. This will be discussed in Section 5.7.

Figure 5.30 presents the radial velocity distribution in the near wake area of the AVATAR rotor for the wind speed case of 10.5 m/s. At the azimuth angle of 0°, it can be seen that, adjacent to the blade suction side, a strong positive radial flow is observed near the blade end-wall junction up to $0.17R$. This positive velocity component marks the radial flow field causing the Himmelskamp effect. It becomes evident that this phenomenon occurs only within a thin layer compared to the whole wake area. One important fact is that the positive radial flow area enlarges a bit approaching the end-wall junction of the blade root where the chord to radius ratio (c/r) increases. The radial flow increases close to the nacelle nose due to the displacement effect of the nacelle. It is clearly observed that the accelerated flow area on the nacelle nose enlarges at larger azimuth angles, $\theta = $ -45° and -90°. Figure 5.30a shows that the negative radial flow ($V_r < 0$) is observed near the blade surface particularly at $r/R = 0.13$ and 0.2. This inward radial flow is related to the bound circulation distribution. A close look into the Γ plot in Figure 5.20a for the case of $U_\infty = 10.5$ m/s reveals that local drops of Γ appear at $r/R = 0.13$ and 0.2. Furthermore, the inward flow motion which starts from $r/R = 0.13$ is connected with the inboard flow on the rear side of the nacelle. For larger azimuth angles, this behaviour is still observed around the nacelle.

5.7   Nacelle-Rotor Interaction

In this section, the interaction of the 3D flow in the root region of the blade with the employed nacelle is discussed. To study the dependency of the flow physics on the nacelle, additional simulations were carried out by employing a different simulation strategy and a different nacelle size, but by maintaining the nacelle shape constant. The turbine operates at the benchmark case where $U_\infty = 10.5$ m/s and $n = 9.02$ rpm. Table 5.3 presents the cases simulated for these studies. The additional nacelle size ($R_n = 9.35$ m) is around twice of the original AVATAR nacelle size ($R_n = 4$ m). This results in an increase in the ratio of the nacelle to the rotor radius (R_n/R) from

3.88% to 9.09%. This was deliberately done to stimulate a stronger nacelle interaction impact and to better distinguish the effects from the previous discussed 3D (blade) characteristics. It is worthwhile to mention again that the CFD simulations carried out in the previous sections assume the whole parts of the nacelle to rotate alongside with the blade. For clarity, this approach has been called "standard" case or NR-N01-A. However, this is not physically correct because in reality the nacelle is split into two different components: rotating and non-rotating. It is obvious that the rotating part is the area where the blades are attached and the static part is the area where the tower is located. In the 120° simulation model, a force term opposing the blade rotation was added on the nacelle surfaces to simulate the static part of the nacelle surface. The illustration is given in Figure 5.31. This approach was also employed by Meister [135] in his PhD thesis using the FLOWer code.

In Figure 5.32, flow characteristics on the nacelle for the three studied test cases are illustrated. The top figures represent the rear side of the nacelle, and the bottom figures are for the front side. The standard case (NR-N01-A) is located on the left side,

Table 5.3: Simulated cases for the nacelle-rotor interaction.

Name	R_n [m]	R_n/R [%]	R_n/L_n [%]	Rot. Nacelle Split
NR-N01-A (standard)	4.00	3.88	24.87	No
NR-N01-B (additional)	4.00	3.88	24.87	Yes
NR-N02-A (additional)	9.35	9.09	24.87	No
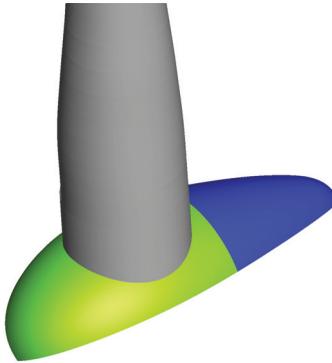
Figure 5.31: Illustration of the rotating (green) and non-rotating (blue) components of the nacelle.
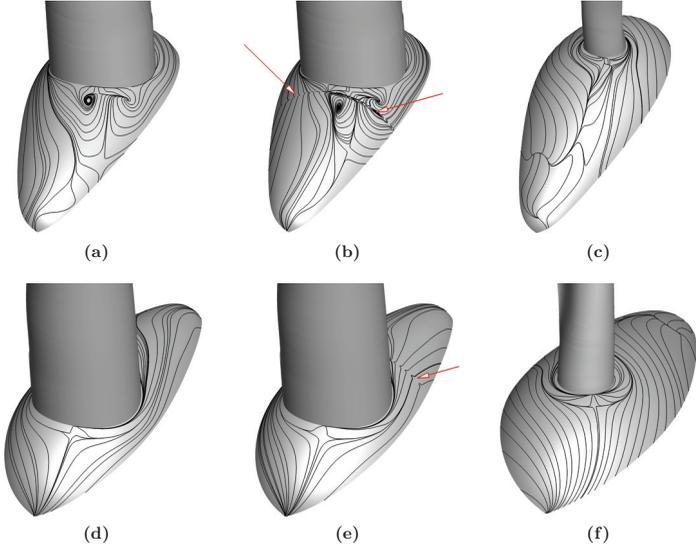
Figure 5.32: Streamlines illustrating the separation characteristics occurring on the rear (upper figure) and front (bottom figures) sides of the nacelle. From left to right: NR-N01-A, NR-N01-B and NR-N02-A.
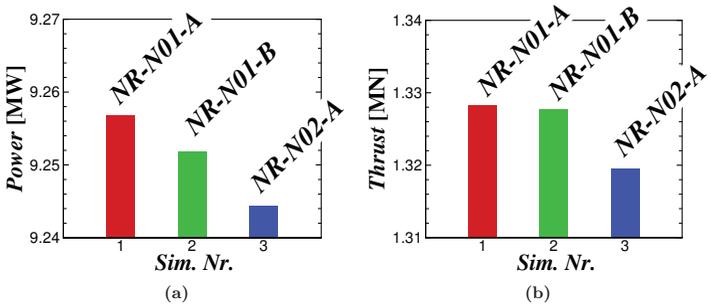
Figure 5.33: Resulting rotor power and thrust force for three studied cases.
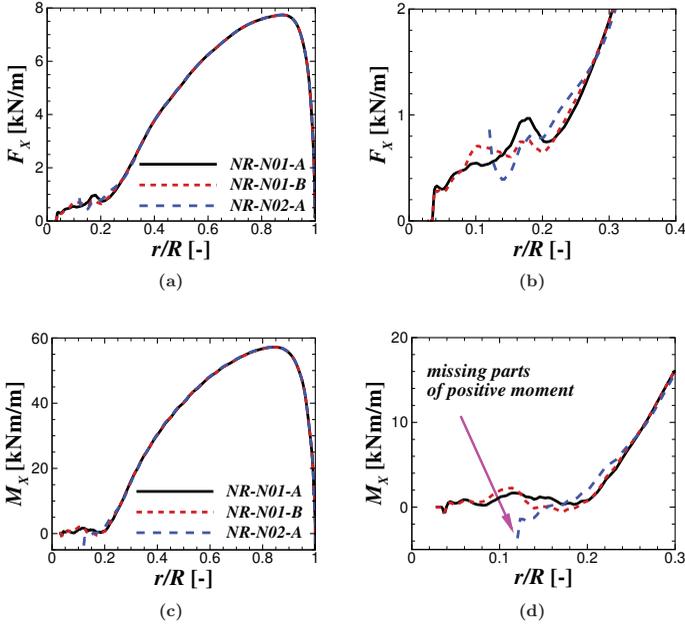
Figure 5.34: Time-averaged sectional loads distributions for three studied test cases. Figures on the right side show the enlarged views of their corresponding left figures.

NR-N01-B in the middle and NR-N02-A (increased nacelle case) on the rear side. It is shown clearly that the flow field behaviour near the wall for NR-N01-A (Figure 5.32a and 5.32d) and NR-N01-B (Figure 5.32b and 5.32e) are similar both on the front and rear sides of the nacelle. Despite that, a noticeable discrepancy is shown downstream of the rotor blade within the separation area. The case presented in Figure 5.32b employs the rotating-zone split mechanism as illustrated in Figure 5.31. The location of the split is indicated by red arrows in Figures 5.32b and 5.32e. A sudden change of the nacelle motion influences the behaviour of the streamlines due to the no-slip condition for the viscous flow. This causes a small reduction of the rotor power and thrust as shown in Figures 5.33a and 5.33b, respectively. In Figures 5.34b and 5.34d, it is shown that the axial force and driving moment, respectively, become smaller at r/R = 0.17 compared to the standard test case. For the case employing a larger nacelle, NR-N02-A, it is shown that the thrust force and power production of the rotor are further reduced. The degradation of the rotor performance is mainly caused by the

missing parts of positive driving moment for $< r/R < 0.1$ as this area is occupied by the nacelle geometry. In addition, it can be seen that the sectional loads for NR-N02-A slightly increase between $0.17 < r/R < 0.25$ due to the induction effect from the nacelle geometry. It was observed that the axial and circumferential velocity components for NR-N02-A within this area are higher than in the other cases. The behaviour of the streamlines displayed in Figures 5.32c and 5.32f shows that a strong horseshoe vortex occurs in the end-wall junction of the blade [167]. However, it shall be noted that the observed horseshoe vortex may be inaccurate because the simulations were carried out using URANS, and two-equation turbulence models are inappropriate for flows with a strong anisotropy [168]. The use of RSM or eddy resolving techniques like LES and DES may improve the situation.

5.8   Summary

Computational Fluid Dynamics (CFD) studies on three-dimensional flow occurring in the root area of the AVATAR rotor have been carried out. Five different wind speeds (U_∞) ranging from below to above the rated conditions were considered in these studies. The turbine rotates at the rotational speed of 9.02 rpm. This parameter along with the pitch angle ($\beta = 0°$) were maintained constant to artificially generate massive separation on the blade at high wind speed cases.

Before performing the 3D simulations, 2D airfoils constructing the AVATAR rotor were simulated and evaluated to develop a more credible basis for the studies of three-dimensional flow in the root area. The results were compared with available measurement data obtained from literature. It was shown that the prediction of the lift polar is accurate within the linear lift region, but the accuracy deteriorates at high angles of attack. Despite that, the general behaviour of the lift polar is reasonably captured. There is no significant difference between the fully turbulent and the prescribed transition calculations because the boundary layer tripping, specified in the experiment and CFD, is very close to the leading edge especially in the linear lift regime. In the post stall region, earlier transition location reduces the maximum attained lift coefficient and stall angle. This shows that the consideration of the transition location is important for the 3D effect studies because the rotational augmentation is strongly influenced by the size of separation. After performing the 2D preliminary studies, the CFD calculations of the AVATAR blade were carried out at a selected wind speed to examine consistency of the numerical simulations. The results were compared with other CFD computations obtained from literature. An excellent agreement is obtained in the predicted sectional loads even though the flow field in the inboard blade area is separated.

With regard to 3D effects, the lift coefficient (C_L) augmentation at the blade inboard region was observed even though the studied blade sections consist of very thick airfoils with the maximum thickness more than 40%. The 3D effects were observed to modify the aerodynamic characteristics of the blade section, where a remarkably higher lift slope occurs in the 3D case. This is caused by the effects of the Coriolis and centrifugal

forces that delay the occurrence of separation and reduce the boundary layer thickness and the size of the separation area. Particularly within the thinner boundary layer, the rotation of the rotor seems to alleviate the decambering effect, modifying the C_p distribution significantly. The drag coefficient (C_D) decreases compared to the 2D simulations due to 3D effects while it increases at certain radial positions for high angles of attack. The local drag augmentation is associated with three main sources: (1) due to reduced pressure, (2) downwash and (3) tip loss effects. It was observed that the root vortex system consist of counter-rotating trailing vortices which become stronger for the higher wind speed case. At this location, a local-distinct increase of the bound circulation is marked and accordingly the drag augmentation.

The quantification of the Coriolis to centrifugal forces (η) weighted by the Rossby number was presented. The ratio of the forces describes the angle of the resulting 3D rotational forces, which can yield information about the shear stress and boundary layer structure. Near the root region close to the line of separation, the flow is directed radially outward which implies that the Himmelskamp force acts mainly in streamwise direction. The Coriolis force strongly influences this area, which shifts further upstream for the higher wind speed case. It was shown that η and the relative spanwise flow decrease with increasing wind speed and radial position, especially near the wall. On the other hand, the reduction of η with increasing wind speed occurs only adjacent to the wall but it is opposite for the rest of the boundary layer area. The reduction of the spanwise flow near the wall is associated with the viscous losses due to frictional forces. In the rest of boundary layer area, the 3D response of the flow is strongly characterized by the pressure gradient. This implies that a stronger reduction of the chordwise flow momentum results in a stronger spanwise flow, caused by the radial pressure gradient and the centrifugal force.

It was observed that the axial flow component increases locally in the wake area at a certain radial station. This phenomenon is caused by the flow acceleration due to the existence of the counter-rotating vortices in the root area. The effect depends strongly on the operating condition of the rotor, especially when the angle of attack and circulation distributions change. Downstream of the rotor, the circumferential flow is generally positive, indicating that the inviscid part of the flow field rotates opposite to the rotor. A strong radial flow was observed within a thin layer in the blade root area. This velocity component is observed to increase in extension and strength with increasing chord to radius ratio.

The studies were carried out for a nacelle geometry that rotates together with the rotor. To investigate the effect for the nacelle in real conditions, a split between the static and rotating parts was defined and investigated. It was shown that the splitting results in a slightly different flow phenomena downstream of the rotor around the blade end-junction area, causing the rotor power and thrust force to slightly reduce. An additional larger nacelle geometry was also examined. The induction effect of the nacelle creates a flow acceleration that slightly increases the axial force and driving moment, but parts of the inboard blade area (that otherwise generate a positive driving moment) are missing as they are occupied by the nacelle geometry. This causes further

reduction of the attained rotor power production.

Chapter 6

Conclusion and Outlook

The fluid flow in the root area of wind turbine rotors is highly complex as and has become the subject of interest for many years because of the implication for accurate load prediction of the wind turbines. The complexity stems from the fact that the inboard area of the blade operates at large angles of attack involving massive flow separation. The presence of rotational motion of the rotor plays an important role in these conditions causing three-dimensional effects to occur. Detailed investigations are necessary to unveil the complexity and to obtain a complete understanding of the mechanism. In this thesis, research key points were drawn for three-dimensional effects in the root area of wind turbine blades in which Computational Fluid Dynamics (CFD) approaches were employed. The computations were carried out using four different techniques, namely the Euler, RANS (Reynolds-Averaged Navier-Stokes), URANS (Unsteady RANS), and DDES (Delayed Detached Eddy Simulation) methods. The researches are divided into two main parts: (1) Studies on the origin of the 3D effects employing the Euler and RANS methods on generic blades with elliptical and NACA airfoil cross-sections. (2) Three-dimensional flows for generic wind turbine rotors of two different sizes employing the URANS and DDES approaches. The studied turbines are the MEXICO (small size) and the AVATAR (large size) rotors. The primary results are summarized and suggestions are given for future works.

6.1 Conclusion

In the present studies, it was shown that three-dimensional effects involve complex behaviours of the flow physics for both inviscid and viscous flows. The studies reveal that 3D effects are generated by a strong interaction of the inviscid and viscous flows, indicating that both effects are of importance. This answers the contradicting conclusions from the preceding studies related to the root cause for the 3D effects. It was observed that the effects become stronger approaching the center of rotation, controlled by parameter c/r, and depend strongly on the chordwise position of the center of rotation (ζ). The latter holds a key relevant for improvement of the current

airfoil/blade design. Two main recommendations are given:

- The aerodynamic performance of the blade section can be improved by shifting the center of rotation further upstream of the leading edge, reducing ζ, to alleviate the strength of separation and to increase the sectional lift coefficient.

- If upstream shift of the center of rotation is not possible due to structural constraints, ζ shall be set at a position where the increased lift benefit due to the displacement effect can be obtained.

These conclusions were derived from the generic blades constructed by thin airfoils and characterized by leading edge separation. The outcomes may deviate for blades with thicker airfoils.

The 3D effects studies carried out for the isolated MEXICO rotor show that the CFD approaches are able to accurately capture the aerodynamic loads of a rotating blade at a high wind speed case, where massive flow separation characterized by rotational augmentation occurs. It was shown that for the blade assuming the isolated condition, where no proper hub geometry is modelled, a strong flow acceleration near the center of rotation was observed, but the effect is generally not significant for the whole flow field surrounding the blade. The change of sign of the rotor tangential and radial velocities marks the location of the root vortices nearby. It was shown that a distinct root vortex occurs in the root area that travels downstream in helical fashion. The studies show that the sectional lift coefficient (C_L) of the blade inboard area is significantly higher than the corresponding 2D conditions. This effect alleviates with increasing blade radius up to the region where c/r is equal to 0.1. Interestingly, no 3D rotational augmentation was observed for a larger radial station (smaller c/r) even though the flow field is massively separated. This leads to a conclusion that 3D effects are insignificant if no strong radial flow presents even though the global flow fields are separated. It is suggested to apply 3D correction models for airfoil polars only in the inboard area up to the region where $c/r = 0.1$. The drag coefficient (C_D) is, however, less influenced than lift, but the trend shows that a slight reduction of C_D occurs.

In evaluations for the generic 10 MW AVATAR rotor, comprehensive studies were carried out for the 3D effects with focus on thick airfoils in the blade inboard area. Preliminarily, two-dimensional studies were performed for thick airfoils constructing the blade to gain a more credible basis of the flow separation characteristics. The prediction is accurate in the linear lift region, but the accuracy deteriorates in the post stall conditions. Despite that, the general behaviour of the 2D lift polar is reasonably predicted. It was shown that the transition location has a strong influence on the 2D aerodynamics in the post stall situation, causing differences in the maximum attained lift and stall angle compared to the case employing the fully turbulent boundary layer. This indicates that the consideration of the transition location is important for the 3D effect studies because the rotational augmentation is strongly influenced by the size of separation.

Similar to the 3D effects observed for the MEXICO rotor, the lift coefficient (C_L) augmentation at the inboard regions of the AVATAR rotor was observed even though

the studied blade sections consist of very thick airfoils with the maximum thickness more than 40%. This involves a remarkably higher lift slope compared to the 2D situation. The drag coefficient was observed to alleviate for this rotor blade, which confirms the conclusion given for the MEXICO rotor. However, the drag coefficient locally increases at several regions that can be divided into: (1) due to reduced pressure, (2) downwash and (3) tip loss effects. The second classification becomes evident as the drag force augments in the location where the blade circulation locally increases. It was observed that the root vortex system consist of counter-rotating trailing vortices which become stronger for the higher wind speed case. In these studies, the ratio of the Coriolis to centrifugal forces (η) weighted by the Rossby number was evaluated that can yield information about the shear stress and boundary layer structure. It was shown that the Coriolis term is dominant in the beginning of separation where the flow is directed radially outward. The investigations show that η and the relative radial flow alleviate with increasing radial position, especially near the wall. Two different zones within the boundary layer based on η response towards wind speed can be classified. (1) Near wall: η reduces with increasing wind speed associated with the viscous losses due to frictional forces. (2) In the rest of the boundary layer area: the 3D response of the flow is strongly characterized by the pressure gradient, implying that a stronger reduction of the chordwise flow momentum results in a stronger relative radial flow.

Similar to the MEXICO rotor, the flow fields surrounding the rotor in the near wake area are presented. The general behaviour of the flow physics is similar, but the significantly increased axial flow near the center of rotation, like for the isolated condition, was not observed because a proper hub connection is modelled. Despite that, the axial velocity enhances locally further outboard at $r/R = 0.2$ for the case of $U_\infty = 10.5$ m/s. The location is shifted a bit outboard for a larger wind speed case. This phenomenon stems from the local flow acceleration due to the existence of the counter-rotating vortices in the root area that depends strongly on the operating condition of the rotor. At last, to close the studies different simulation strategy and nacelle geometry were considered. It was observed that if the nacelle is split between the rotating and non-rotating parts, the rotor power and thrust force slightly alleviate. Increasing the nacelle size leads to the induction effect that slightly enhances the axial force and driving moment. However, some parts of the blade area, that would otherwise generate positive driving moment, are occupied by the nacelle geometry which causes further degradation of the rotor performance.

6.2   Outlook

The present analyses focus on the 3D effects occurring in the root area of horizontal axis wind turbines. The scope of the present works may be extended by the following suggestions:

- The present studies can be used as a fundamental basis for designing more efficient rotors. The newly designed blade that consider the chordwise distance of the

center of rotation needs to be examined in more detail according to the structural stability and its performance under different inflow conditions.

- Further studies can be performed focusing on the root flow characteristics under unsteady inflow conditions. This may help the community to better understand the 3D root flow field characteristics under realistic operating conditions, for example under tower shadow, yaw, inflow turbulence or wind gust.

- A three-dimensional correction model can be developed by considering the fact that 3D effects alleviate due to viscous losses. Furthermore, a simple 3D correlation model based on the 2D inviscid pressure can be developed by considering the 3D response of the inviscid-viscous interactions.

- As the main cause of the performance losses of the rotors is flow separation, the use of passive/active flow control in the inboard area may be helpful for improving the aerodynamic performance of wind turbine rotors, and this may reduce the complexity of the 3D flows within this region.

- At last, higher fidelity studies on the nacelle-rotor interaction is suggested to obtain a deeper insight into 3D characteristics of the horseshoe vortex in the blade root junction area.

References

[1] Shen W.Z. and Sørensen J.N.: Quasi-3D Navier-Stokes model for a rotating airfoil. *Jornal of Computational Physics* 150, 518–548, 1999.

[2] Hansen A. and Butterfield C.: Aerodynamics of horizontal-axis wind turbines. *Annual Review of Fluid Mechanics* 25(1), 115–149, 1993.

[3] Himmelskamp H.: Profile investigations on a rotating airscrew. Ph.D. thesis, Universität Göttingen, 1945.

[4] McCroskey W. and Yaggy P.: Laminar boundary layers on helicopter rotors in forward flight. *AIAA journal* 6(10), 1919–1926, 1968.

[5] Rosenhead L.: Laminar boundary layers. Oxford University Press, 1963.

[6] Sears W.: Potential flow around a rotating cylindrical blade. *Readers Forum, Journal of the Aeronautical Sciences* 17(3), 183, 1950.

[7] Lamb H.: Hydrodynamics. Cambridge university press, 1932.

[8] Fogarty L.E. and Sears W.R.: Potential flow around a rotating, advancing cylindrical blade. *Readers Forum, Journal of the Aeronautical Sciences* 17(9), 599, 1950.

[9] Fogarty L.E.: The laminar boundary layer on a rotating blade. *Journal of the Aeronautical Sciences* 18(4), 247–252, 1951.

[10] Tan H.: On laminar boundary layer over a rotating blade. *Readers Forum, Journal of the Aeronautical Sciences* 20(11), 780–781, 1953.

[11] Rott N. and Smith W.: Some examples of laminar boundary-layer flow on rotating blades. *Journal of the Aeronautical Sciences* 23(11), 991–996, 1956.

[12] Banks W. and Gadd G.: Delaying effect of rotation on laminar separation. *AIAA journal* 1(4), 941–941, 1963.

[13] McCroskey W.J.: Measurements of boundary layer transition, separation and streamline direction on rotating blades. Technical report, NASA, 1971.

REFERENCES

[14] Truong V.K.: Prediction of helicopter rotor airloads based on physical modeling of 3-D unsteady aerodynamics. European Rotorcraft Forum, volume 22. 1996.

[15] Prandtl L.: On boundary layers in three-dimensional flow. 64. Rep. and Trans, 1946.

[16] Jones R.T.: Effects of sweepback on boundary layer and separation. Technical report, NACA TN No. 1402, 1947.

[17] Sears W.R.: The boundary layer of yawed cylinders. *Journal of the aeronautical sciences* 15(1), 49, 1948.

[18] Tanner W. and Yaggy P.: Experimental boundary layer study on hovering rotors. *Journal of the American Helicopter Society* 11(3), 22–37, 1966.

[19] Sørensen J.N., Larsen P.S., Pedersen B.M. and Jensen J.T.: Three-level, viscous-inviscid interaction technique for the prediction of separated flow past rotating wing. Ph.D. thesis, Technical University of Denmark, 1986.

[20] Milborrow D. and Ross J.: Airfoils characteristics of rotating blades. IEA LS-WECS, 12th Meeting of Experts, Copenhagen. 1984.

[21] Savino J. and Nyland T.: Wind turbine flow visualisation studies. Technical report, NASA Lewis Research Center, 1985.

[22] Ronsten G.: Static pressure measurements on a rotating and a non-rotating 2.375 m wind turbine blade. Comparison with 2D calculations. *J. Wind Eng. Ind. Aerodyn.* 39(1), 105–118, 1992.

[23] Bruining A., Van Bussel G., Corten G. and Timmer W.: Pressure Distribution from a Wind Turbine Blade; Field Measurements Compared to 2-Dimensional Wind Tunnel Data. Technical report, 1993.

[24] Carcangiu C.E., Sørensen J.N., Cambuli F. and Mandas N.: CFD-RANS analysis of the rotational effects on the boundary layer of wind turbine blades. *J. Phys.: Conf. Series* 75, 012031, 2007.

[25] Ramos-García N., Sørensen J.N. and Shen W.Z.: A strong viscous-inviscid interaction model for rotating airfoils. *Wind Energy* 17(12), 1957–1984, 2014.

[26] Sørensen J.: Prediction of three-dimensional stall on wind turbine blade using three-level, viscous-inviscid interaction model. EWEC, volume 86, 429–435. 1986.

[27] Snel H., Houwink R., Bosschers J., Piers W.J., van Bussel G.J.W. and Bruining A.: Sectional prediction of 3-D effects for stalled flow on rotating blades and comparison with measurements. EWEC 3959. 1993.

[28] Snel H.: Review of the present status of rotor aerodynamics. *Wind Energy* 1(s 1), 46–69, 1998.

[29] Chaviaropoulos P. and Hansen M.O.: Investigating three-dimensional and rotational effects on wind turbine blades by means of a quasi-3D Navier-Stokes solver. *Journal of Fluids Engineering* 122(2), 330–336, 2000.

[30] Du Z. and Selig M.: The effect of rotation on the boundary layer of a wind turbine blade. *Renewable Energy* 20(2), 167–181, 2000.

[31] Du Z. and Selig M.S.: A 3-D stall-delay model for horizontal axis wind turbine performance prediction. *AIAA paper* 21, 1998.

[32] Dumitrescu H. and Cardos V.: Rotational effects on the boundary-layer flow in wind turbines. *AIAA journal* 42(2), 408–411, 2004.

[33] Dumitrescu H. and Cardos V.: Analysis of leading-edge separation bubbles on rotating blades. *Journal of Aircraft* 47(5), 1815–1819, 2010.

[34] Dumitrescu H. and Cardos V.: Inboard stall delay due to rotation. *Journal of Aircraft* 49(1), 101–107, 2012.

[35] Martínez G., Sørensen J., Shen W. *et al.*: 3D boundary layer study on a rotating wind turbine blade. Journal of Physics: Conference Series, volume 75, 012032. IOP Publishing, 2007.

[36] Wood D.: A three-dimensional analysis of stall-delay on a horizontal-axis wind turbine. *Journal of Wind Engineering and Industrial Aerodynamics* 37(1), 1–14, 1991.

[37] Clausen P., Piddington D. and Wood D.: An experimental investigation of blade element theory for wind turbines. Part 1. mean flow results. *Journal of wind engineering and industrial aerodynamics* 25(2), 189–206, 1987.

[38] Preuss R.D., Suciu E.. and Morino L.: Unsteady potential aerodynamics of rotors with applications to horizontal-axis windmills. *AIAA Journal* 18(4), 385–393, 1980.

[39] Valarezo W. and Liebeck R.: Three-dimensional calculation of windmill surface pressures. 6th AIAA Applied Aerodynamics Conference, volume 1, 168–173. 1988.

[40] Hess J.L. and Valarezo W.O.: Calculation of steady flow about propellers using a surface panel method. *Journal of Propulsion and Power* 1(6), 470–476, 1985.

[41] Cardos V. and Dimitrescu H.: Reply by the Authors to DH Wood. *Technical Comments, AIAA Journal* 43(10), 2269–2269, 2005.

[42] Dumitrescu H. and Cardos V.: Three-dimensional boundary layer on wind turbine blades. *PAMM* 4(1), 432–433, 2004.

[43] Wood D.H.: Comment on" Rotational Effects on the Boundary-Layer Flow in Wind Turbines". *AIAA Journal* 43(10), 2268–2269, 2005.

REFERENCES

[44] Fingersh L., Simms D., Hand M., Jager D., Cotrell J., Robinson M., Schreck S. and Larwood S.: Wind Tunnel Testing of NRELs Unsteady Aerodynamics Experiment. AIAA Paper 2001-0035. 20th ASME Wind Energy Symposium and the 39th Aerospace Sciences Meeting, Reno, NV. 2001.

[45] Hand M.M., Simms D., Fingersh L., Jager D., Cotrell J., Schreck S. and Larwood S.: Unsteady aerodynamics experiment phase VI: wind tunnel test configurations and available data campaigns. National Renewable Energy Laboratory Golden, Colorado, USA, 2001.

[46] Simms D.A., Schreck S., Hand M. and Fingersh L.: NREL unsteady aerodynamics experiment in the NASA-Ames wind tunnel: a comparison of predictions to measurements. National Renewable Energy Laboratory Golden, CO, USA, 2001.

[47] Tangler J.L.: Insight into wind turbine stall and post-stall aerodynamics. *Wind Energy* 7(3), 247–260, 2004.

[48] Schreck S. and Robinson M.: Rotational augmentation of horizontal axis wind turbine blade aerodynamic response. *Wind Energy* 5(2-3), 133–150, 2002.

[49] Schreck S.: Rotationally augmented flow structures and time varying loads on turbine blades. 45th AIAA Aerospace Sciences Meeting and Exhibit. Reno, Nevada, January 8-11, 2007.

[50] Schreck S., Sant T. and Micallef D.: Rotational augmentation disparities in the MEXICO and UAE phase VI experiments. 3rd EWEA Conference-Torque 2010: The Science of making Torque from Wind, Heraklion, Crete, Greece. 28-30 June 2010.

[51] Schreck S.J., Sørensen N.N. and Robinson M.C.: Aerodynamic structures and processes in rotationally augmented flow fields. *Wind Energy* 10(2), 159–178, 2007.

[52] Sørensen N.N., Michelsen J. and Schreck S.: Navier–Stokes predictions of the NREL phase VI rotor in the NASA Ames 80 ft× 120 ft wind tunnel. *Wind Energy* 5(2-3), 151–169, 2002.

[53] Johansen J., Sorensen N., Michelsen J. and Schreck S.: Detached-eddy simulation of flow around the NREL phase VI blade. ASME 2002 Wind Energy Symposium, 106–114. American Society of Mechanical Engineers, 2002.

[54] Duque E.P., Burklund M.D. and Johnson W.: Navier-Stokes and comprehensive analysis performance predictions of the NREL phase VI experiment. *Journal of Solar Energy Engineering* 125(4), 457–467, 2003.

[55] Herráez I., Stoevesandt B. and Peinke J.: Insight into rotational effects on a wind turbine blade using Navier–Stokes computations. *Energies* 7(10), 6798–6822, 2014.

[56] Bangga G., Lutz T. and Krämer E.: An examination of rotational effects on large wind turbine blades. EAWE PhD Seminar 11, Stuttgart. 2015.

[57] Bangga G., Kim Y., Lutz T., Weihing P. and Krämer E.: Investigations of the inflow turbulence effect on rotational augmentation by means of CFD. *Journal of Physics: Conference Series* 753(2), 022026, 2016. doi:10.1088/1742-6596/753/2/022026.

[58] Zahle F., Bak C., Guntur S., Sørensen N.N. and Troldborg N.: Comprehensive aerodynamic analysis of a 10 mw wind turbine rotor using 3d cfd. 32nd ASME Wind Energy Symposium, 0359. 2014.

[59] Kim Y., Jost E., Bangga G., Weihing P. and Lutz T.: Effects of ambient turbulence on the near wake of a wind turbine. Journal of Physics: Conference Series, volume 753, 032047. IOP Publishing, 2016. doi:10.1088/1742-6596/753/3/032047.

[60] Johansen J. and Sørensen N.N.: Aerofoil characteristics from 3D CFD rotor computations. *Wind Energy* 7(4), 283–294, 2004.

[61] Laursen J., Enevoldsen P. and Hjort S.: 3D CFD quantification of the performance of a multi-megawatt wind turbine. Journal of Physics: Conference Series, volume 75, 012007. IOP Publishing, 2007.

[62] Gross A., Fasel H., Friederich T. and Kloker M.: Numerical investigation of rotational augmentation for S822 wind turbine airfoil. *Wind Energy* 15(8), 983–1007, 2012.

[63] Troldborg N., Bak C., Sørensen N., Madsen H., Réthoré M., Zahle F. and Guntur S.: Experimental and numerical investigation of 3D aerofoil characteristics on a MW wind turbine. Proceedings of the European Wind Energy Association. Vienna, Austria, February 4-7, 2013.

[64] Baldwin B.S. and Lomax H.: Thin layer approximation and algebraic model for separated turbulent flows, volume 257. American Institute of Aeronautics and Astronautics, 1978.

[65] Pape A.L. and Lecanu J.: 3D Navier–Stokes computations of a stall-regulated wind turbine. *Wind Energy* 7(4), 309–324, 2004.

[66] Guntur S. and Sørensen N.N.: A study on rotational augmentation using CFD analysis of flow in the inboard region of the MEXICO rotor blades. *Wind Energy* 18(4), 745–756, 2015.

[67] Bangga G., Lutz T., Jost E. and Krämer E.: CFD studies on rotational augmentation at the inboard sections of a 10 MW wind turbine rotor. *Journal of Renewable and Sustainable Energy* 9(2), 023304, 2017. doi:10.1063/1.4978681.

[68] Bangga G., Lutz T. and Krämer E.: Numerical Investigation of Unsteady Aerodynamic Effects on Thick Flatback Airfoils. German Wind Energy Conference 12, Bremen.

[69] Baker J., Mayda E. and Van Dam C.: Experimental analysis of thick blunt trailing-edge wind turbine airfoils. *Journal of Solar Energy Engineering* 128(4), 422–431, 2006.

[70] Bak C., Johansen J. and Andersen P.B.: Three-dimensional corrections of airfoil characteristics based on pressure distributions. Proceedings of the European Wind Energy Conference, 1–10. 2006.

[71] Troldborg N., Zahle F. and Sørensen N.N.: Simulation of a MW rotor equipped with vortex generators using CFD and an actuator shape model. Proceedings of 53rd Aiaa Aerospace Sciences Meeting. American Institute of Aeronautics & Astronautics, 2015.

[72] Troldborg N., Zahle F. and Sørensen N.N.: Simulations of wind turbine rotor with vortex generators. Journal of Physics: Conference Series, volume 753, 022057. IOP Publishing, 2016.

[73] Longo J.: Verification of the computer code CEVCATS for the computation of vortex flows around delta wings. *Zeitschrift fuer Flugwissenschaften und Weltraumforschung* 20(5), 213–226, 1996.

[74] Aumann P., Bartelheimer W., Bleecke H., Kuntz M., Lieser J., Monsen E., Eisfeld B., Fassbender J., Heinrich R. and Kroll N, Mauss M, Raddatz J, Reisch U, Roll B, Schwarz T: FLOWer installation and user manual. Deutsches Zentrum fur Luft- und Raumfahrt, 2008.

[75] Kroll N., Rossow C.C., Becker K. and Thiele F.: The MEGAFLOW project. *Aerospace Science and Technology* 4(4), 223–237, 2000.

[76] Schwarz T., Spiering F. and Kroll N.: Grid coupling by means of Chimera interpolation techniques. Second Symposium of Simulation of Wing and Nacelle Stall. 2010.

[77] Bangga G., Weihing P., Lutz T. and Krämer E.: Effect of computational grid on accurate prediction of a wind turbine rotor using delayed detached-eddy simulations. *Journal of Mechanical Science and Technology* 31(5), 2359–2364, 2017. doi:10.1007/s12206-017-0432-6.

[78] Weihing P., Letzgus J., Bangga G., Lutz T. and Krämer E.: Hybrid RANS/LES capabilities of the Flow Solver FLOWer - Application to Flow around Wind Turbines. 6th Symposium on Hybrid RANS-LES Methods. Strasbourg, France, September 26 - 28, 2016.

[79] Kowarsch U., Oehrle C., Hollands M., Keßler M. and Krämer E.: Computation of helicopter phenomena using a higher order method. High Performance Computing in Science and Engineering 13, 423–438. Springer, 2013.

[80] Dietz M., Kessler M., Krämer E. and Wagner S.: Tip vortex conservation on a helicopter main rotor using vortex-adapted chimera grids. *AIAA journal* 45(8), 2062–2074, 2007.

[81] Kranzinger P., Hollands M., Kessler M., Wagner S. and Kraemer E.: Generation and Verification of Meshes Used in Automated Process Chains to Optimize Rotor Blades. 50th AIAA Aerospace Sciences Meeting including the New Horizons Forum and Aerospace Exposition, 1260. 2012.

[82] Liu X.D., Osher S. and Chan T.: Weighted essentially non-oscillatory schemes. *Journal of computational physics* 115(1), 200–212, 1994.

[83] Shur M.L., Spalart P.R., Strelets M.K. and Travin A.K.: A hybrid RANS-LES approach with delayed-DES and wall-modelled LES capabilities. *Int. J. Heat Fluid Flow* 29(6), 1638–1649, 2008.

[84] Lutz T., Meister K. and Krämer E.: Near wake studies of the MEXICO rotor. Proceedings of European Wind Energy Association. Brussels, March 14-17, 2011.

[85] Jameson A., Schmidt W., Turkel E. *et al.*: Numerical solutions of the Euler equations by finite volume methods using Runge-Kutta time-stepping schemes. *AIAA paper* 1259, 1981, 1981.

[86] Jameson A.: Multigrid algorithms for compressible flow calculations. Multigrid Methods II, 166–201. Springer, 1986.

[87] Favre A.: Equations des gaz turbulents compressibles. 1. formes générales. *Journal de mecanique* 4(4), 361–390, 1965.

[88] Favre A.: Equations des gaz turbulents compressibles. 2. methode des vitesses moyennes methode des vitesses macroscopiques ponderees par la masse volumique. *Journal de mecanique* 4(4), 391–421, 1965.

[89] Blazek J.: Computational fluid dynamics: principles and applications. Butterworth-Heinemann, 2015.

[90] Hinze J.: Turbulence. McGraw-Hill, 1975.

[91] Wilcox D.C. *et al.*: Turbulence modeling for CFD, volume 2. DCW industries La Canada, CA, 1998.

[92] Fröhlich J. and von Terzi D.: Hybrid LES/RANS methods for the simulation of turbulent flows. *Progress in Aerospace Sciences* 44(5), 349–377, 2008.

REFERENCES

[93] Leonard A.: Energy cascade in large-eddy simulations of turbulent fluid flows. *Advances in geophysics* 18, 237–248, 1975.

[94] Smagorinsky J.: General circulation experiments with the primitive equations: I. the basic experiment. *Monthly weather review* 91(3), 99–164, 1963.

[95] Speziale C.G.: Computing non-equilibrium turbulent flows with time-dependent RANS and VLES. Fifteenth International Conference on Numerical Methods in Fluid Dynamics, 123–129. Springer, 1997.

[96] Speziale C.: Turbulence modeling for time-dependent RANS and VLES: a review. *AIAA journal* 36(2), 173–184, 1998.

[97] Fan T.C., Tian M., Edwards J.R., Hassan H.A. and Baurle R.A.: Validation of a hybrid Reynolds-averaged/large-eddy simulation method for simulating cavity flameholder configurations. AIAA Fluid Dynamics Conference & Exhibit, 31 st, Anaheim, CA. 2001.

[98] Spalart P., Jou W., Strelets M., Allmaras S. *et al.*: Comments on the feasibility of LES for wings, and on a hybrid RANS/LES approach. *Advances in DNS/LES* 1, 4–8, 1997.

[99] Spalart P.R. and Allmaras S.R.: A one equation turbulence model for aerodinamic flows. *AIAA journal* 94, 1992.

[100] Pope S.B.: Turbulent flows. Cambridge University Press, 2000.

[101] Menter F. and Kuntz M.: Adaptation of eddy-viscosity turbulence models to unsteady separated flow behind vehicles. The aerodynamics of heavy vehicles: trucks, buses, and trains, 339–352. Springer, 2004.

[102] Menter F.R.: Two-equation eddy-viscosity turbulence models for engineering applications. *AIAA journal* 32(8), 1598–1605, 1994.

[103] Spalart P.R., Deck S., Shur M., Squires K., Strelets M.K. and Travin A.: A new version of detached-eddy simulation, resistant to ambiguous grid densities. *Theoretical and computational fluid dynamics* 20(3), 181–195, 2006.

[104] Bangga G. and Sasongko H.: Dynamic stall prediction of a pitching airfoil using an adjusted two-equation URANS turbulence model. *Journal of Applied Fluid Mechanics* 10(1), 1–10, 2017.

[105] Wienken W., Stiller J. and Keller A.: A method to predict cavitation inception using large-eddy simulation and its application to the flow past a square cylinder. *Journal of Fluids Engineering* 128(2), 316–325, 2006.

[106] Breuer M., Lakehal D. and Rodi W.: Flow around a surface mounted cubical obstacle: comparison of LES and RANS-results. Computation of Three-Dimensional Complex Flows, 22–30. Springer, 1996.

[107] Ducros F., Ferrand V., Nicoud F., Weber C., Darracq D., Gacherieu C. and Poinsot T.: Large-eddy simulation of the shock/turbulence interaction. *Journal of Computational Physics* 152(2), 517–549, 1999.

[108] Akselvoll K. and Moin P.: Large eddy simulation of a backward facing step flow. *Engineering Turbulence Modelling and Experiments* 2, 303–313, 2014.

[109] Spalart P.R.: Detached-eddy simulation. *Annual review of fluid mechanics* 41, 181–202, 2009.

[110] Caruelle B.: Simulations d'écoulements instationnaires turbulents en aérodynamique: application à la prédiction du phénomène de tremblement. Ph.D. thesis, 2000.

[111] Deck S.: Simulation numérique des charges latérales instationnaires sur des configurations de lanceur. Ph.D. thesis, Orléans, 2002.

[112] Glauert H.: Airplane propellers. Aerodynamic theory, 169–360. Springer, 1935.

[113] Sørensen J.N.: Blade-Element/Momentum Theory. General Momentum Theory for Horizontal Axis Wind Turbines, 99–121. Springer, 2016.

[114] Masters I., Chapman J., Willis M. and Orme J.: A robust blade element momentum theory model for tidal stream turbines including tip and hub loss corrections. *Journal of Marine Engineering & Technology* 10(1), 25–35, 2011.

[115] Bangga G., Hutomo G., Syawitri T., Kusumadewi T., Oktavia W., Sabila A., Setiadi H., Faisal M., Hendranata Y., Lastomo D. *et al.*: Enhancing BEM simulations of a stalled wind turbine using a 3D correction model. Journal of Physics: Conference Series, volume 974, 012020. IOP Publishing, 2018.

[116] Prandtl L. and Betz A.: Vier Abhandlungen zur Hydrodynamik und Aerodynamik...: mit einer Literaturübersicht als Anhang. Kaiser Wilhelm-Instituts für Strömungsforschung, 1927.

[117] Shen W.Z., Mikkelsen R., Sørensen J.N. and Bak C.: Tip loss corrections for wind turbine computations. *Wind Energy* 8(4), 457–475, 2005.

[118] Schepers J., Boorsma K., Cho T., Gomez-Iradi S., Schaffarczyk P., Jeromin A., Shen W., Lutz T., Meister K., Stoevesandt B. *et al.*: Final report of IEA Task 29. *Mexnext (Phase 1), Analysis of Mexico wind tunnel measurements ECN-E-12-004* 2012.

[119] Boorsma K. and Schepers J.: New MEXICO experiment. Technical report, ECN Wind Energy, 2014.

[120] Lekou D. *et al.*: Avatar deliverable d1.2 reference blade design. Technical report, ECN Wind Energy, 2015.

[121] Sørensen N. *et al.*: Power curve predictions WP2 deliverable 2.3. Technical report, ECN Wind Energy, 2014.

[122] Bak C., Zahle F., Bitsche R., Kim T., Yde A., Henriksen L., Andersen P., Natarajan A. and Hansen M.: Design and performance of a 10 MW turbine. Technical report, Technical University of Denmark, dtu-10mw-rwt.vindenergi.dtu.dk, 2013.

[123] Schepers J., Ceyhan O., Savenije F., Stettner M., Kooijman H., Chaviarapoulos P., Sieros G., Ferreira C.S., Sørensen N., Wächter10 M. *et al.*: AVATAR: AdVanced Aerodynamic Tools for lArge Rotors. Proceedings of 33rd ASME Wind Energy Symposium. 2015.

[124] Laino D.J., Hansen A.C. and Minnema J.E.: Validation of the aerodyn subroutines using NREL unsteady aerodynamics experiment data. ASME 2002 Wind Energy Symposium, 179–189. American Society of Mechanical Engineers, 2002.

[125] Shen W.Z., Hansen M.O. and Sørensen J.N.: Determination of the angle of attack on rotor blades. *Wind Energy* 12(1), 91–98, 2009.

[126] Hansen M., Srensen N., Srensen J. and Michelsen J.: Extraction of lift, drag and angle of attack from computed 3D viscous flow around a rotating blade 499501, 1997.

[127] Hansen M.O. and Johansen J.: Tip studies using CFD and comparison with tip loss models. *Wind Energy* 7(4), 343–356, 2004.

[128] Klein L., Lutz T. and Krämer E.: CFD simulation of a floating horizontal axis model wind turbine. EAWE PhD Seminar 11. Stuttgart, Germany, September 23-25, 2015.

[129] Jost E., Fischer A., Bangga G., Lutz T. and Krämer E.: An investigation of unsteady 3D effects on trailing edge flaps. *Wind Energy Science* 2, 241–256, 2016. doi:10.5194/wes-2-241-2017.

[130] Shen W.Z., Hansen M.O. and Sørensen J.N.: Determination of angle of attack (AoA) for rotating blades. Wind Energy, 205–209. Springer, 2007.

[131] Schmitz S. and Chattot J.J.: Characterization of three-dimensional effects for the rotating and parked NREL phase VI wind turbine. *Journal of Solar Energy Engineering* 128, 445–454, 2006.

[132] Sant T., van Kuik G. and Van Bussel G.: Estimating the angle of attack from blade pressure measurements on the NREL phase VI rotor using a free wake vortex model: Axial conditions. *Wind Energy* 9(6), 549–577, 2006.

[133] Kroll N.: Berechnung von Strömungsfeldern um Propeller und Rotoren im Schwebeflug durch die Lösung der Euler-Gleichungen. Deutsche Forschungsanstalt für Luft-und Raumfahrt, 1989.

[134] Jameson A. and Liu F.: Multigrid Euler calculations for three dimensional cascades. AIAA, Aerospace Sciences Meeting, 28 th, Reno, NV, 1990. 1990.

[135] Meister K.: Numerische Untersuchung zum aerodynamischen und aeroelastischen Verhalten einer Windenergieanlage bei turbulenter atmosphärischer Zuströmung. Shaker Verlag, 2015.

[136] Rossow C.C.: Berechnung von Strömungsfeldern durch Lösung der Euler-Gleichungen mit einer erweiterten Finite-Volumen Diskretisierungsmethode. Deutsche Forschungsanstalt für Luft-und Raumfahrt, 1989.

[137] Rudnik R.: Erweiterung eines dreidimensionalen Euler-Verfahrens zur Berechnung des Strömungsfeldes um Nebenstromtriebwerke mit Fan-und Kernstahl. *Zeitschrift für Flugwissenschaften und Weltraumforschung* 15(5), 285–288, 1991.

[138] Rossow C.C.: Efficient computation of inviscid flow fields around complex configurations using a multiblock multigrid method. *Communications in applied numerical methods* 8(10), 735–747, 1992.

[139] Radespiel R., Rossow C. and Swanson R.: Efficient cell-vertex multigrid scheme for the three-dimensional Navier-Stokes equations. *AIAA journal* 28(8), 1464–1472, 1990.

[140] Wood D.: Some effects of finite solidity on the aerodynamics of horizontal-axis wind turbines. *Journal of Wind Engineering and Industrial Aerodynamics* 26(2), 255–273, 1987.

[141] Bangga G., Weihing P., Lutz T. and Krämer E.: Hybrid RANS/LES simulations of the three-dimensional flow at root region of a 10 MW wind turbine rotor. New Results in Numerical and Experimental Fluid Mechanics XI, 707–716. Springer, 2018. doi:10.1007/978-3-319-64519-3_63.

[142] Corten G.P.: Inviscid stall model. Netherlands Energy Research Foundation, 2001.

[143] Streiner S.: Beitrag zur numerischen Simulation der Aerodynamik und Aeroelastik großer Windkraftanlagen mit horizontaler Achse. Verlag Dr. Hut, 2011.

[144] Meister K., Lutz T. and Krämer E.: Simulation of a 5MW wind turbine in an atmospheric boundary layer. J. Phys.: Conf. Series, volume 555, 012071. 2014.

[145] Spalart P.R.: Young-person's guide to detached-eddy simulation grids 2001.

REFERENCES

[146] Bangga G., Lutz T. and Krämer E.: Root flow characteristics and 3D effects of an isolated wind turbine rotor. *Journal of Mechanical Science and Technology* 31(8), 3839–3844, 2017. doi:10.1007/s12206-017-0728-6.

[147] Shelton A., Abras J., Jurenko R. and Smith M.J.: Improving the CFD predictions of airfoils in stall. 43rd AIAA Aerospace Sciences Meeting and Exhibit, Reno, Jan. 2005.

[148] Potsdam M. and Mavriplis D.: Unstructured mesh CFD aerodynamic analysis of the NREL Phase VI rotor. 47th AIAA Aerospace Sciences Meeting Including the New Horizons Forum and Aerospace Exposition, 1221. 2009.

[149] Bangga G., Guma G., Lutz T. and Krämer E.: Numerical simulations of a large offshore wind turbine exposed to turbulent inflow conditions. *Wind Engineering* 42(2), 88–96, 2018.

[150] Akay B., Ragni D., Simão Ferreira C. and Bussel G.: Experimental investigation of the root flow in a horizontal axis wind turbine. *Wind Energy* 17(7), 1093–1109, 2014.

[151] Akay B.: The root flow of horizontal axis wind turbine blades: Experimental analysis and numerical validation. Ph.D. thesis, Delft University of Technology, 2016.

[152] Sherry M., Nemes A., Jacono D.L., Blackburn H.M. and Sheridan J.: The interaction of helical tip and root vortices in a wind turbine wake. *Physics of Fluids (1994-present)* 25(11), 117102, 2013.

[153] Boorsma K. and Schepers J.: Description of experimental set-up. Mexico measurements. *ECN, Netherlands* 2009.

[154] Sicot C., Devinant P., Loyer S. and Hureau J.: Rotational and turbulence effects on a wind turbine blade. Investigation of the stall mechanisms. *J. Wind Eng. Ind. Aerodyn.* 96(8), 1320–1331, 2008.

[155] Bangga G., Hutomo G., Wiranegara R. and Sasongko H.: Numerical study on a single bladed vertical axis wind turbine under dynamic stall. *Journal of Mechanical Science and Technology* 31(1), 261–267, 2017. doi:10.1007/s12206-016-1228-9.

[156] Lindenburg C.: Investigation into rotor blade aerodynamics. Technical report, ECN Report: ECN-C-03-025, 2003.

[157] Van Rooij R. and Timmer W.: Roughness sensitivity considerations for thick rotor blade airfoils. *Journal of solar energy engineering* 125(4), 468–478, 2003.

[158] Drela M.: XFOIL: An analysis and design system for low Reynolds number airfoils. Low Reynolds number aerodynamics, 1–12. Springer, 1989.

[159] Bangga G., Kusumadewi T., Hutomo G., Sabila A., Syawitri T., Setiadi H., Faisal M., Wiranegara R., Hendranata Y., Lastomo D. *et al.*: Improving a two-equation eddy-viscosity turbulence model to predict the aerodynamic performance of thick wind turbine airfoils. Journal of Physics: Conference Series, volume 974, 012019. IOP Publishing, 2018.

[160] Celik I.B., Ghia U., Roache P.J. *et al.*: Procedure for estimation and reporting of uncertainty due to discretization in CFD applications. *Journal of fluids Engineering* 130(7), 2008.

[161] Sørensen N.N.: General purpose flow solver applied to flow over hills. Ph.D. thesis, Technical University of Denmark, 1995.

[162] Papadakis G. and Voutsinas S.G.: In view of accelerating CFD simulations through coupling with vortex particle approximations. Journal of Physics: Conference Series, volume 524, 012126. IOP Publishing, 2014.

[163] Schreck S., Fingersh L., Siegel K., Singh M. and Medina P.: Rotational augmentation on a 2.3-MW rotor blade with thick flatback airfoil cross sections. Proceedings of the 51st AIAA Aerospace Sciences Meeting, AIAA 2013, volume 915. 2013.

[164] Raj N.V.: An improved semi-empirical model for 3-D post-stall effects in horizontal axis wind turbines. Master's thesis, 2000.

[165] Corrigan J. and Schillings J.: Empirical model for stall delay due to rotation. American Helicopter Society Aeromechanics Specialists Conference, San Francisco, CA, volume 21. 1994.

[166] Snel H.: Scaling laws for the boundary layer flow on rotating windturbine blades. 4th IEA symposium on aerodynamics for wind turbines, Rome. 1991.

[167] Bangga G., Ashfahani A., Sugianto E., Saadiyah D., Putri T., Jost E. and Lutz T.: Three-dimensional flow in the vicinity of a circular cylinder mounted to a flat plate at high Reynolds number. AIP Conference Proceedings, volume 1788, 030012. AIP Publishing, 2017.

[168] Ansys A.F.: 14.0 Theory Guide. *ANSYS inc* 218–221, 2011.

REFERENCES

Galih Bangga

Curriculum Vitae

✉ bangga@iag.uni-stuttgart.de
📄 galih.bangga90@gmail.com
born on the 6th of May, 1990
in Kediri, Indonesia

Education

09/2011 – 03/2013   **M.Eng.**, *Mechanical Engineering Department, Institut Teknologi sepuluh Nopember*, 3.92/4.00.

09/2008 – 08/2012   **B.Eng.**, *Mechanical Engineering Department, Institut Teknologi sepuluh Nopember*, 3.91/4.00.

Experience

from 11/2013   **Research Assistant**, *Institute of Aerodynamics and Gas Dynamics, University of Stuttgart*.
Investigating three-dimensional effects in the root area of wind turbine rotors using Computational Fluid Dynamics (CFD) approaches.

09/2011 – 08/2012   **Teaching Assistant**, *Mechanical Engineering Department, Institut Teknologi Sepuluh Nopember*.
Preparing the materials for the basic physics, mechanical vibration and fluid dynamics courses.

Honours and Awards

11/2017   Invited poster presentation and travel grant on the 33rd International CAE Conference, Vicenza, Italy, 2017.

08/2016   Best paper award on the International Conference on Engineering, Science and Nanotechnology 2016, Solo, Indonesia, 2016.

11/2015   1st runner up in *Scientific Paper* category on the Innovative Writing Competition, Paris, France, 2015.

09/2015   Best student paper award on the 2nd International Conference on Mechanical Engineering, Bali, Indonesia, 2015.

11/2013 – 05/2017   DGHE scholarship from the Ministry of Research, Technology and Higher Education of Indonesia (PhD).

09/2011 – 03/2013   Fast Track scholarship from the Ministry of Education and Culture of Indonesia (Master).

09/2008 – 08/2012   Excellent Winner scholarship (Beasiswa Unggulan Juara) from the Ministry of Education and Culture of Indonesia (Bachelor).

09/2007 – 08/2008   ORBIT scholarship from the Hasri Ainun Habibie foundation (Senior High School).

This book presents the state of the art in the analyses of three-dimensional flow over rotating wind turbine blades. Systematic studies for wind turbine rotors with different sizes were carried out numerically employing three different simulation approaches, namely the Euler, URANS and DDES methods. The main mechanisms of the lift augmentation in the blade inboard region are described in detail. The physical relations between the inviscid and viscous effects are presented and evaluated, emphasizing the influence of the flow curvature on the resulting pressure distributions. Detailed studies concerning the lift augmentation for large wind turbine rotors are considered as thick inboard airfoils characterized by massive separation are desired to stronger contribute to power production. Special attention is given to the analyses of wind turbine loads and flow field that can be helpful for the interpretation of the occurring physical phenomena. The book is aimed at students, researchers, engineers and physicists dealing with wind engineering problems, but also for a wider audience involved in flow computations.